

Nature-Inspired Algorithms for Real-World Optimization Problems

Guest Editors: Wei Fang, Xiaodong Li, Mengjie Zhang, and Mengqi Hu





Nature-Inspired Algorithms for Real-World Optimization Problems

Journal of Applied Mathematics

Nature-Inspired Algorithms for Real-World Optimization Problems

Guest Editors: Wei Fang, Xiaodong Li, Mengjie Zhang,
and Mengqi Hu



Copyright © 2014 Hindawi Publishing Corporation. All rights reserved.

This is a special issue published in "Journal of Applied Mathematics." All articles are open access articles distributed under the Creative Commons Attribution License, which permits unrestricted use, distribution, and reproduction in any medium, provided the original work is properly cited.

Editorial Board

Saeid Abbasbandy, Iran
Mina B. Abd-El-Malek, Egypt
Mohamed A. Abdou, Egypt
Syed Abdul Mohiuddine, KSA
Subhas Abel, India
Janos Abonyi, Hungary
Sergei Alexandrov, Russia
M. Montaz Ali, South Africa
Mohammad R. Aliha, Iran
Carlos J. S. Alves, Portugal
Mohamad Alwash, USA
Gholam R. Amin, Oman
Igor Andrianov, Germany
Boris Andrievsky, Russia
Whye-Teong Ang, Singapore
Abul-Fazal M. Arif, KSA
Sabri Arik, Turkey
Ali R. Ashrafi, Iran
Allaberen Ashyralyev, Turkey
Francesco Aymerich, Italy
Jalel Azaiez, Canada
Seungik Baek, USA
Hamid Bahai, UK
Olivier Bahn, Canada
Antonio Bandera, Spain
Jean-Pierre Barbot, France
Mostafa Barigou, UK
Roberto Barrio, Spain
Henri Baudrand, France
Alfredo Bellen, Italy
Vasile Berinde, Romania
Jafar Biazar, Iran
Anjan Biswas, KSA
Abdellah Bnouhachem, Morocco
Gabriele Bonanno, Italy
Walter Briec, France
James Robert Buchanan, USA
Humberto Bustince, Spain
Xiao Chuan Cai, USA
Piermarco Cannarsa, Italy
Jinde Cao, China
Yijia Cao, China
Zhenfu Cao, China
Bruno Carpentieri, Netherlands
Ana Carpino, Spain

Alexandre Carvalho, Brazil
Song Cen, China
Shih-sen Chang, China
Shuenn-Yih Chang, Taiwan
Tai-Ping Chang, Taiwan
Wei-Der Chang, Taiwan
Kripasindhu Chaudhuri, India
Jianbing Chen, China
Ke Chen, UK
Ru-Dong Chen, China
Rushan Chen, China
Xinkai Chen, Japan
Yuming Chen, Canada
Zhang Chen, China
Zhi-Zhong Chen, Japan
Ching-Hsue Cheng, Taiwan
Chin-Hsiang Cheng, Taiwan
Eric Cheng, Hong Kong
Hui Cheng, China
Jin Cheng, China
Qi Cheng, USA
Francisco Chiclana, UK
Jen-Tzung Chien, Taiwan
Chongdu Cho, Korea
Han H. Choi, Republic of Korea
M. S. H. Chowdhury, Malaysia
Yu-Ming Chu, China
Hung-Yuan Chung, Taiwan
Angelo Ciaramella, Italy
Pedro J. Coelho, Portugal
Carlos Conca, Chile
Vitor Costa, Portugal
Jie Cui, USA
Lirong Cui, China
Livija Cveticanin, Serbia
Binxiang Dai, China
Gaoliang Dai, Germany
Hua Dai, China
Michael Defoort, France
Hilmi Demiray, Turkey
Mingcong Deng, Japan
Youjun Deng, France
Orazio Descalzi, Chile
Raffaele Di Gregorio, Italy
Kai Diethelm, Germany

Daniele Dini, UK
Urmila Diwekar, USA
Vit Dolejsi, Czech Republic
BoQing Dong, China
Rodrigo W. dos Santos, Brazil
Wenbin Dou, China
Rafael Escarela-Perez, Mexico
Magdy A. Ezzat, Egypt
Meng Fan, China
Ya Ping Fang, China
István Faragó, Hungary
Didier Felbacq, France
Ricardo Femat, Mexico
Antonio J. M. Ferreira, Portugal
George Fikioris, Greece
Michel Fliess, France
Marco A. Fontelos, Spain
Dimitris Fotakis, Serbia
Tomonari Furukawa, USA
Maria Gandarias, Spain
Huijun Gao, China
Naiping Gao, China
Xiao-wei Gao, China
Xin-Lin Gao, USA
Laura Gardini, Italy
Winston Garira, South Africa
Leonidas N. Gergidis, Greece
Bernard J. Geurts, Netherlands
Sandip Ghosal, USA
Dibakar Ghosh, India
Pablo González-Vera, Spain
Alexander N. Gorban, UK
Keshlan S. Govinder, South Africa
Said R. Grace, Egypt
Jose L. Gracia, Spain
Maurizio Grasselli, Italy
Zhi-Hong Guan, China
Nicola Guglielmi, Italy
Frédéric Guichard, Canada
Kerim Guney, Turkey
Shu-Xiang Guo, China
Vijay Gupta, India
Saman K. Halgamuge, Australia
Ridha Hambli, France
Abdelmagid S. Hamouda, Qatar

Bo Han, China
Maoan Han, China
Pierre Hansen, Canada
Ferenc Hartung, Hungary
Xiao-Qiao He, China
Yuqing He, China
Nicolae Herisanu, Romania
O. Hernandez-Lerma, Mexico
Luis Javier Herrera, Spain
J. C. D. Hoenderkamp, Netherlands
Thomas Höhne, Germany
Wei-Chiang Hong, Taiwan
Sun-Yuan Hsieh, Taiwan
Ning Hu, Japan
Ying Hu, France
Dan Huang, China
Jianguo Huang, China
Ting-Zhu Huang, China
Zhenkun Huang, China
Zhilong L. Huang, China
Asier Ibeas, Spain
Mustafa Inc, Turkey
Gerardo Iovane, Italy
Anuar Ishak, Malaysia
Takeshi Iwamoto, Japan
George Jaiani, Georgia
GunHee Jang, Korea
Zhongxiao Jia, China
Daqing Jiang, China
Haijun Jiang, China
Jianjun Jiao, China
Xing Jin, China
Zhen Jin, China
Lucas Jódar, Spain
Zlatko Jovanoski, Australia
Tadeusz Kaczorek, Poland
Dongsheng Kang, China
Sangmo Kang, USA
Ido Kanter, Israel
Abdul Hamid Kara, South Africa
Dimitrios A. Karras, Greece
Dogan Kaya, Turkey
Ihsan Kaya, Turkey
C. Masood Khaliq, South Africa
Waqar A. Khan, Pakistan
Khalil Khanafer, USA
Hyunsung Kim, Korea
Jong Hae Kim, Republic of Korea
Younjea Kim, Republic of Korea
Svein Kleiven, Sweden
Kazutake Komori, Japan
Vassilis Kostopoulos, Greece
Jisheng Kou, China
Roberto A. Kraenkel, Brazil
Kannan Krithivasan, India
Vadim A. Krysko, Russia
Jin L. Kuang, Singapore
Gennady M. Kulikov, Russia
Venugopal Kumaran, India
Mirosław Lachowicz, Poland
Hak-Keung Lam, UK
Heung-Fai Lam, Hong Kong
Tak-Wah Lam, Hong Kong
Luciano Lamberti, Italy
Peter G L Leach, Cyprus
Jaehong Lee, Korea
Myung-Gyu Lee, Korea
Usik Lee, Republic of Korea
Wen-Chuan Lee, Taiwan
Jinsong Leng, China
Hua Li, Singapore
Lixiang Li, China
Qin Li, China
Qingdu Li, China
Shiyong Li, China
Shuai Li, Hong Kong
Wan-Tong Li, China
Wenlong Li, Hong Kong
Xiang Li, China
Dongfang Liang, UK
Jin Liang, China
Yan Liang, China
Ching-Jong Liao, Taiwan
Teh-Lu Liao, Taiwan
Chong Lin, China
Gao Lin, China
Yiping Lin, China
Yong-Cheng Lin, China
Ignacio Lira, Chile
Chein-Shan Liu, Taiwan
Chongxin Liu, China
Fei Liu, China
Kang Liu, USA
Meiqin Liu, China
Peide Liu, China
Pengfei Liu, China
Peter Liu, Taiwan
Sheng Liu, Australia
Shutian Liu, China
Tao Liu, China
Weiqing Liu, China
Yansheng Liu, China
Zhengrong Liu, China
Zhijun Liu, China
Zhuangjian Liu, Singapore
Jose L. López, Spain
Benzhuo Lu, China
Hao Lu, USA
Henry Horng-Shing Lu, Taiwan
Hongbing Lu, China
Shiping Lu, China
Yuan Lu, China
Gilles Lubineau, KSA
Zhen Luo, China
Changfeng Ma, China
Li Ma, China
Lifeng Ma, China
Ruyun Ma, China
Shuping Ma, China
Krzysztof Magnucki, Poland
Nazim I. Mahmudov, Turkey
Oluwole D. Makinde, South Africa
Flavio Manenti, Italy
Francisco J. Marcellán, Spain
Vasile Marinca, Romania
Giuseppe Marino, Italy
Guiomar Martín-Herrán, Spain
Carlos Martín-Vide, Spain
Alessandro Marzani, Italy
Nikos E. Mastorakis, Bulgaria
Nicola Mastronardi, Italy
Panayotis Takis Mathiopoulos, Greece
Gianluca Mazzini, Italy
Michael McAleer, Netherlands
Stephane Metens, France
Michael Meylan, Australia
Efren Mezura-Montes, Mexico
Fan Min, China
Alain Miranville, France
Ram N. Mohapatra, USA
Gisele Mophou, France
José Morais, Portugal
Cristinel Mortici, Romania
Emmanuel Moulay, France

Jaime E. Munoz Rivera, Brazil
 Javier Murillo, Spain
 Roberto Natalini, Italy
 Srinivasan Natesan, India
 Tatsushi Nishi, Japan
 Mustapha Nourelfath, Canada
 Andreas "Ochsner, Australia
 Wlodzimierz Ogryczak, Poland
 Roger Ohayon, France
 Javier Oliver, Spain
 Soontorn Oraintara, USA
 Donal O'Regan, Ireland
 Martin Ostoja-Starzewski, USA
 Turgut "Oziş, Turkey
 Claudio Padra, Argentina
 Vincent Pagneux, France
 Reinaldo Martinez Palhares, Brazil
 Quanke Pan, China
 Endre Pap, Serbia
 Sehie Park, Korea
 Manuel Pastor, Spain
 Giuseppe Pellicane, South Africa
 Francesco Pellicano, Italy
 Juan Manuel Peña, Spain
 Jian-Wen Peng, China
 Ricardo Perera, Spain
 Malgorzata Peszynska, USA
 Allan C. Peterson, USA
 Andrew Pickering, Spain
 Somyot Plubtieng, Thailand
 Hector Pomares, Spain
 Roland Potthast, UK
 Kerehalli V. Prasad, India
 Radu-Emil Precup, Romania
 Mario Primicerio, Italy
 Morteza Rafei, Netherlands
 Phadungsak Rattanadecho, Thailand
 Laura Rebollo-Neira, UK
 Mahmoud M. Reda Taha, USA
 Roberto Renò, Italy
 Bruno G. M. Robert, France
 Juan A. Rodriguez-Velázquez, Spain
 Ignacio Rojas, Spain
 Carla Roque, Portugal
 Debasish Roy, India
 Imre J. Rudas, Hungary
 Abbas Saadatmandi, Iran
 Kunihiko Sadakane, Japan
 Samir H. Saker, Egypt
 R. Sakthivel, Republic of Korea
 Juan José Salazar González, Spain
 Miguel A. F. Sanjuan, Spain
 Bogdan Sasu, Romania
 Richard Saurel, France
 Wolfgang Schmidt, Germany
 Mehmet Sezer, Turkey
 Naseer Shahzad, KSA
 Pengjian Shang, China
 M. Shariyat, Iran
 Hui-Shen Shen, China
 Jian Hua Shen, China
 Yong Shi, China
 Yasuhide Shindo, Japan
 Patrick Siarry, France
 Fernando Simões, Portugal
 Theodore E. Simos, Greece
 Georgios Sirakoulis, Greece
 Robert Smith?, Canada
 Francesco Soldovieri, Italy
 Abdel-Maksoud A. Soliman, Egypt
 Qiankun Song, China
 Xinyu Song, China
 Yuri N. Sotskov, Belarus
 Ivanka Stamova, USA
 Niclas Strömberg, Sweden
 Housheng Su, China
 Ray K.L. Su, Hong Kong
 Chengjun Sun, Hong Kong
 Jitao Sun, China
 Wenyu Sun, China
 W. Y. Szeto, Hong Kong
 Toshio Tagawa, Japan
 Ying Tan, China
 San-Yi Tang, China
 XianHua Tang, China
 Nasser-Eddine Tatar, KSA
 Zhidong Teng, China
 Engang Tian, China
 Alexander Timokha, Norway
 Aydin Tiryaki, Turkey
 Yiying Tong, USA
 Hossein Torkaman, Iran
 Mariano Torrisi, Italy
 Juan J. Trujillo, Spain
 Jung-Fa Tsai, Taiwan
 George Tsiatas, Greece
 Charalampos Tsitouras, Greece
 Antonia Tulino, USA
 Stefano Ubertini, Italy
 Jeong S. Ume, Korea
 Alexandrina Untaroiu, USA
 Sergey Utyuzhnikov, UK
 Kuppalapalle Vajravelu, USA
 Alvaro Valencia, Chile
 Olaf van der Sluis, Netherlands
 Erik Van Vleck, USA
 Ezio Venturino, Italy
 Jesus Vigo-Aguiar, Spain
 Michael N. Vrahatis, Greece
 Michael Vynnycky, Sweden
 Baolin Wang, China
 Dongqing Wang, China
 Guangchen Wang, China
 Heng Wang, Singapore
 Mingxin Wang, China
 Peiguang Wang, China
 Qing-Wen Wang, China
 Shuming Wang, Singapore
 Xiang Wang, China
 Yaonan Wang, China
 Youqing Wang, China
 Yuh-Rau Wang, Taiwan
 Junzo Watada, Japan
 Guoliang Wei, China
 Jinjia Wei, China
 Junjie Wei, China
 Wei Wei, China
 Li Weili, China
 Martin Weiser, Germany
 Frank Werner, Germany
 Man Leung Wong, Hong Kong
 Cheng Wu, China
 Min-Hsien Wu, Taiwan
 Qingbiao Wu, China
 Shi-Liang Wu, China
 Wei Wu, China
 Xian Wu, China
 Xiangjun Wu, China
 Yuqiang Wu, China
 Tiecheng Xia, China
 Yonghui Xia, China
 Xian Xian-Yong, China
 Gongnan Xie, China
 Xuejun Xie, China



Daoyi Xu, China
Wei Xu, China
Yuesheng Xu, USA
Zhiqiang Xu, China
Fuzhen Xuan, China
Gregory S. Yablonsky, USA
Chao Yan, USA
Bin Yang, China
Chao Yang, China
Chao-Tung Yang, Taiwan
Chunyu Yang, China
Dar-Li Yang, Taiwan
Guowei Yang, China
Na Yang, China
Xiao-Jun Yang, China
Zhichun Yang, China
Her-Terng Yau, Taiwan
Wei-Chang Yeh, Taiwan
Guan H. Yeoh, Australia

Chih-Wei Yi, Taiwan
Bo Yu, China
Simin Yu, China
Gonglin Yuan, China
Jinyun Yuan, Brazil
Xiaohui Yuan, China
Rafal Zdunek, Poland
Ashraf Zenkour, Egypt
Guisheng Zhai, Japan
Jianming Zhan, China
Meng Zhan, China
Henggui Zhang, UK
Heping Zhang, China
Jiangang Zhang, China
Jifeng Zhang, China
Jingxin Zhang, Australia
Ke Zhang, China
Liang Zhang, China
Long Zhang, China

Sheng Zhang, China
Zhengqiu Zhang, China
Zihua Zhang, China
Baosheng Zhao, China
Chongbin Zhao, Australia
Shan Zhao, USA
Yun-Bo Zhao, China
Renat Zhdanov, USA
Dong Zheng, USA
Bin Zhou, China
Huaichun Zhou, China
Huamin Zhou, China
Shangbo Zhou, China
Quanxin Zhu, China
William Zhu, China
Xinqun Zhu, Australia
Goangseup Zi, Korea
Zhiqiang Zuo, China

Contents

Nature-Inspired Algorithms for Real-World Optimization Problems, Wei Fang, Xiaodong Li, Mengjie Zhang, and Mengqi Hu
Volume 2015, Article ID 359203, 2 pages

Metaheuristic Approaches for Hydropower System Scheduling, Ieda G. Hidalgo, Regiane S. de Barros, Jéssica P. T. Fernandes, João Paulo F. Estrócio, and Paulo B. Correia
Volume 2015, Article ID 701851, 6 pages

Coincidence Detection Using Spiking Neurons with Application to Face Recognition, Fadhlan Kamaruzaman, Amir Akramin Shafie, and Yasir M. Mustafah
Volume 2015, Article ID 534198, 20 pages

Gravitational Search Algorithm and Selection Approach for Optimal Distribution Network Configuration Based on Daily Photovoltaic and Loading Variation, Koong Gia Ing, H. Mokhlis, H. A. Illias, M. M. Aman, and J. J. Jamian
Volume 2015, Article ID 894758, 11 pages

Migrating Birds Optimization for the Seaside Problems at Maritime Container Terminals, Eduardo Lalla-Ruiz, Christopher Expósito-Izquierdo, Jesica de Armas, Belén Melián-Batista, and J. Marcos Moreno-Vega
Volume 2015, Article ID 781907, 12 pages

An UWB LNA Design with PSO Using Support Vector Microstrip Line Model, Salih Demirel, Filiz Gunes, and A. Kenan Keskin
Volume 2015, Article ID 374325, 10 pages

Editorial

Nature-Inspired Algorithms for Real-World Optimization Problems

Wei Fang,¹ Xiaodong Li,² Mengjie Zhang,³ and Mengqi Hu⁴

¹*School of IoT Engineering, Jiangnan University, No. 1800, Lihu Avenue, Wuxi 214122, China*

²*School of Computer Science and IT, RMIT University, GPO Box 2476, Melbourne, VIC 3001, Australia*

³*Evolutionary Computation Research Group, School of Engineering and Computer Science, Victoria University of Wellington, P.O. Box 600, Wellington 6140, New Zealand*

⁴*University of Illinois at Chicago, 842 W. Taylor Street, 2039 ERE, Chicago, IL 60661, USA*

Correspondence should be addressed to Wei Fang; fangwei@jiangnan.edu.cn

Received 26 August 2015; Accepted 26 August 2015

Copyright © 2015 Wei Fang et al. This is an open access article distributed under the Creative Commons Attribution License, which permits unrestricted use, distribution, and reproduction in any medium, provided the original work is properly cited.

Nature-inspired algorithms are a set of novel problem-solving methodologies and approaches and have been attracting considerable attention for their good performance. Representative examples of nature-inspired algorithms include artificial neural networks (ANN), fuzzy systems (FS), evolutionary computing (EC), and swarm intelligence (SI), and they have been applied to solve many real-world problems. Despite the popularity of nature-inspired algorithms, many challenges remain which require further research efforts.

The contributions presented in this special issue include some latest developments of nature-inspired algorithms, such as genetic algorithm, particle swarm optimization, ant colony optimization, migrating birds optimization, neural networks, gravitational search algorithm, and their applications. Several real-world optimization problems have been studied by several nature-inspired algorithms.

K. G. Ing et al. present the application of gravitational search algorithm (GSA) in determining the optimal daily configuration of distribution network based on photovoltaic generation and system loading. The distribution network reconfiguration problem is formulated as a minimization problem to minimize the power loss of the distribution. Experimental results show that GSA with selection approach is a simple yet effective technique to minimize total daily power loss.

The work of E. Lalla-Ruiz et al. studies the improved migrating birds optimization (MBO) approach for solving

two seaside problems, which are the Dynamic Berth Allocation Problem (DBAP) and Quay Crane Scheduling Problem (QCSP). MBO approach can solve these two problems with high-quality solutions with a small short computational cost, which makes this technique a competitive method for frequently seaside operations either performed individually or embedded into real decision-support systems.

The paper by I. G. Hidalgo et al. integrates genetic algorithm (GA) with Strength Pareto Evolutionary Algorithm (SPEA) and ant colony optimization (ACO) to deal with the short-term scheduling problem. The problem is solved by the proposed two hybrid approaches in two phases. The experimental results on two hydroelectric plants show that both approaches produce good performance for the optimal dynamic dispatch in the short-term operation of hydroelectric plants.

S. Demirel et al. focus on the optimal design of ultra-wideband (UWB) low-noise amplifier (LNA) based on the support vector regression machine (SVRM) microstrip line model. Particle swarm optimization (PSO) algorithm has been employed in the solving procedure for two parameters resulting in good performance in terms of accuracy and fast convergence.

F. Kamaruzaman et al. propose the coincidence detection (CD) classifier with two learning methods based on the Spiking Neural Network (SNN). The proposed method can produce an output spike pattern from an input pair identical

to the discrete Spike Response Model (SRM) with significantly lower floating operations and a much faster processing time.

The papers included in this special issue are of high quality, hopefully making useful contributions to the research area of nature-inspired algorithms.

Acknowledgments

Dr. Wei Fang acknowledges the support from the National Nature Science Foundation of China (Grants nos. 61105128, 61170119, and 61373055), the Nature Science Foundation of Jiangsu Province, China (Grants nos. BK20131106, BK20130161, and BK20130160), the Postdoctoral Science Foundation of China (Grant no. 2014M560390), the Fundamental Research Funds for the Central Universities, China (Grant no. JUSRP51410B), and Six Talent Peaks' Project of Jiangsu Province (Grant no. DZXX-025). As guest editors, we would like to thank the contributing authors and the reviewers for their hard work in preparing and reviewing the submissions.

*Wei Fang
Xiaodong Li
Mengjie Zhang
Mengqi Hu*

Research Article

Metaheuristic Approaches for Hydropower System Scheduling

Ieda G. Hidalgo,¹ Regiane S. de Barros,² Jéssica P. T. Fernandes,² João Paulo F. Estrócio,³ and Paulo B. Correia²

¹Faculty of Technology, State University of Campinas (Unicamp), 13.484-332 Limeira, SP, Brazil

²Faculty of Mechanical Engineering, State University of Campinas (Unicamp), 13.083-860 Campinas, SP, Brazil

³Cia Energética de São Paulo (CESP), 04.447-011 São Paulo, SP, Brazil

Correspondence should be addressed to Ieda G. Hidalgo; iedahidalgo@gmail.com

Received 28 February 2015; Revised 8 June 2015; Accepted 10 June 2015

Academic Editor: Wei Fang

Copyright © 2015 Ieda G. Hidalgo et al. This is an open access article distributed under the Creative Commons Attribution License, which permits unrestricted use, distribution, and reproduction in any medium, provided the original work is properly cited.

This paper deals with the short-term scheduling problem of hydropower systems. The objective is to meet the daily energy demand in an economic and safe way. The individuality of the generating units and the nonlinearity of their efficiency curves are taken into account. The mathematical model is formulated as a dynamic, mixed integer, nonlinear, nonconvex, combinatorial, and multiobjective optimization problem. We propose two solution methods using metaheuristic approaches. They combine Genetic Algorithm with Strength Pareto Evolutionary Algorithm and Ant Colony Optimization. Both approaches are divided into two phases. In the first one, to maximize the plant's net generation, the problem is solved for each hour of the day (static dispatch). In the second phase, to minimize the units' switching on-off, the day is considered as a whole (dynamic dispatch). The proposed methodology is applied to two Brazilian hydroelectric plants, in cascade, that belong to the national interconnected system. The nondominated solutions from both approaches are presented. All of them meet demand respecting the physical, electrical, and hydraulic constraints.

1. Introduction

Brazilian power generation system is predominantly hydroelectric. The operation planning/scheduling of this system is divided into three stages: long-term, medium-term, and short-term. In the long-term the horizon is up to five years with monthly time-step. In this stage, the plants are grouped by subsystems. In the medium-term the horizon is up to one year with monthly or weekly time-step. In this stage, the plants are treated individually. In the short-term the horizon is up to two weeks with hourly time-step. In this stage the generating units (GUs) of the plants are considered and the physical, electrical, and hydraulic aspects are taken into account.

Within the short-term stage is made the optimal dynamic dispatch (ODD) of the GUs, which is the focus of this paper. It consists of determining, for each hour of the day, which units should be operating and their generating level. The objective is to meet energy demand, optimally utilizing the available water resources and reducing the maintenance costs of the GUs.

Two equations are important for the ODD of the GUs: the hydraulic balance and production function, Hidalgo et al. [1]. The hydraulic balance determines the reservoir's final volume from the initial volume, water inflow, and water outflow. The production function relates the plant's generation with the turbines efficiency, generators efficiency, net head, and water discharged.

The optimal use of the available water resources is related to plant's efficient operation. Yi et al. [2] propose to maximize the system efficiency, Arce et al. [3] aim to minimize the power generation losses, Finardi and Scuzziato [4] suggest minimizing the total water released, and Catalão et al. [5] propose to maximize the value of the stored water in the reservoir.

The maintenance cost of the GUs is affected, among other things, by the number of startups and shutdowns during the operation. Each switching on-off of a unit is estimated to reduce its useful life by about 10 to 15 hours, Nilsson et al. [6]. Borghetti et al. [7] define a cost for the switching on-off of GUs. Chang et al. [8] propose a penalty for each of the status

changes of the units. Chancelier and Renaud [9] determine a minimum time required between the startup and shutdown of the GUs.

As shown, in general, the ODD problem has two main objectives: to increase the net generation of the plant and reduce the number of times that status of the GUs is changed. System constraints related to this problem include meeting the load demand and respecting the physical, electrical, and hydraulic constraints. It has discrete variables for the selection of GUs and continuous variables for the loading dispatch of each online GU. The production function of a hydroelectric plant and the efficiency curves of the units are nonlinear. The ODD problem is usually nonconvex. The combinatorial nature of the problem makes it more complex.

Artificial Intelligence techniques have been applied to solve similar problems to ODD. Santos and Ohishi [10] apply Genetic Algorithm (GA) and Lagrangian Relaxation (LR) to three Brazilian hydroelectric systems. Muller [11] employs GA and Sequential Quadratic Programming (SQP) for the Unit Commitment (UC) problem in order to minimize losses in power generation. Colnago [12] employs GAs to solve the problem. Naresh and Sharma [13] present a model based on Artificial Neural Networks (ANNs) for hydrosystem scheduling. Huang [14] proposes an optimization approach based on Ant Colony System (ACS) to enhancement of hydroelectric generation scheduling. Villasanti et al. [15] employ Multi-Objective Evolutionary Algorithms (MOEAs) to dispatch hydroelectric generating units. Musirin et al. [16] apply Ant Colony Optimization (ACO) technique to solve the economic power dispatch problem with cost minimization as objective function. Columbus et al. [17] propose the Nodal Ant Colony Optimization (NACO) technique to solve the UC problem with profit maximization as objective function. Mo et al. [18] present a hybrid algorithm based on Multi-Ant Colony System (MACS) and Adaptive Differential Evolution (ADE) for solving the short-term hydrogeneration scheduling problem.

This paper presents a comparison of two metaheuristic approaches developed to solve the ODD problem of GUs. They are based on GA, Strength Pareto Evolutionary Algorithm (SPEA), and ACO. GA is used to create and diversify the solutions' search space. SPEA is employed to select the solutions that approach Pareto Frontier. ACO is applied to explore the search space using the experience accumulated by ants.

2. Objects of Study

The objects of study of this research are two Brazilian hydroelectric plants that operate in cascade: Jupuíá (*Engenheiro Souza Dias*) and Porto Primavera (*Engenheiro Sérgio Motta*). According to the company that manages the operation of these plants, their head can be considered constant, during the day, and equal to 20 m. Figure 1 shows the operation schematic diagram of these plants. They are located at Paraná River.

Jupuíá is a run-of-river plant, with 1,551 MW of installed power and 14 GUs. The first 12 units of Jupuíá plant are connected to the 440 kV busbar and the last 2 units are

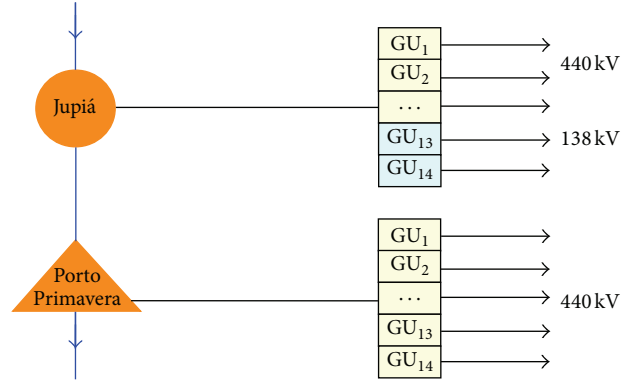


FIGURE 1: Diagram of the objects of study: Jupuíá and Porto Primavera hydroelectric plants.

connected to the 138 kV busbar. Its dam is 5,495 m long and its reservoir is 330 km².

Porto Primavera has a small capacity of storage, 618 hm³. For this reason, it is operated as a run-of-river plant. Porto Primavera plant has 1,540 MW of installed power and also 14 GUs. All of them are connected to the 440 kV busbar. Its dam, the largest in Brazil, is 10,186.20 m long and its reservoir is 2,250 km².

For Jupuíá plant, the range of operating limits of GUs 1, 3, 5, 6, 7, 8, 9, 11, 12, and 14 is 25–110.8 MW; GU 2 range is 40–110.8 MW; GU 4 can only operate 100 MW. GUs 10 and 13 range is 50–100 MW. For Porto Primavera plant, all GUs have the same operating limits: the lower is 30 MW and the upper is 110 MW.

The characteristic curves of the GUs are represented by a fourth degree polynomial. They relate efficiency and power for head = 20 m. Table 1 shows the coefficients for Jupuíá's GUs. Table 2 displays the coefficients for Porto Primavera's GUs.

3. Mathematical Formulation

3.1. Objective Functions. The proposed optimization model consists of two conflicting objectives. They are (1) maximizing the total net generation of the plant and (2) minimizing the number of times that the status of the GUs is changed. Jupuíá and Porto Primavera are individually optimized, since they are operated as run-of-river plants:

$$\begin{aligned} \text{Max } & \sum_{t=1}^{24} \sum_{u=1}^U g_u^t \eta_u^t (h_p, g_u^t), \\ \text{Min } & \sum_{t=1}^{24} \sum_{u=1}^U |y_u^{t+1} - y_u^t|, \end{aligned} \quad (1)$$

where t = index of the time period; u = index of the GU; U = total number of GUs; g_u^t = generation of the unit u , in the time period t (MW); η_u^t = efficiency of the unit u , in the time period t ; h_p = net head of the plant; and y_u^t = binary variable that indicates whether the unit u is active in the time period t (1 = active, 0 = inactive).

TABLE 1: Coefficients of the fourth degree polynomial of each GU, Jupia plant.

GU	a_4	a_3	a_2	a_1	a_0
01	-8.22E - 008	5.549E - 005	-1.24E - 002	1.03E + 000	6.45E + 001
02	5.33E - 007	-1.14E - 004	4.19E - 003	3.74E - 001	7.31E + 001
03	4.37E - 007	-7.60E - 005	-2.87E - 004	5.47E - 001	7.21E + 001
04	-4.92E - 007	1.31E - 004	-177E - 002	1.24E + 000	5.99E + 001
05	8.12E - 007	-1.93E - 004	1.21E - 002	3.53E - 002	7.82E + 001
06	3.08E - 008	3.93E - 005	-1.22E - 002	1.08E + 000	6.32E + 001
07	3.124E - 007	-5.12E - 005	-2.38E - 003	6.71E - 001	6.82E + 001
08	7.79E - 008	3.04E - 005	-1.18E - 002	1.08E + 000	6.30E + 001
09	3.62E - 007	-5.58E - 005	-2.24E - 003	6.27E - 001	7.10E + 001
10	7.58E - 008	-4.47E - 005	1.59E - 003	3.66E - 001	7.34E + 001
11	3.70E - 007	-5.96E - 005	-1.70E - 003	5.98E - 001	7.14E + 001
12	7.96E - 007	-1.88E - 004	1.16E - 002	6.08E - 002	7.78E + 001
13	-6.03E - 007	1.58E - 004	-2.00E - 002	1.33E + 000	5.82E + 001
14	3.53E - 007	-5.17E - 005	-2.81E - 003	6.62E - 001	7.01E + 001

TABLE 2: Coefficients of the fourth degree polynomial of each GU, Porto Primavera plant.

GU	a_4	a_3	a_2	a_1	a_0
01	8.97E - 007	-3.17E - 004	3.44E - 002	-1.31E + 000	1.05E + 002
02	-7.80E - 007	1.41E - 004	-1.05E - 002	5.53E - 001	7.74E + 001
03	1.60E - 006	-4.85E - 004	4.82E - 002	-1.77E + 000	1.10E + 002
04	6.74E - 007	-1.58E - 004	1.02E - 002	-2.71E - 002	8.43E + 001
05	-9.19E - 007	1.72E - 004	-1.26E - 002	5.88E - 001	7.78E + 001
06	7.99E - 007	-2.20E - 004	1.93E - 002	-5.39E - 001	9.39E + 001
07	-3.00E - 007	2.96E - 005	-1.496E - 003	2.49E - 001	8.11E + 001
08	1.11E - 006	-3.02E - 004	2.64E - 002	-7.67E - 001	9.52E + 001
09	-3.93E - 007	5.42E - 005	-4.08E - 003	3.81E - 001	7.83E + 001
10	7.47E - 007	-2.05E - 004	1.78E - 002	-4.75E - 001	9.29E + 001
11	1.03E - 006	-2.69E - 004	2.27E - 002	-6.31E - 001	9.49E + 001
12	1.22E - 006	-3.37E - 004	3.04E - 002	-9.57E - 001	9.82E + 001
13	-5.56E - 007	9.59E - 005	-7.78E - 003	5.11E - 001	7.69E + 001
14	-1.91E - 006	4.67E - 004	-4.49E - 002	2.14E + 000	4.95E + 001

3.2. *Constraints.* The optimization is subject to the following set of constraints, for each time period. Inequality (2) is the demand constraint by busbar, which states that the power generated must meet the specified load demand. According to (3), the sum of the water discharge of the units is equal to the total water discharge of the plant. Since the plants are run-of-river, the water inflow must be equal to the water outflow, water discharge plus water spillage (4). Inequalities (5) and (6) specify the lower and upper bounds of net generation, respectively:

$$\sum_{u=1}^U g_u^t \eta_u^t (h_p, g_u^t) \geq \text{Dem}^t, \quad (2)$$

$$\sum_{u=1}^U d_u^t = D^t, \quad (3)$$

$$I^t = D^t + S^t, \quad (4)$$

$$g_u^t \eta_u^t (h_p, g_u^t) \leq (\min) g_u^t \eta_u^t (h_p, g_u^t), \quad (5)$$

$$g_u^t \eta_u^t (h_p, g_u^t) \leq (\max) g_u^t \eta_u^t (h_p, g_u^t), \quad (6)$$

where Dem^t = demand of the plant, in the time period t (MW); d_u^t = water discharge of the unit u , in the time period t (m^3/s); D^t = water discharge of the plant, in the time period t (m^3/s); I_p^t = water inflow of the plant, in the time period t (m^3/s); and S^t = water spillage of the plant, in the time period t (m^3/s).

3.3. *Variables.* The integer and continuous variables of the model are represented in integrity constraints (7) and (8), respectively. The integer variables are used for the selection of GUs and the continuous variables are employed for the loading dispatch of the selected GUs:

$$y_u^t \in \{0, 1\}, \quad (7)$$

$$g_u^t \in \mathbb{R}. \quad (8)$$

TABLE 3: Solution strategy (GA + SPEA) and (GA + ACO).

Approach 1	Approach 2		Objective(s)	Dispatch
GA + SPEA	GA + ACO	Phase 1	Max plant's generation	Static (for each hour)
		Phase 2	Max plant's generation Min GUs' on/off	Dynamic (for all day)

TABLE 4: Parameters of the algorithms: GA, SPEA, and ACO.

GA		GA + SPEA		ACO	
Selection	Roulette	Selection	Elitism	α	2
Crossover	One point	Crossover	One point	β	5
Cross rate	0.9	Cross. rate	0.9	Pheromone	0.0001
Mutation	Inversion	Mutation	Inversion	Evap. rate	0.5
Mut. rate	0.1	Mut. rate	0.1	Ants	2000
Individuals	100	Individuals	100	Iterations	50
Iterations	50	Iterations	50	—	—
—	—	Ext. archive	40	—	—

4. Methodology

We propose two solution strategies using metaheuristic approaches. The first one combines GA, Holland [19], with SPEA, Zitzler et al. [20]. The second approach relates GA with ACO, Dorigo and Stützle [21]. Table 3 shows the main characteristics of these approaches.

Both approaches are divided into two phases. In Phase 1, to maximize the plant's net generation using GA, the problem is solved for each hour of the day (static dispatch). The resulting population consists of a set of individuals containing dispatch solutions for each hour of the day. These solutions are randomly combined to compose the individuals of the initial population for Phase 2.

For the first approach, Phase 2 employs SPEA. In our problem, this multiobjective algorithm searches a tradeoff between maximizing the plant's net generation and minimizing the GUs' switching on-off. The day is considered as a whole (dynamic dispatch). As a result the algorithm saves the nondominated solutions in an external archive.

For the second approach, ACO is used in Phase 2. Ants exploit the search space based on accumulated experience by them. In this approach, the dynamic dispatch is solved as a minimal cost path problem. The main objective in this phase is to minimize the GUs' switching on-off using a state transition rule. The first objective function is also taken into account since the search space consists of suboptimal solutions from Phase 1. Trade-off curve is employed to deal with both objective functions simultaneously.

5. Case Studies

The parameters used for GA, SPEA, and ACO, chosen according to literature, are shown in Table 4. In this table, α = relative importance of pheromone trail and β = relative importance of heuristic function.

We conduct case studies to the days 02/11/2012 and 01/16/2013 (chosen by the company that holds the concession

of the plants), for Jupia and Porto Primavera plants, using GA + SPEA and GA + ACO approaches. In the total there are eight case studies grouped in Frames I, II, III, and IV.

For all studies, the net generations at least meet demand; the physical, electrical, and hydraulic constraints are satisfied. Tables 5 and 6 show the results for the studies of 02/11/2012 and 01/16/2013, respectively. For each day, plant, and approach two variables are presented: number (#) of GUs' switching on-off and plant's total net generation (MW).

The better results have lower number of GUs' switching on-off and higher plant's total net generation. It is possible to compare the results just focusing on the first line (highlighted) of these tables.

In Frame I, the better results are presented by GA + SPEA, in relation to the number of startups and shutdowns of the GUs (2) and net generation of the plant (32,512.59 MW). In Frame II, although both strategies avoid GU's on-off in a perfect way (0), GA + SPEA exhibits better net generation values (33,774.55 MW). In Frame III, GA + SPEA yields higher plant's net generation value (31,949.96 MW), whereas GA + ACO yields lower number of startups and shutdowns (5). In Frame IV, again both strategies avoid GU's on-off in a perfect way (0), but GA + SPEA exhibits better net generation values (36,426.65 MW).

6. Summary and Conclusions

This paper presents metaheuristic approaches to optimize the dynamic dispatch of hydropower systems. The mathematical model consists of two conflicting objectives. It is formulated as a dynamic, mixed integer, nonlinear, nonconvex, and combinatorial optimization problem.

The solution strategies that employ GA, SPEA, and ACO consist of two phases. The first one solves the static problem for each hour of the day, in order to maximize the total net generation of the plant. The second phase is concerned with the linking hour-by-hour of the statics solutions throughout the day, setting the dynamic dispatch. Its objectives are to

TABLE 5: Results from the case study of day 02/11/2012.

Solution	Jupiá (Frame I)				Porto Primavera (Frame II)			
	GA + SPEA		GA + ACO		GA + SPEA		GA + ACO	
	# on-off	Generation (MW)	# on-off	Generation (MW)	# on-off	Generation (MW)	# on-off	Generation (MW)
1	2	32,512.59	2	31,770.43	0	33,774.55	0	32,168.20
2	3	32,626.50	3	32,247.92	2	33,777.07	2	32,219.96
3	4	32,970.51	5	32,324.27	—	—	4	33,313.23
4	5	32,976.89	—	—	—	—	—	—

TABLE 6: Results from the case study of day 01/16/2013.

Solution	Jupiá (Frame III)				Porto Primavera (Frame IV)			
	GA + SPEA		GA + ACO		GA + SPEA		GA + ACO	
	# on-off	Generation (MW)	# on-off	Generation (MW)	# on-off	Generation (MW)	# on-off	Generation (MW)
1	10	31,949.96	5	30,212.20	0	36,426.65	0	35,147.76
2	12	31,978.13	6	30,463.18	—	—	2	35,187.10
3	14	31,986.00	9	30,528.50	—	—	—	—
4	—	—	10	30,819.07	—	—	—	—

maximize the total net generation of the plant and to reduce the number of startups and shutdowns of the units.

The proposed approaches are applied to two hydroelectric plants that operate in cascade: Jupiá and Porto Primavera plants. Eight case studies are carried out for two days of these two plants, comparing GA + SPEA and GA + ACO strategies.

For the case studies of this research, on the whole, GA + SPEA approach shows better results for both objectives functions of the problem. This can be seen in Frames I, II, and IV where the higher net generation values and lower number of startups and shutdowns are in GA + SPEA column. Besides, in general, GA + SPEA presents better result in terms of plant's net generation and GA + ACO exhibits better performance in relation to GU's switching on-off, as shown in Frame III. That probably occurs because, in Phase 2, SPEA deals with both objectives of the problem in a simultaneous way, since it is a multiobjective algorithm, whereas ACO focuses on the second objective, minimizing GU's on-off, although the first objective is also taken into account in a preemptive way.

In conclusion, both solution strategies, GA + SPEA and GA + ACO, are good alternatives to solve the optimal dynamic dispatch in the short-term operation of hydroelectric plants. As future work, the authors propose to run the models several times to collect an expressive number of case studies. The goal will be to apply statistical analyses in a bigger sample to compare the models in a more accurate way.

Conflict of Interests

The authors declare that there is no conflict of interests regarding the publication of this paper.

Acknowledgments

The research reported herein was supported by three Brazilian Government agencies and one of the largest power generating companies. They are *Conselho Nacional de Desenvolvimento Científico e Tecnológico* (CNPq), *Coordenação de Aperfeiçoamento de Pessoal de Nível Superior* (CAPES), *Agência Nacional de Energia Elétrica* (ANEEL), and *Companhia Energética de São Paulo* (CESP), respectively.

References

- [1] I. G. Hidalgo, D. G. Fontane, J. E. Lopes, J. G. Andrade, and A. F. de Angelis, "Efficiency curves for hydroelectric generating units," *Journal of Water Resources Planning and Management*, vol. 140, no. 1, pp. 86–91, 2014.
- [2] J. Yi, J. W. Labadie, and S. Stitt, "Dynamic optimal unit commitment and loading in hydropower systems," *Journal of Water Resources Planning and Management*, vol. 129, no. 5, pp. 388–398, 2003.
- [3] A. Arce, T. Ohishi, and S. Soares, "Optimal dispatch of generating units of the Itaipu hydroelectric plant," *IEEE Transactions on Power Systems*, vol. 17, no. 1, pp. 154–158, 2002.
- [4] E. C. Finardi and M. R. Scuzziato, "Hydro unit commitment and loading problem for day-ahead operation planning problem," *International Journal of Electrical Power & Energy Systems*, vol. 44, no. 1, pp. 7–16, 2013.
- [5] J. P. S. Catalão, S. J. P. S. Mariano, V. M. F. Mendes, and L. A. F. M. Ferreira, "Parameterisation effect on the behaviour of a head-dependent hydro chain using a nonlinear model," *Electric Power Systems Research*, vol. 76, no. 6-7, pp. 404–412, 2006.
- [6] O. Nilsson, L. Söder, and D. Sjelvgren, "Integer modelling of spinning reserve requirements in short term scheduling of

- hydro systems,” *IEEE Transactions on Power Systems*, vol. 13, no. 3, pp. 959–964, 1998.
- [7] A. Borghetti, C. D’Ambrosio, A. Lodi, and S. Martello, “An MILP approach for short-term hydro scheduling and unit commitment with head-dependent reservoir,” *IEEE Transactions on Power Systems*, vol. 23, no. 3, pp. 1115–1124, 2008.
- [8] G. W. Chang, M. Aganagic, J. G. Waight et al., “Experiences with mixed integer linear programming based approaches on short-term hydro scheduling,” *IEEE Transactions on Power Systems*, vol. 16, no. 4, pp. 743–749, 2001.
- [9] J.-P. Chancelier and A. Renaud, “Daily generation scheduling: decomposition methods to solve the hydraulic problems,” *International Journal of Electrical Power & Energy Systems*, vol. 16, no. 3, pp. 175–181, 1994.
- [10] E. F. Santos and T. Ohishi, “A hydro unit commitment model using genetic algorithm,” in *Proceedings of the Congress on Evolutionary Computation (CEC '04)*, vol. 2, pp. 1368–1374, IEEE, June 2004.
- [11] G. Muller, *Dispatch of generating units and generation of individual hydroelectric using genetic algorithm [M.S. thesis]*, Federal University of Rio de Janeiro, Rio de Janeiro, Brazil, 2010.
- [12] G. R. Colnago, *Contribution for turbines optimization in hydroelectric plants: specification and operation [Ph.D. thesis]*, State University of Campinas, São Paulo, Brazil, 2011.
- [13] R. Naresh and J. Sharma, “Hydro system scheduling using ANN approach,” *IEEE Transactions on Power Systems*, vol. 15, no. 1, pp. 388–395, 2000.
- [14] S.-J. Huang, “Enhancement of hydroelectric generation scheduling using ant colony system based optimization approaches,” *IEEE Transactions on Energy Conversion*, vol. 16, no. 3, pp. 296–301, 2001.
- [15] C. M. Villasanti, C. V. Lucken, and B. Baran, “Dispatch of hydroelectric generating units using multiobjective evolutionary algorithms,” in *Proceedings of the IEEE/PES Transmission & Distribution Conference & Exposition: Latin America*, pp. 929–934, São Paulo, Brazil, 2004.
- [16] I. Musirin, N. H. F. Ismail, M. R. Kalil, M. K. Idris, T. K. A. Rahman, and M. R. Adzman, “Ant Colony Optimization (ACO) technique in economic power dispatch problems,” in *Trends in Communication Technologies and Engineering Science*, P.-K. A. Wai, X. Huang, and S.-I. Ao, Eds., vol. 33, chapter 15, pp. 191–203, Springer Netherlands, 2009.
- [17] C. C. Columbus, K. Chandrasekaran, and S. P. Simon, “Nodal ant colony optimization for solving profit based unit commitment problem for GENCOs,” *Applied Soft Computing Journal*, vol. 12, no. 1, pp. 145–160, 2012.
- [18] L. Mo, P. Lu, C. Wang, and J. Zhou, “Short-term hydro generation scheduling of Three Gorges-Gezhouba cascaded hydropower plants using hybrid MACS-ADE approach,” *Energy Conversion and Management*, vol. 76, pp. 260–273, 2013.
- [19] J. H. Holland, *Adaptation in Natural and Artificial Systems*, The University of Michigan Press, Ann Arbor, Mich, USA, 1975.
- [20] E. Zitzler, M. Laumanns, and L. Thiele, “SPEA2: improving the strength pareto evolutionary algorithm,” Tech. Rep. TIK-103, Department of Electrical Engineering, Swiss Federal Institute of Technology, Zürich, Switzerland, 2001.
- [21] M. Dorigo and T. Stützle, *Ant Colony Optimization*, A Bradford Book, The MIT Press, 2004.

Research Article

Coincidence Detection Using Spiking Neurons with Application to Face Recognition

Fadhlan Kamaruzaman, Amir Akramin Shafie, and Yasir M. Mustafah

Department of Mechatronics Engineering, International Islamic University Malaysia, P.O. Box 10, 50728 Kuala Lumpur, Malaysia

Correspondence should be addressed to Amir Akramin Shafie; aashafie@iium.edu.my

Received 24 February 2015; Revised 22 April 2015; Accepted 12 May 2015

Academic Editor: Wei Fang

Copyright © 2015 Fadhlan Kamaruzaman et al. This is an open access article distributed under the Creative Commons Attribution License, which permits unrestricted use, distribution, and reproduction in any medium, provided the original work is properly cited.

We elucidate the practical implementation of Spiking Neural Network (SNN) as local ensembles of classifiers. Synaptic time constant τ_s is used as learning parameter in representing the variations learned from a set of training data at classifier level. This classifier uses coincidence detection (CD) strategy trained in supervised manner using a novel supervised learning method called τ_s Prediction which adjusts the precise timing of output spikes towards the desired spike timing through iterative adaptation of τ_s . This paper also discusses the approximation of spike timing in Spike Response Model (SRM) for the purpose of coincidence detection. This process significantly speeds up the whole process of learning and classification. Performance evaluations with face datasets such as AR, FERET, JAFFE, and CK+ datasets show that the proposed method delivers better face classification performance than the network trained with Supervised Synaptic-Time Dependent Plasticity (STDP). We also found that the proposed method delivers better classification accuracy than k nearest neighbor, ensembles of k NN, and Support Vector Machines. Evaluation on several types of spike codings also reveals that latency coding delivers the best result for face classification as well as for classification of other multivariate datasets.

1. Introduction

Donald Hebb first proposed that if the synapses between two neurons effectively cooperate in an activity then the synaptic efficacy of the synapse would be strengthened. Since the cooperativeness between these neurons would be more effective if it happens within a specific period of time, the idea of “Hebbian Plasticity” could also be considered as a form of coincidence detection or neuronal synchronization between the inputs of the two neurons. Previous studies show that thalamic synchronization has significant impact on cortical responsiveness and suggest that coincidence detection plays a critical role in the sensory information transmission between different brain’s regions [1] as well as in phosphoinositide signaling [2]. Subsequently, the resulting Long-Term Potentiation (LTP), a phenomenon in which synaptic strength is enhanced following bursts of synaptic activity, is vital for learning and memory [3].

In this paper, we discuss two ways of learning and classification by coincidence detections, namely, (1) learning

by weight adaptation in the form of Supervised STDP and (2) learning by synaptic time constant adaptation in the form of a novel approach called τ_s Prediction. These two strategies are both based on Hebbian plasticity but their implementations are quite different. Here supervised learning rules are used to form the necessary synaptic weights or synaptic time constant that represent the training data and then the trained network is used for classification.

In learning stage, the network is presented with set of positive (negative) samples, and the network will be allowed certain amount of time to fire spikes. If the designated neurons fail to fire spikes, the weights or synaptic time constant will be adjusted accordingly based on the desired spike timing. This strategy would result in higher (lower) weights or synaptic time constants for neurons that barely (easily) fire. In face identification, similar faces compete more than dissimilar faces; thus this strategy would enforce stricter conditions for spike firing on neurons dedicated to facial regions with high degree of similarity. This is done by imposing smaller weights or synaptic time constant on the synaptic

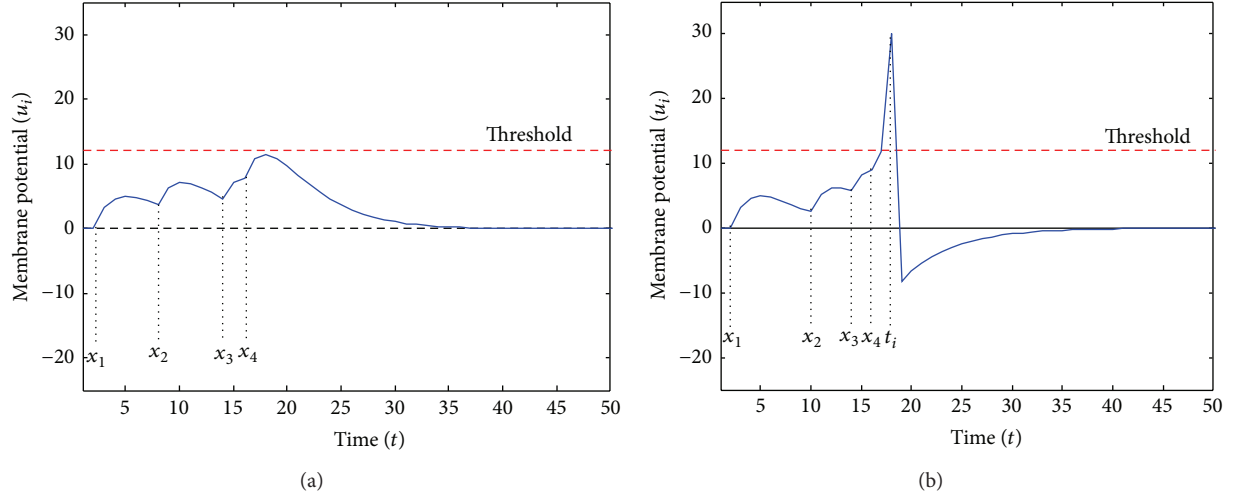


FIGURE 1: The membrane potential $u_i(t)$ for different sets of inputs x_n : (a) the output is $ED_4(x_1, x_2, x_3, x_4) = 0$, and (b) the output is $ED_4(x_1, x_2, x_3, x_4) = 1$ since $|x_4 - x_3| \leq c_1$.

connections. The restrictions would ensure that only highly similar facial regions would cause firing in output neuron. On the other hand, the process would also impose looser restrictions on dissimilar facial regions.

Coincidence detection strategy in practice would cause neurons connected to similar faces to fire more easily and vice versa; thus, based on coincidence detection and input synchrony point of view, it can be hypothesized that if the synaptic connection between presynaptic input pair of similar face requires larger weight or larger synaptic time constant to facilitate output spike firing, it signifies that the input pairs are connected to the facial area which possesses smaller discriminative capacity for face recognition.

Implicitly, to realize this hypothesis, it is thus assumed that (1) human beings exhibit similar intrapersonal variations, and thus (2) the learned weights and synaptic time constant from set of generic face samples could represent the actual variations that might appear on the unseen face samples.

2. Related Works

In this section we review briefly the idea of coincidence detection as proposed by Maass [4]. Then we highlight several supervised spiking neural network (SNN) learning methods. Subsequently, we discuss the basics of Spike Response Model (SRM) used in this paper. Finally, we take a closer look on multilayer supervised learning algorithm based on Synaptic-Time-Dependent Plasticity (STDP) approach proposed by Sporea and Grüning [5].

2.1. Coincidence Detection Overview. Spiking neurons can act as a coincidence detector for incoming input pulses by relaying the synchronized synaptic inputs and exact timing of spikes [4, 6, 7]. Studies of the somatosensory [8] and visual systems [9] suggested that neuronal synchronization is critical in transmitting sensory information. This relies on the

fact that synchronous inputs signals are more effective in producing higher firing rates of output spikes than asynchronous inputs signals.

Assuming the input pulses received are encoding some set of numbers, the coincidence detection can determine whether some of these numbers have equal or almost equal values. This operation if carried out on more traditional type of ANN is actually very expensive [4]. By the description of the basic idea of coincidence detection by spiking neurons [4], an output neuron i would not fire if the input neurons j fire at a temporal distance of $\geq c_2$ but it will fire when the input neurons j fire at a temporal distance of $\leq c_1$. If a set of n input neuron j is used to encode n real numbers x_1, x_2, \dots, x_n , the firing patterns $\{0 \text{ or } 1\}$ of output neuron i denoted as ED_n can be used to decode the input. For example, two cases, namely, $ED_4 = 0$ and $ED_4 = 1$, are shown in Figure 1.

Recent work showed that a simple SNN model constructed by integrate-and-fire neurons and single coincidence-detector neuron can precisely read out subthreshold noisy signal [10]. The authors highlight that the two important parameters that will determine reliability and precision of the coincidence detection of the input pulses are the detection time window which can be manipulated by τ_s and the threshold. They suggest that it is possible to obtain as much as 100% reliability of the outputs by having an optimal pair of the detection time window and the threshold.

2.2. Supervised Learning Methods for SNN. Supervised learning for SNN is usually performed based on the traditional gradient descent techniques. However, due to nature of spiking neurons timing, some modifications or special methods are introduced for dealing specifically with this temporal adaptation problem. Some popular methods of supervised learning in SNN includes learning method designed specifically for SNN based on the gradient descent by backpropagation of error called SpikeProp [11, 12], and Remote Supervised Method (ReSuMe) [13]. Later, Sporea and Grüning [5] extend

ReSuMe into multilayer supervised learning algorithm based on STDP where results of benchmarks on XOR problem and Iris dataset reveal successful implementation of the algorithm as well as the flexibility of this learning rule to learn different spike coding and timing patterns.

Recently an SNN learning rule called Chronotron is proposed by Florian [14]. Xu et al. [15] then proposed a supervised multispike learning rule with temporal coding based on gradient descent that aims to solve the problem of error function construction and interference among multiple output spikes during learning. Another learning rule, called Spike Pattern Association (SPAN) [16], is based on Widrow-Hoff learning rule and temporal coding that can associate multiple spatiotemporal spike patterns to desired output spike pattern. Other methods also include statistical method [17, 18], linear algebra method [19], evolutionary method [20], and Analog Spiking Neuron Approximation Backpropagation (ASNAProp) [21].

2.3. Spike Response Model. The formulation of spiking neuron behavior in SNN implementation described by integrate and fire model can be further simplified and represented by SRM [22]. Let w_{ij} be the weight between postsynaptic neuron i and presynaptic neuron j , τ_s is the synaptic time constant, τ_{rec} is recovery time constant, I^{ext} is the external current, t_j^f is the time of presynaptic spikes, and \hat{t}_i is time of output spike, while η , ϵ_{ij} , and κ_{ij} are kernels, $\delta(t)$ is Dirac delta function, and $s = t - t_j^f$. According to [22] the state of membrane potential $u_m(t)$ can be computed from (1) where the kernel ϵ_{ij} is an alpha function computed from (2):

$$u_m(t) = \eta(t - \hat{t}_i) + \sum_j w_{ij} \sum_f \epsilon_{ij}(t - \hat{t}_i, s) \quad (1)$$

$$+ \int_0^\infty \kappa_{ij}(t - \hat{t}_i, s) I^{ext}(t - s) ds,$$

$$\epsilon_{ij}(s) = \frac{s}{\tau_{s,ij}} \exp\left(1 - \frac{s}{\tau_{s,ij}}\right). \quad (2)$$

In SRM, each incoming spike from neuron j at time t_j^f will perturb u_m to produce presynaptic potentials (PSP) and the time course of u_m as a result of the perturbation is defined by the kernel ϵ_0 . If after the summation of PSPs u_m reaches the threshold v , output spike at time \hat{t}_i is therefore triggered. The form of the spike and the after-spike potential is described by kernel η . Then the zero order SRM can be constructed by neglecting the dependence of and upon the $t - \hat{t}_i$ argument, so the kernels ϵ_{ij} and κ_{ij} are set so that $\epsilon_0(s) = \epsilon_{ij}(\infty, s)$ and $\kappa_0(s) = \kappa_{ij}(\infty, s)$, respectively. Assuming that there is no external current discharged into the neuron, we let $I^{ext} = 0$, so now (1) becomes:

$$u_m(t) = \eta(t - \hat{t}_i) + \sum_j w_{ij} \sum_f \frac{s}{\tau_{s,ij}} \exp\left(1 - \frac{s}{\tau_{s,ij}}\right). \quad (3)$$

Therefore each presynaptic spike evokes a PSP with the same time course, independent of the index j of the

presynaptic neuron and independent of the last firing time \hat{t}_i of the postsynaptic neuron. Thus the synaptic efficacies w_{ij} and τ_s are the parameters that are responsible to scale the amplitude of the PSPs and their ‘‘effective time interval,’’ respectively.

2.4. Supervised STDP Learning Method. Using neurons described by SRM model in fully connected feed-forward SNN with single hidden layer, this learning rule is based on backpropagation of error [5]. The error is defined as the difference between the actual firing rate and target firing rate for all neurons. It is similar to the standard backpropagation in discrete time but derived as a functional derivative in continuous time. Assuming that the neuron has only single spike train, according to the STDP learning [22–25], the weight change between output and hidden neurons Δw_{oh} and between n_h hidden neurons and n_i input neurons Δw_{hi} can be described as

$$\Delta w_{oh} = \frac{1}{n_h} \left(A_+ \exp \frac{t_h - t_d}{\tau_+} - A_+ \exp \frac{t_h - t_o}{\tau_+} \right), \quad (4)$$

$$\Delta w_{hi} = \frac{1}{n_h n_i} |w_{oh}| \left(A_+ \exp \frac{t_i - t_d}{\tau_+} - A_+ \exp \frac{t_i - t_o}{\tau_+} \right),$$

where $A_+ > 0$ is the amplitude, $\tau_+ > 0$ is the time constant, t_h is hidden neuron firing time, t_i is input neuron firing time, t_o is output neuron firing time, and t_d is target neuron firing time. Note that the weight modification rules do not depend on the specific dynamics of the neuron model but only depend on the target, output, and input firing time thus making it applicable to any neuron model.

3. Detailed Description on Coincidence Detection

To illustrate several cases of coincidence detections under different variants of learning parameters such as synaptic time constant τ_s , weight w , and threshold v , consider two presynaptic inputs from 2 presynaptic neurons $j = 1$ and $j = 2$ fired at times t_1^f and t_2^f , respectively, where $t_2^f \geq t_1^f$, having temporal distance between inputs $d = t_2^f - t_1^f$, $d > 0$ were propagated into a coincidence detection (CD) neuron. Under different values of learning variables, these two presynaptic inputs can either (1) invoke a spike or more than one spike (2) or none at all at the CD neuron. Since d is effectively determined by the spatiotemporal pattern of the input, then the objective of a CD neuron would be to facilitate an output spike at only certain range of d and depress firing at other instances of d .

However, in order to achieve the specified objective of coincidence detection, behaviors of learning parameters such as τ_s , w , and v need to be closely examined. Descriptions on a few possible coincidence detection outcomes of presynaptic inputs $t_1^f = 2$ ms and $t_2^f = 8$ ms (thus $d = 6$ ms) with respect to different learning parameters are shown in Figure 2. All spikes generated using SRM model with fixed threshold.

Consider the maximum amplitude of PSP evoked by the first presynaptic input, conveniently denoted afterwards as

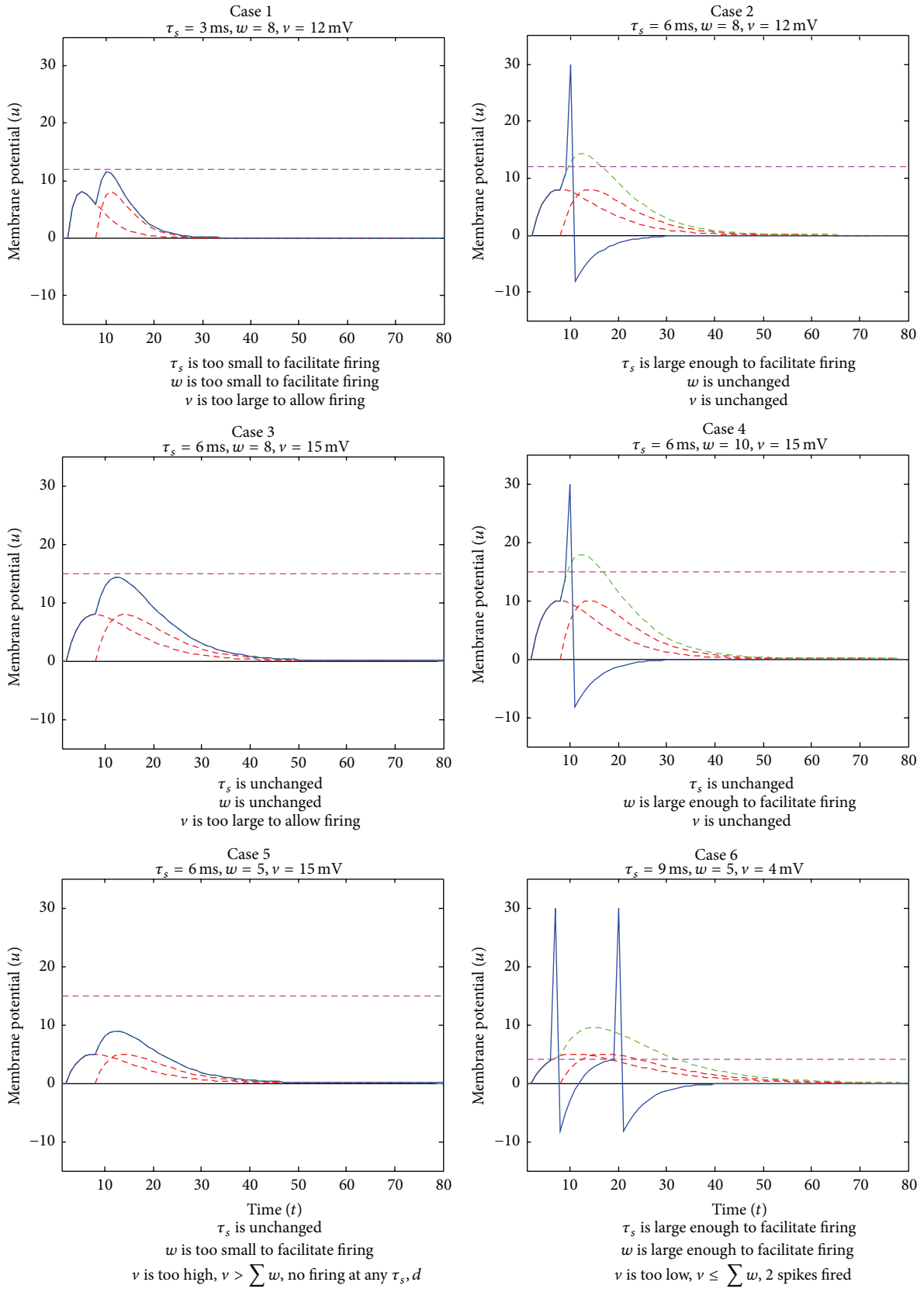


FIGURE 2: Several cases of coincidence detection between two presynaptic inputs.

PSP_{1,max}, the weight w , and synaptic time constant τ_s . From (2), the time at which PSP₁ would reach its peak $t_{1,max}$ can be defined as $t_{1,max} = t_1^f + \tau_s$. Since $s = (t_1^f + \tau_s) - t_1^f = \tau_s$, then (2) can be written as

$$\epsilon(\tau_s) = \frac{\tau_s}{\tau_s} \exp\left(1 - \frac{\tau_s}{\tau_s}\right) = 1. \quad (5)$$

Thus, the PSP_{1,max} can be denoted as

$$\text{PSP}_{1,max} = w \cdot \epsilon(\tau_s) = w. \quad (6)$$

For a CD neuron receiving two presynaptic spikes at a time, to ensure appropriate firing while avoiding firing facilitated by only single presynaptic spike, the proper selection of threshold should follow $\sum w \geq v > w$. It is assumed that there exists a minimum required synaptic time constant $\tau_{s,min}$ that would cause a CD neuron to fire a spike. For any value of τ_s larger than $\tau_{s,min}$ it would definitely cause the CD neuron to fire, but with a larger delay. This can be summarized in

$$\text{Neuron spike} \begin{cases} \delta(t_i) = 1, & \text{if } \tau_{s,min} \leq \tau_s < \infty \\ \delta(t_i) = 0, & \text{if } \tau_{s,min} > \tau_s \geq 1. \end{cases} \quad (7)$$

There are two distinctive regions which can be defined for the firing behavior of a CD neuron. These two regions are (1) firing region (FG) and (2) nonfiring region (NFG). These regions are illustrated in Figure 3. According to Figure 3, there is 100% probability that any PSP that are strong enough to cause a CD neuron to fire would reach the threshold in FG region, while, in NFG, any neuron that failed to fire in FG region would absolutely not be able to fire in NFG region. The two NFG regions are discontinued by an FG region, where $t_{fg} - t_2^f$ signifies the maximum time interval of FG region. The boundaries for these distinctive regions are given in the following equation, where we defined $t_{fg} = \tau_s + t_2^f$:

$$\text{FG} = \{t_2^f, t_{fg}\}, \quad (8)$$

$$\text{NFG} = \{0, t_2^f\}, \{t_{fg}, \infty\}.$$

Consider if threshold v is set at the highest possible value such that $v = 2w$, for this threshold, only PSP resulting from two presynaptic spikes fired at the same time can reach it, where $t^f = t_1^f = t_2^f$. Based on (3), assuming that the CD neuron is allowed to fire only once, the refractory kernel $\eta(t - \hat{t}_i)$ can be set to be fixed at $\eta_0 \leq 0$. Let $s = (t - t^f)/\tau_s$ and $\eta_0 = 0$; since $t^f = t_1^f = t_2^f$, (3) can be written as (9). For complete calculation readers are referred to Appendix A. Consider

$$\ln(s) - s + 1 - \ln\left(\frac{u_m}{2w}\right) = 0. \quad (9)$$

As $\ln(s) - s$ is analytically unsolvable, we can use numerical approximation of function of $\ln(s) - s + 1 - \ln(u_m/2w) = 0$ for $s = [0, 1]$, where solution for s is found as $s = 1$; hence $t = \tau_s + t^f$. Since $t^f = t_1^f = t_2^f$, and any PSP that occurs before t_2^f would yield a lower membrane potential, thus the maximum achievable membrane potential for this coincidence neuron would happen before or precisely at $\tau_s + t_2^f$.

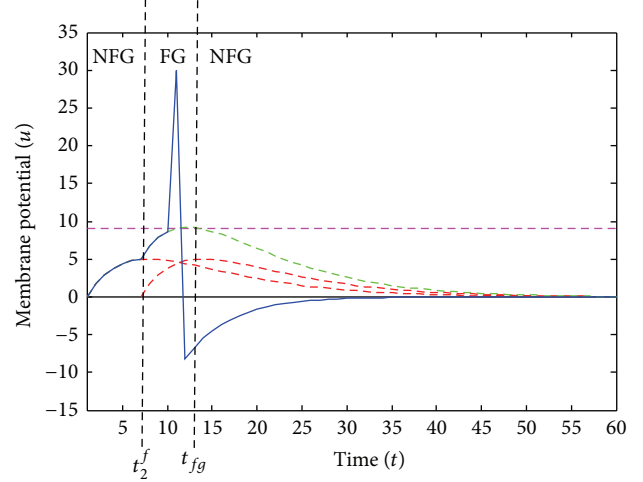


FIGURE 3: Illustration on firing region and nonfiring region of a CD neuron receiving 2 presynaptic spikes at $t_1^f = 0$ ms and $t_2^f = 7$ ms.

4. Proposed Method

4.1. Output Spike Time Prediction. One major problem of any spiking neuron model is the processing time taken to evaluate the exact level of membrane potential prior to any spike triggering. According to Makino [26] it is difficult to predict firing for a complex neuron such as SRM model since it involves delayed-firing and causality. Furthermore, approximation methods such as firing time prediction can be inexact while exact simulation is limited to simple models [27]. Makino [26] proposes an event-driven SRM using incremental partitioning method which uses linear envelopes of the state variable of a neuron to partition the simulated time. This would cause the firing time to be reliably calculated by implementing the bisection-combined Newton-Raphson method to each resulting partition.

In discrete-time approach, the system needs to compute accurately the level of membrane potential in each discrete time and also to update the state variables for precise output spike timing. If the numbers of discrete intervals σ (which is also known as sampling rate, f_s in continuous-to-discrete signal conversion) between specific period of time Δt are large, then the evaluations would take considerably large amount of time. One way to overcome this problem is by reducing the number of σ but this would reduce the precision of the resulting output spike timing. Here we propose an approximation method called Output Spike Time Prediction (OSTP) SRM to solve this problem.

Consider the simplified SRM model in (3) where the output neuron i is assumed to receive two presynaptic inputs from two presynaptic neurons $j = 1$ and $j = 2$ at two different times t_1^f and t_2^f where $t_2^f > t_1^f$. The objective of OSTP is to find the estimated spike time $t_{i,est}$ of the output neuron. For convenience, let $s_j = (t - t_j^f)/\tau_s$ and $\eta(t - \hat{t}_i) = \eta_0$ so that (3) now becomes

$$u_m(s) - \eta_0 = w [s_1 \cdot \exp(1 - s_1) + w [s_2 \cdot \exp(1 - s_2)]. \quad (10)$$

Then, let $a = t_2^f - t_1^f$; thus $t_2^f = a + t_1^f$; consequently, $s_2 = s_1 - (a/\tau_s)$. Thus, we can write (10) as (11). For simplification of notation, let $A = \exp(1)[1 + \exp(a/\tau_s)]$ and $B = [(a/\tau_s) \cdot \exp(1 + (a/\tau_s))]$ so that the OSTP equation can be described in (12). For complete calculation readers are referred to Appendix B. Then, using the numerical approximation as discussed previously to solve for s_1 , the estimated time of spike t_{est} can be obtained using (13). For $t_1^f = 1$ ms, $t_2^f = 3$ ms, and $\tau_s = 5$, $s_1 = [0 \ 5]$ plot of OSTP equation in (12) with 10 equally spaced values of the term $(u - \eta_0)/w$ from 0 until 3 is illustrated in Figure 4:

$$\frac{u - \eta_0}{w} = s_1 \cdot \exp(-s_1) \cdot \exp(1) \left[1 + \exp\left(\frac{a}{\tau_s}\right) \right] \quad (11)$$

$$- \exp(-s_1) \left[\frac{a}{\tau_s} \cdot \exp\left(1 + \frac{a}{\tau_s}\right) \right],$$

$$\exp(-s_1) (A \cdot s_1 - B) - \frac{u - \eta_0}{w} = 0, \quad (12)$$

$$t_{\text{est}} = s_1 \cdot \tau_s + t_1^f. \quad (13)$$

From Figure 4, several lines manage to cross 0 while others do not, which indicates that no solution of s_1 could be obtained. The lines that cross 0 (blue lines) are drawn from variables that would produce spike firings while others that do not cross (red-dashed lines) are drawn from variables that would not produce any spike firing. Thus, the precise spike firing time can be approximated given that the numbers of discrete intervals between the boundaries of s_1 are sufficient to provide precise estimation. Similar to discrete estimation case, OSTP relies on discrete intervals σ_{OSTP} between Δs_1 in order to produce accurate estimation. However, discrete intervals between Δs_1 in OSTP do not have significant effect on the overall processing time unlike discrete-time which will be seen later.

4.2. Output of Coincidence Detection Network. As explained earlier, any sufficiently close pair of presynaptic inputs would produce output spikes. However, for reliable and accurate output spikes, two additional spikes or ‘‘cues’’ called the start cue and end cue are added for each output spike train. These two cues indicate the start and end of CD neuron simulation. Without start cue, the firing delay of each occurring spike cannot be accurately determined. The significance of the start cue has been discussed at length in literatures [11, 28]. The time of start cue is kept when the first presynaptic spike arrives at CD neuron. In contrast, without end cue, some meaningful information encoded by presynaptic spikes that are unable to evoke any output spike would be lost and this would affect the spike coding accuracy.

Another important element which is particularly important for STDP supervised learning is ‘‘imaginary spike.’’ It is important to mention that imaginary spike is not used for classification; however it is used to compute error signal for supervised adjustment of the weight. This imaginary spike

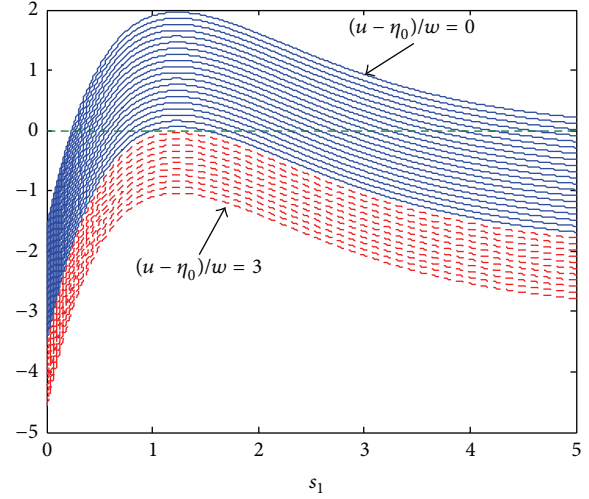


FIGURE 4: Visualization of OSTP equation with 10 equally spaced values of $(u - \eta_0)/w$ between $[0 \ 3]$ for $t_1^f = 1$ ms, $t_2^f = 3$ ms, and $\tau_s = 5$, $s_1 = [0 \ 5]$.

indicates the end of a designated time t_{deg} if a presynaptic input fails to produce a spike within certain period. As shown earlier, the maximum time for presynaptic input pair to attain the highest membrane level and evoke a spike is $t_{fg} = \tau_s + t_2^f$ so the designated time t_{deg} for a spike to fire is set slightly larger than t_{fg} , where

$$t_{\text{deg}} = 2\tau_s + t_2^f. \quad (14)$$

Note that the presynaptic inputs only maintain the temporal integrity of the input, while the spatial integrity is embedded into the spatial location \mathcal{L} of the presynaptic neuron. To achieve spatiotemporally reliable output spike pattern, it is vital to sequence the presynaptic inputs. This process is carried out by allowing only single pair of presynaptic inputs from neurons sharing the same spatial location to take part in evoking output spike at one time. After an output or imaginary spike is produced, another pair from next location is allowed to take part in evoking spike, if any. This process is repeated until the end of simulation; that is, all presynaptic inputs have taken part in evoking output spike.

In this implementation, the computation of exact membrane potential and the term $\eta(t - \hat{t}_i)$ would slow the whole network down. Thus, for simplicity, the current level of membrane potential u_m (for spiking case) and the membrane reset term $\eta(t - \hat{t}_i)$ (for nonspiking case) just before next presynaptic input pair takes part in evoking the output spike are changed to membrane reset constants $\eta_o = \eta_{\text{no spike}}$ and $\eta_o = \eta_{\text{spike}}$, respectively, with respect to (10). This is actually feasible assuming that both spiking and nonspiking cases of coincidence detection are producing spikes (actual and imaginary spikes). The output spike train of a CD neuron using continuous SRM, discrete-time SRM, and OSTP SRM in a CD classification network accepting 9 presynaptic input pairs is shown in Figure 5, where the parameters used are $w = 5$, $\tau_s = 3$ ms, $v = 7$ mV, $\eta_{\text{no spike}} = 2$ mV, and $\eta_{\text{spike}} = -2$ mV.

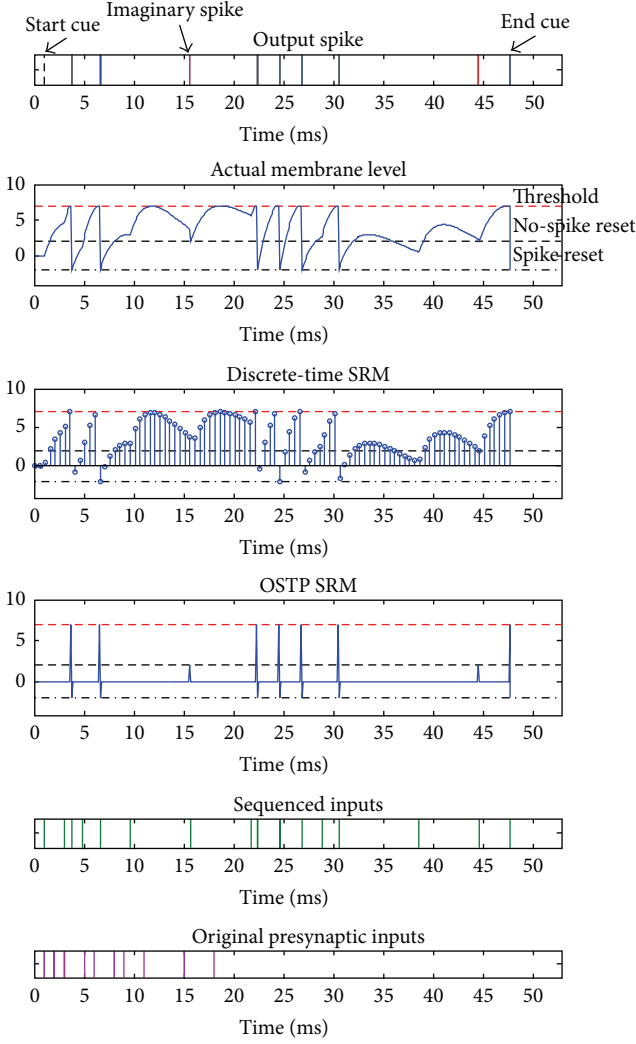


FIGURE 5: Precise spike firing time at a CD neuron by continuous SRM ($\sigma_{\text{disc}} = 100$ ms, providing almost actual membrane level for comparison), discrete-time SRM ($\sigma_{\text{disc}} = 2$ ms), and OSTP SRM ($\sigma_{\text{OSTP}} = 10$) approximation in CD SNN classification.

Based on Figure 5 each bar represents the precise timing of output spikes (blue), imaginary output spikes (red), cues (dashed black), sequenced presynaptic inputs (green), and original presynaptic inputs (purple). The resulting output spikes for these 3 approaches are exactly the same. Imaginary output spikes are needed specifically to train the network by Supervised STDP approach and are not used for classification. There are 2 cues (start and end (cooccurring at the end of output spike)), and 7 spikes and 2 imaginary spikes are produced by the CD neuron.

The numbers of actual spikes are generally less than the number of presynaptic input pairs; however the number of total spikes (actual + imaginary) would be equal to the number of presynaptic input pairs. Note that the original presynaptic inputs do not have spatial integrity intact since they share several instances of similar presynaptic spike time and tend to clutter together in temporal neural network.

The temporal sequencing of input makes use of spatial locations by temporally rearranging the presynaptic inputs. Furthermore, it can be observed that the OSTP SRM implementation produces identical spikes as discrete-time SRM.

4.3. Learning Process for Coincidence Detection. We propose a novel learning approach called τ_s Prediction, which is carried out by approximating the required synaptic time constant to produce an output spike. Unlike Supervised STDP in [5], this learning process only requires positive (+1) class sample.

The main objective of τ_s is much simpler than Supervised STDP, that is, to evoke small-delayed spike in matching sample. Additionally, this process is assumed to be able to implicitly depress the spike or delay it longer for nonmatching sample, given that the temporal distances between the input pairs are greater than a certain range. Since changes in τ_s could facilitate, depress, or delay the output spike, using as τ_s learning parameter should allow this type of training in coincidence detection spiking neural network.

Assume that the training process needs to approximate the value of τ_s that would allow a pair of inputs t_1^f and t_2^f from matching face to evoke a spike at CD neuron output at desired time $t = t_d$. By letting $X = 1/\tau_s$, from (10) we can have (15). For complete calculation readers are referred to Appendix C. Then, X can be solved by finding the zero crossing using the numerical approximation discussed earlier. After that, we can compute the approximation of synaptic time constant $\tau_{s,\text{approx}}$ using (16). Finally, the change in synaptic time constant $\Delta\tau_{s,m,n}$ for each pixel n belongs to local patch m such that $n \in m$ can be computed using (17):

$$X \left[(t_d - t_1^f) \cdot \exp(1) \exp(- (t_d - t_1^f) (X)) + (t_d - t_2^f) \cdot \exp(- (t_d - t_2^f) (X)) \right] - \frac{u - \eta_0}{w} = 0, \quad (15)$$

$$\tau_{s,\text{approx}} = \frac{1}{X}, \quad (16)$$

$$\Delta\tau_{s,m,n} = \frac{A_+}{KK_+} \sum_{k=1}^K \sum_{k_+=1}^{K_+} \tau_{s,\text{approx}}, \quad (17)$$

where K is total number of training subjects (classes), K_+ is positive sample per training subject, and A_+ is learning constant. Since the teacher signal $t_d = t_2^f + \tau_s$ depends on the current state of τ_s , it would evolve along the training process allowing it to have dynamic behavior. Additionally, there are instances of function in (15) where the plot does not produce any zero crossing, similar to no-solution case shown in Figure 5. Therefore, the approximated τ_s can take the value of $t_2^f - t_1^f$ since the minimum synaptic time constant τ_s required to evoke the spike in a CD neuron is less than or equal to $t_2^f - t_1^f$ as proven in Appendix D. Since this approach only involves estimation based on positive samples, the corresponding spike error e for τ_s Prediction can be given

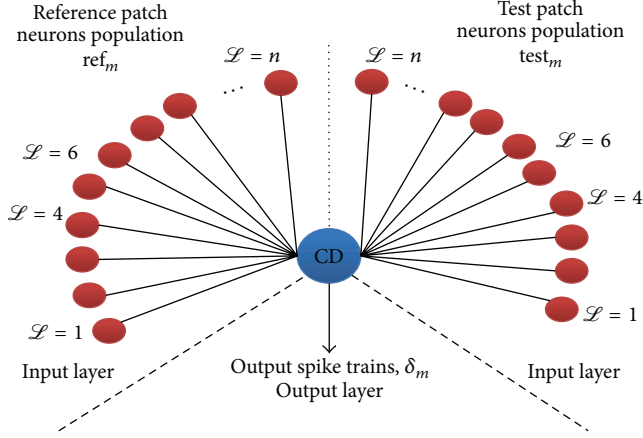


FIGURE 6: Illustration of a CD neuron (center) attached to single patch of face receiving presynaptic inputs attached to locally lateral LP m from gallery face and probe face. Each neuron connected to the CD neuron patch assumes spatially different input \mathcal{L} to ensure that spatiotemporal information is intact. This coincidence detection implementation adopts a feed-forward 2-layer neural network approach comprising an input layer and an output layer.

simply as a resulting error from sensitivity (true positive rate) which is given as

$$e = 1 - \left(\frac{e_{TP}}{e_{TP} + e_{FN}} \right), \quad (18)$$

where, for τ_s Prediction, the spike errors $e_{TP} = t_d - t_i$ and $e_{FN} = t_i - t_d$. Thus, from (18) the total spike error becomes

$$e = \frac{1}{MK} \sum_M \sum_K \frac{1}{K_+} \sum_{K_+} 1 - \left(\frac{e_{TP}}{e_{TP} + e_{FN}} \right). \quad (19)$$

4.4. Face Classification Using Coincidence Detection. In order to apply coincidence detection as a classifier, the CD neurons are used as output neurons in a 2-layer feed-forward neural network. Using local ensemble strategy for face recognition employed in [29, 30], each CD neuron is attached to each local patch. Thus the number of CD neurons in the classifier network would be equivalent to total number of local patches M . The number of inputs neuron however depends on the dimension, N of the local patch. Since this coincidence detection would evaluate the synchronization between a gallery and a probe input, each CD neuron would have presynaptic neurons and connections of $2N$. The detailed network connections and elements comprising single CD neuron as output neuron are shown in Figure 6.

The output spike train for each local patch δ_m from the CD neuron will then be fed to a summation stage where the outputs of all CD neurons in the network will then be evaluated to produce vectors called Non-Coincidence Factor (NCF), d_m for each local patch. This NCF describes degree of coincidence between an input pair where smaller values of d_m would indicate higher coincidence between the inputs thus higher matching probability and vice versa. Different spike codings can be used to interpret the output spike trains and,

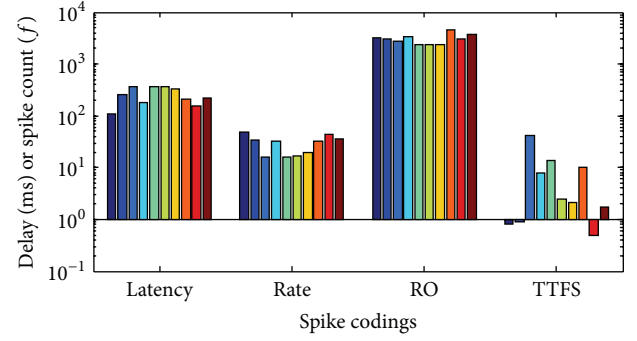


FIGURE 7: Detailed description on the classification model, showing different spike interpretations on classification of a probe patch against 10 gallery patches.

here in this paper, the performance of several spike codings, namely, latency, rate by spike count (conveniently denoted simply as “rate” afterwards), rank order (RO), and time to first spike (TTFS) is investigated. Equations (20) to (23) describe several spike codings used and the associated NCF, d_m as follows.

Latency. Consider the following:

$$d_m = \sum_{l=1}^{\mathcal{L}} (\delta_m(\hat{t}_l) - \delta_m(\hat{t}_{l-1})). \quad (20)$$

Rate (Spike Count). Consider the following:

$$d_m = 2N - \sum_f \delta_m(\hat{t}^f). \quad (21)$$

RO. Consider the following:

$$d_m = \sum_{l=1}^{\mathcal{L}} (\delta_m(\hat{t}_l) - \delta_m(\hat{t}_1)). \quad (22)$$

TTFS. Consider the following:

$$d_m = (\delta_m(\hat{t}_2) - \delta_m(\hat{t}_1)). \quad (23)$$

At the summation stage, the NCF obtained from different spike codings would indicate the gallery image which has the highest probability to be the correct match of the probe. For a more detailed description on the classification model, the delay and spike firing counts of a CD neuron's firings caused by classification of a probe image's patch of dimension, $n = 49$ with 10 lateral gallery images' patches are shown in Figure 7. Note that each bar for each spike coding case represents a gallery image patch, and the first gallery in each case is the actual match for the probe. Based on the figure, we can observe that, for latency, RO, and TTFS coding, lower delay in CD neurons' firing signifies higher coincidence and hence higher probability of correct match, while, for

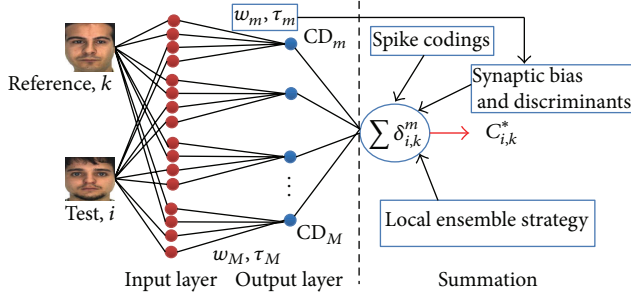


FIGURE 8: Coincidence detection classifier evaluating synchronization of two classes of inputs, namely, reference face k and test face i comprising M CD neurons as output neurons.

spike interpretation by rate coding, the firing delay is totally insignificant but higher rate of spike firings would indicate higher coincidence between the probe and the gallery image. Note also in the figure that a misclassification occurs in TTFS case, where the 9th gallery image patch is found to be having the highest coincidence.

Aside from applying the proper spike codings to interpret the output spike trains, two other processes are also carried out at the summation stage in order to add discriminative influence on the final classification. Firstly, after the spike codings are applied, local ensemble strategies are adopted to locally classify the resulting d_m and then d_m are normalized to find the local confidence vectors $c^m = \log(\arg \min\{d_m\} + 2) / \log(d_m + 2)$. Secondly, these confidence vectors will be weighted using discriminants denoted as φ_m acquired from the learnt synaptic time constants $\tau_{s,m,n}$ computed using

$$\varphi_m = \frac{1}{N} \sum_{n=1}^N \tau_{s,m,n} \quad \text{where } n \in m. \quad (24)$$

Here, the discriminants are then normalized to ensure that φ_m would take the values between $[0 \ 1]$. Consider a probe i needing to be matched to gallery k with each local patch dimension $n = 2$ using a CD classification network with fully trained τ_s , the total weighted confidence c_k^* of probe i as belonging to gallery k can be obtained from (25). For illustration purpose, the whole classification network is shown in Figure 8:

$$c_k^* = \sum_{m=1}^M (\varphi_m c_k^m). \quad (25)$$

5. Experimental Results and Discussions

In this section, we conduct a test to validate and evaluate the accuracy of OSTP approximation and its efficiency. Then we compare the performance of coincidence detection trained by τ_s Prediction against coincidence detection trained by supervised STDP. Subsequently, we investigate the performance of several spike codings used in our proposed coincidence detection. Then using Principal Component Analysis (PCA) and Gabor features, we assess the performance of the proposed CD classifier against several types of classifiers, namely,

k nearest neighbor classifier (k NN), ensembles of k NN classifier (soft k NN) [30], Support Vector Machine (SVM), and ensembles of SVM classifiers (soft SVM) (inspired by [30]).

We adopt Single Sample per Person (SSPP) face recognition (for review, see [31]), where only single image per person is used as gallery. Four publicly available datasets are used for the experiments, namely, AR, JAFFE, FERET, and CK+ datasets. The AR dataset [32] contains frontal images of 76 males and 60 females with several types of variations such as different illumination conditions, expressions, and partial occlusions. Images were taken in two sessions (S1 and S2) with 13 images per session. We use only 8 expression-variant images (neutral, smile, angry, and scream) and 4 partially occluded images (sunglasses and scarf) from both sessions. JAFFE dataset [33] contains 212 expression-variant images from 10 female Japanese subjects. There are 7 types of expressions in this dataset and each subject portrays at least 3 images for each expression. FERET dataset [34] consists of 13,539 facial images corresponding to 1,565 subjects, which are diverse across ethnicity, gender, and age. Two subsets were used, namely, fa and fb following the standard FERET evaluation protocol [34]. Subset fa , containing 1,196 frontal images of 1,196 subjects, was specifically used as gallery, while fb (1,195 expression-variant images) was used as probes. CK+ dataset [35] contains 523 sequences from 123 subjects portraying seven basic expressions (happiness, sadness, surprise, anger, disgust, fear, and contempt). Examples of images from AR, JAFFE, FERET, and CK+ datasets are shown in Figure 9.

As standard preprocessing step, all images used are aligned and resized to 84×84 pixels. Histogram equalization is applied on all images except for images with scarves and sunglasses in AR dataset. This is due to too much irregularity caused by the histogram equalization process on the occluded parts of the image (i.e., the scarves and sunglasses), consistent with the suggestion in [30]. Each image is partitioned into 144 square local patches of 7×7 scanning window. This will result into total dimension of 7056 pixels per image and the vector dimension of $N = 49$ per local patch. Hence the number of afferents that connect input neurons pair to CD neuron is equal to 7056. Each afferent is assumed to be representing a pair of neurons connected to inputs at spatial location \mathcal{L} .

5.1. OSTP Performance Analysis. A test is carried out to determine the accuracy and speed of the OSTP approximation by comparing t_{est} with the exact spike firing time t_{exc} obtained from computation of discrete-time SRM in coincidence neuron. Consider that the sampling frequency or discrete intervals σ for discrete-time SRM and OSTP SRM is measured for each 1 ms and $\Delta s_1 = 1$, respectively; the evaluation of discrete-time SRM uses $\sigma_{\text{disc}} = 1$ while OSTP SRM uses $\sigma_{\text{OSTP}} = 100$. The error e for this test is defined as $e = ||t_{\text{est}} - t_{\text{exc}}|$, where $[x]$ denotes the ceiling process. The test is performed on 191000 neurons, having different values of threshold, synaptic time constant, and weights. It is found that the approximation is correct 99.6% of the time and the processing time taken for OSTP is 9.2454 seconds while discrete-time SRM took 498.7757 seconds. This yields

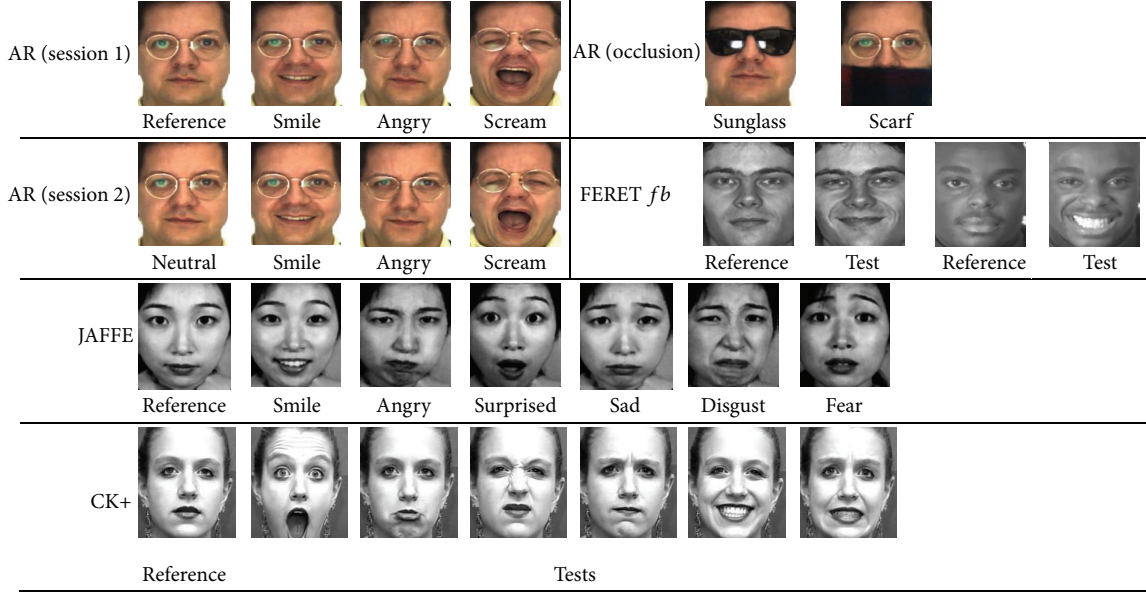


FIGURE 9: Examples of images used in this paper. The variations of probe samples in AR are neutral, smile, angry, scream, sunglass, and scarf, while the variations of probe samples in JAFFE are neutral, smile, angry, surprised, sad, disgust, and fear. FERET probe samples' variations, however, consist of mixtures of several different expressions while CK+ consists of several FACS-coded expressions.

a significant reduction in processing speed by more than 98% of the discrete-time SRM's.

In order to investigate further on the effect of discrete intervals σ_{OSTP} and σ_{disc} on the performance of the spike firing time approximation, the accuracy, Mean Squared Error (MSE), processing speed, and number of floating points operations of OSTP and discrete-time SRM are compared for different values of σ_{OSTP} and σ_{disc} , ranging between 1 and 10000. This test uses $n = 20500$ pairs of input neurons with different combinations of presynaptic inputs, thresholds, synaptic time constants, and weights. The accuracy and MSE of both OSTP and discrete-time SRM is compared with the exact spike timing t_{exc} , where t_{exc} is obtained by discrete-time using $\sigma_{\text{disc}} = 1000$. The approximated spike firing accuracy is calculated based on the following equation while MSE is computed from $\text{MSE} = (1/n)(\sum_{n=1}^n (t_{\text{est}} - t_{\text{exc}})^2)$:

$$\text{approximation accuracy} = \frac{1}{n} \left(\sum_{n=1}^n x_n \right) \times 100\%,$$

$$\text{where } x = \begin{cases} 1, & \text{if } |[t_{\text{est}}] - t_{\text{exc}}| = 0, \\ 0, & \text{if } |[t_{\text{est}}] - t_{\text{exc}}| \neq 0. \end{cases} \quad (26)$$

The number of floating points operations is computed as the total numerical operations from the start to the end of the test. The results on the effect of discrete intervals' size on the performance of OSTP and discrete-time SRM are shown in Figure 10.

According to Figure 10, OSTP produces comparable optimal accuracy and MSE to discrete-time SRM at $\sigma_{\text{OSTP}} = 100$, while consuming minimal processing speed and constant floating points operations. Discrete-time operation on the other hand, even though producing good accuracy and low

MSE, consumes exponentially increasing processing speed and floating points operations with respect to σ_{disc} . From Figure 10(b), for all tested σ , an average of 12.82 seconds is required by OSTP to produce all spikes as opposed to 18.75×10^4 seconds required by discrete-time SRM. As a matter of fact, according to Figure 10(b), at $\sigma_{\text{OSTP}} = \sigma_{\text{disc}} = 100$, the processing speed achieved by OSTP is more than 99% faster than discrete-time SRM while producing comparable accuracy of spike timing as indicated by Figure 10(a). These results highlight the efficiency and performance of the proposed OSTP.

5.2. Face Recognition Performance of τ_s Prediction and Supervised STDP. In order to examine the recognition accuracy of CD classifier trained with Supervised STDP and τ_s Prediction, an experiment is conducted. Following the recommendation by Nordlie et al. [36], a tabular description of experimental setup is given in Table 1.

Each dataset is randomly split into two groups, where each group has half of total number of subjects available. Each split follows 2-fold cross validation method, where each group is interchangeably used as training and then tested once, and after that the average recognition accuracy is taken. This random split is repeated 10 times and the final average accuracy for both training and test along with the standard deviation is recorded in Table 2. For this particular experiment, the spike coding used to interpret the output spikes of CD neuron is latency coding. The Baseline accuracy in Table 2 is obtained from k NN approach.

Based on result presented in Table 2, CD classifier using either Supervised STDP or τ_s Prediction on average delivers better recognition accuracy than the Baseline approach. For the test sets, CD classifier with Supervised STDP delivers

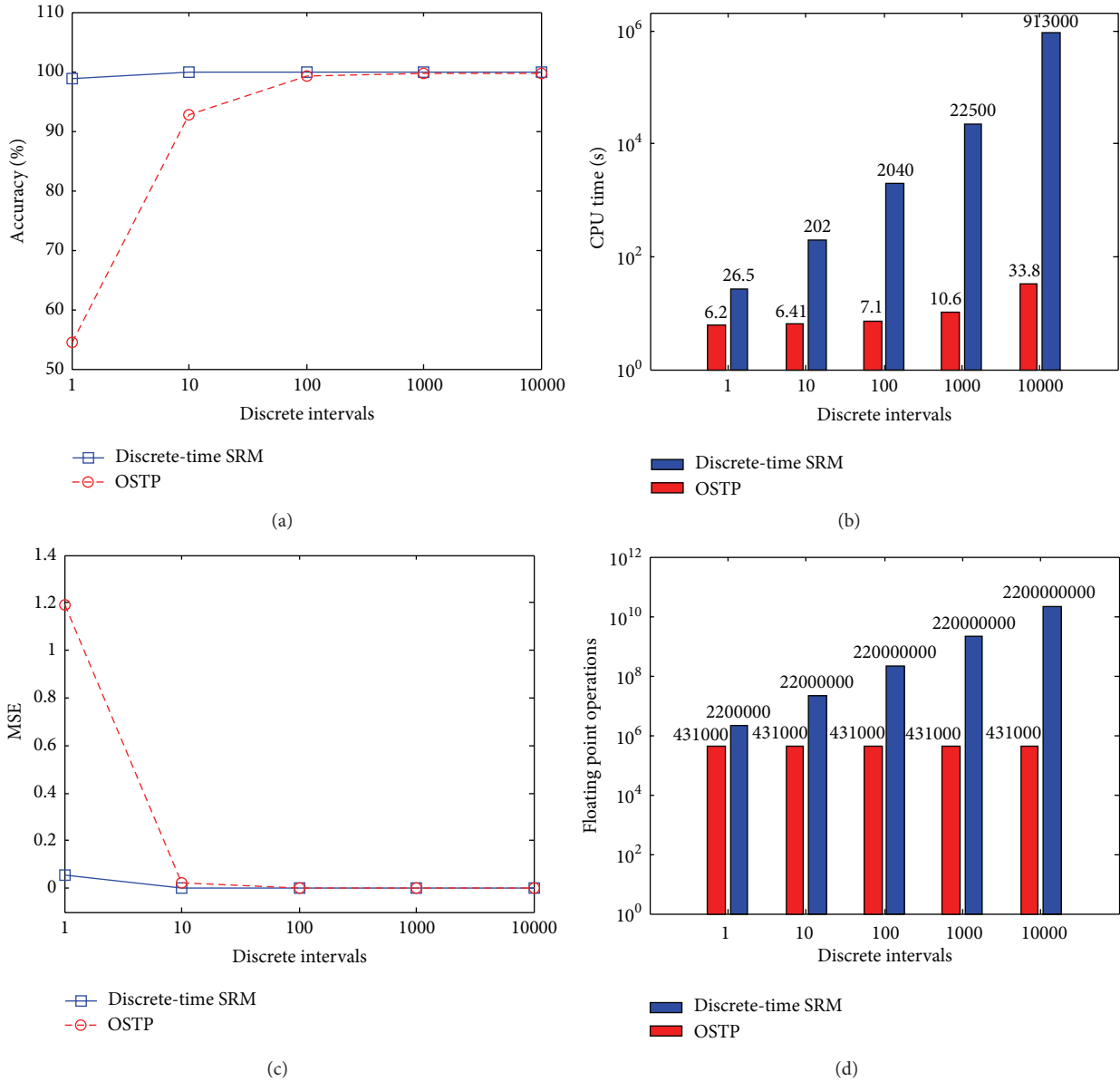


FIGURE 10: Comparisons on the (a) accuracy, (b) processing speed, (c) MSE, and (d) number of floating points operations of OSTP and discrete-time SRM for different values of σ_{OSTP} and σ_{disc} between 1 and 10000.

average recognition accuracy of 95.56%, while τ_s prediction is at 96.31% where both are more than 20% better than Baseline accuracy. In terms of performance between training and test samples, their performances are comparable, signifying that no overfitting occurs during training process. On average, τ_s Prediction performs slightly better than Supervised STDP by just around 1% difference in recognition accuracy.

5.3. *Convergence Analysis.* Since both learning methods are iterative algorithms, their performances with respect to different number of iterations need to be examined. Using AR Scream S1 and Scarf S1, the average recognition accuracy of the training set as the iteration grows for Supervised STDP and τ_s Prediction is shown in Figures 11(a) and

11(b), respectively. Similarly the corresponding spike error e with $\beta = 2$ is also presented in Figure 11(c). According to Figure 11(b), the latency coding converges to minimum recognition error immediately at epoch = 1, while RO and TTFS coding converges at epoch > 10. Special case of convergence is observed for rate coding since it converges to minimum after epoch = 30 and produces lowest error $e_{rate} = 0$. However, the performance of test set for rate coding is not as high, in which we found that test error of $e_{rate} = 0.10$ is obtained (not shown in Figure 11). This indicates an *overfitting* case for rate coding, which also signifies that, in rate coding, large data with large dimension would require a very large number of spikes to reliably distinguish each individual class. Thus it is recommended to use epoch = 1

TABLE 1: Tabular description of experimental setup as suggested in [36].

	Supervised STDP	τ_s Prediction
Model summary		
Neuron model	Zero Order Spike Response Model (SRM ₀) with OSTP	
Synaptic model	α -shaped PSP	
Synaptic function	$\epsilon_{ij}(s) = (s/\tau_{s,ij}) \exp(1 - (s/\tau_{s,ij}))$	
Input connectivity	Feed forward, with each input neuron connected to each image pixels	
Parameters		
Weight, w	Trained, start at constant 4	5
Synaptic time constant, τ_s	3 ms	Trained, start at constant 1 ms
Learning time constant, τ_+ and τ_-	$\tau_+ = \tau_- = 10$ ms	none
Threshold, v	9 mV	5.1 mV
No-spike reset potential, $\eta_{\text{no spike}}$	0 mV	2 mV
Spike reset potential, η_{spike}	0 mV	-2 mV
Learning constant, A_+	0.3	1.0
Learning constant, A_-	0.1	none
OSTP discrete interval σ_{OSTP}	10	10
Positive sample per subject, K_+	All available	All available
Negative sample per subject, K_-	1 (random selection)	None
Input model		
Type	Direct conversion	
Details	Input spike time is equivalent to normalized value of image pixels Each neuron population is attached to each local patch m	

TABLE 2: Result of face recognition accuracy using CD classifier with Supervised STDP and τ_s Prediction.

Datasets	Accuracy (%)				
	Baseline	Supervised STDP		τ_s Prediction	
		Train	Test	Train	Test
AR Neutral S1	82.80	94.00 \pm 0.90	93.40 \pm 1.07	93.10 \pm 0.99	92.80 \pm 0.92
AR Smile S1	100.0	100.0 \pm 0.00	100.0 \pm 0.00	100.0 \pm 0.00	100.0 \pm 0.00
AR Angry S1	93.60	99.10 \pm 0.56	99.20 \pm 0.42	99.10 \pm 0.74	98.90 \pm 0.88
AR Scream S1	74.00	90.90 \pm 0.74	90.70 \pm 0.67	93.10 \pm 1.20	92.90 \pm 1.45
AR Sunglasses S1	56.10	98.20 \pm 1.03	98.20 \pm 1.03	98.30 \pm 0.82	98.40 \pm 0.70
AR Scarf S1	7.80	94.10 \pm 0.99	92.70 \pm 1.34	95.50 \pm 0.85	95.30 \pm 0.67
JAFFE	88.68	94.76 \pm 0.90	93.68 \pm 0.95	96.26 \pm 0.59	94.94 \pm 0.89
<i>fb</i>	89.13	96.83 \pm 0.73	96.62 \pm 0.71	97.27 \pm 0.60	97.26 \pm 0.61
Average	74.01	95.98 \pm 0.73	95.56 \pm 0.77	96.58 \pm 0.73	96.31 \pm 0.76

to avoid overtraining the synaptic time constant τ_s , where the train error $e_{\text{rate}} = 0.08$ and test error $e_{\text{rate}} = 0.08$ are obtained. By comparing Figures 11(a) and 11(b) the convergence to minimum recognition error is achieved faster in τ_s Prediction for all types of spike codings. Similarly, from Figure 11(c), the spike error converges to minimum faster in τ_s Prediction than in Supervised STDP.

To investigate the convergence of both methods further, evolution of output spikes from a CD neuron receiving inputs from 2 populations of neurons sharing similar spatial location as reference and test during Supervised STDP Learning and τ_s Prediction learning process is shown in Figure 12. The 2 populations of neurons are acquired from images belonging to the same subject (matching samples). Based on Figure 12,

both methods start the training by producing only small number of spikes at epoch 0. However, Supervised STDP learning requires more epochs (30 to 35 epochs) before the output spikes stabilize while τ_s Prediction learning only requires 5 to 15 epochs in order to do so. Based on the convergence alone, τ_s Prediction would be favorable since it trains and converges faster than Supervised STDP.

5.4. Discriminants from Synaptic Time Constant. The resulting trained synaptic time constant τ_s can capture the underlying variations embedded within the training faces. We observed that in τ_s Prediction learning the trained synaptic time constants values are lower at synaptic connections attached to face feature with lower importance. This conforms

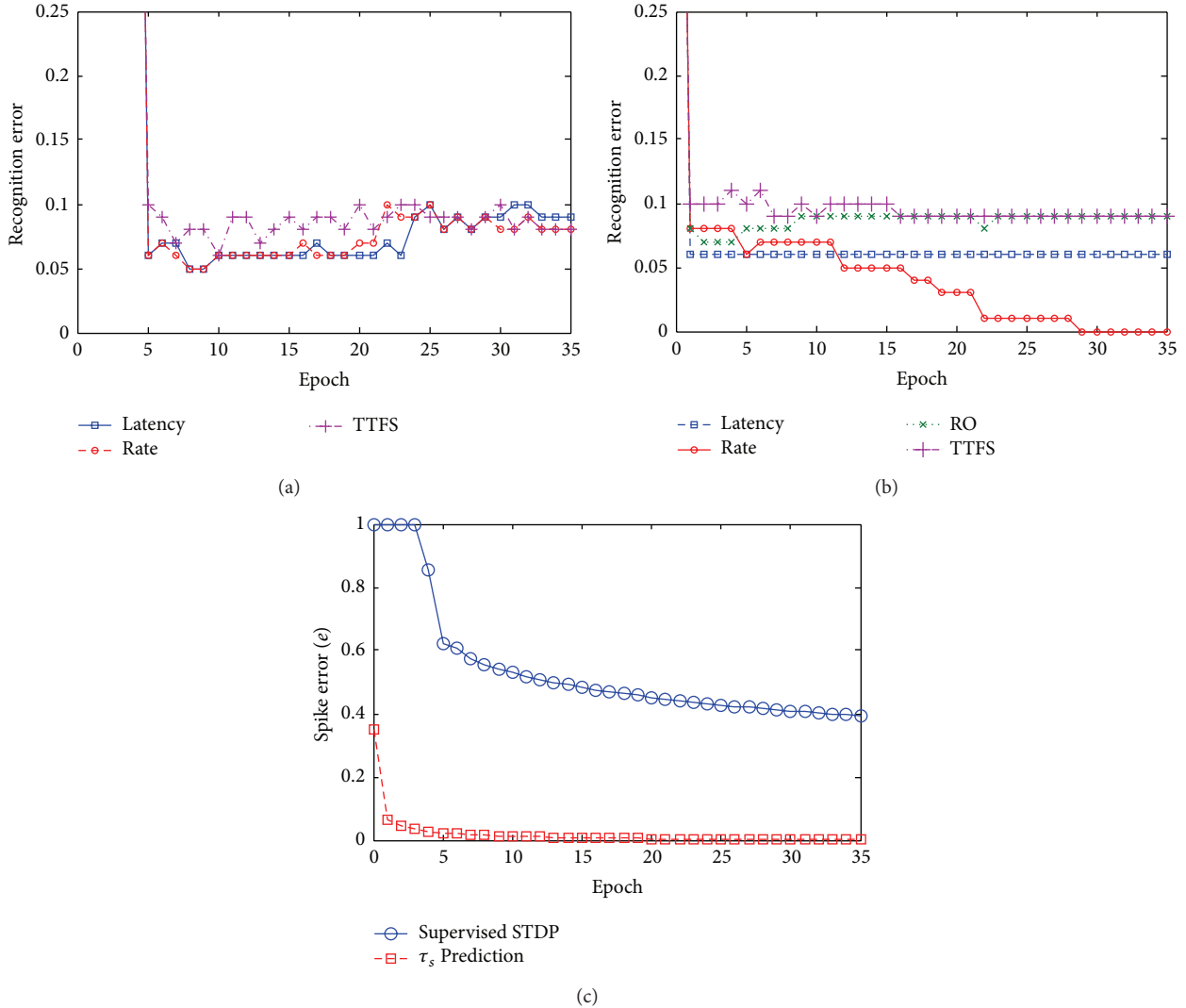


FIGURE 11: Convergence analysis on (a) Supervised STDP and (b) τ_s Prediction using different spike codings (c) shows the comparison on spike error e of Supervised STDP and the τ_s Prediction learning methods as the training iteration grows. The errors are taken as average of recognition error from AR Scream S1 and Scarf S1. The recognition error at $e > 0.25$ in (a) and (b) is not shown for clarity of the graph. For Supervised STDP, recognition error for RO coding e_{RO} is not shown since $e_{RO} = 1$ for all tested epochs.

to the initial objective of enforcing stricter conditions for spike firing on neurons attached to facial regions with high degree of similarity. This would ensure that only highly similar facial regions would cause firing in output neuron. The distribution of fully trained τ_s is shown in Figure 13.

According to Figure 13, facial regions with low discrimination such as mouth in scream set receives higher values of fully trained τ_s which signifies lower importance to final classification. This is used in accordance to feature selection strategy by locally rewarding or penalizing each local NCF obtained from CD classifier based on the computed discriminants φ_m .

5.5. Performance Comparison of Different Spike Codings. From results presented earlier, in terms of recognition accuracy and convergence, one learning method stands out from

the other. τ_s Prediction delivers better recognition accuracy than Supervised STDP and trains faster too. Furthermore, there is a limitation on type of spike coding that could be used by Supervised STDP, where the rank-order coding does not deliver acceptable result. Thus, next analysis on performance of CD classifier using different spike codings to interpret the output spike is based only on CD classifier trained using τ_s Prediction. Using similar experimental settings described in Section 5.2, the recognition accuracy is recorded in Table 3.

According to Table 3, on average, latency coding produces the best test result on test samples with 96.31% accuracy, followed by rate coding with 94.67% accuracy, RO coding with 94.30% accuracy, and TTFS coding with 93.42% accuracy. RO coding particularly works slightly better than latency coding in AR Scarf S1, where it produces 95.90% accuracy as opposed to 95.30% produced by latency coding. On the other hand,

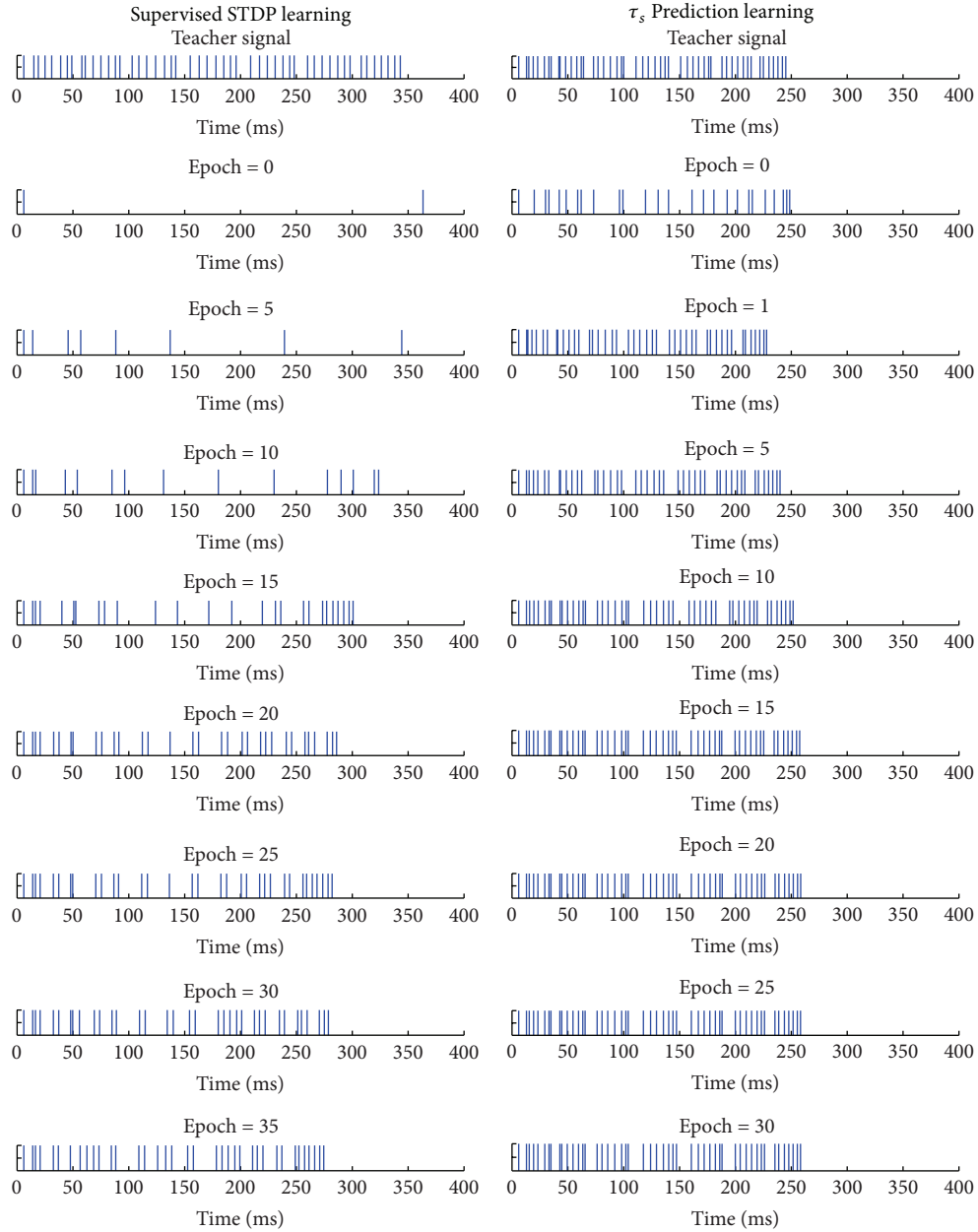


FIGURE 12: Evolution of output spikes from a CD neuron during Supervised STDP Learning and τ_s Prediction learning process. The output spikes are shown as small bar plot indicating the exact output spike time in milliseconds. The input spikes are obtained from identical subject and the output spikes shown also include start and end cues but exclude the imaginary spikes.

considering that TTFS only uses the first output spike from each CD neuron, it delivers quite an impressive result, on average only lacks around 3% accuracy compared to latency coding.

In addition, in order to closely examine the interpretation of each spike coding on output spike distribution for both matching samples and nonmatching samples, 4 images of 2 subjects from AR Scream S1 and Scarf S1 are used. Each pair constitutes to 2 matching samples and 2 nonmatching samples, with each pair of image from the 4 different samples classified by fully trained CD classifier and the input

and output spike patterns are recorded. The input patterns and output spike interpretations of different spike codings are given in Figure 14. The codings are applied to outputs from each local population of input neurons (i.e., 144 local patches).

From Figure 14, the output spikes delays rely heavily on the coincidence of the presynaptic input sequence where matching samples appear to produce lower-delay spikes and vice versa. The rate of output spike firing is also higher in matching sample while slightly lower in nonmatching sample. In the plot, upper face parts are bound to neurons' afferents at

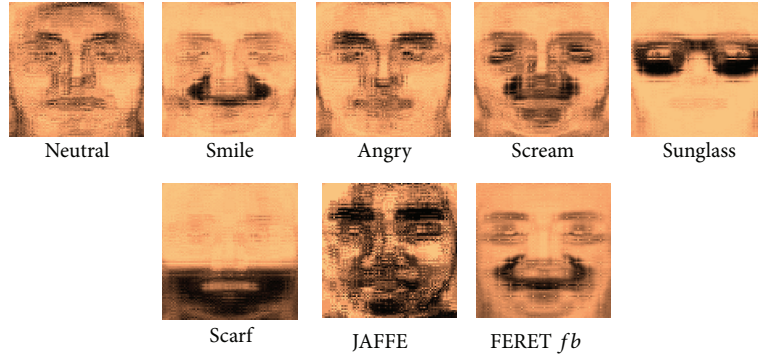


FIGURE 13: Result of learning by τ_s prediction for several face datasets where each pixel in \mathcal{L} location within the images represents the synaptic time constant τ_s of synaptic connection between CD neuron and input neuron attached to the \mathcal{L} location. Darker pixels represent higher τ_s and vice versa. Number of epochs used is 1.

TABLE 3: Result of face recognition accuracy using CD classifier trained by τ_s Prediction with different spike codings.

Datasets	Accuracy (%)							
	Latency		Rate		RO		TTFS	
	Train	Test	Train	Test	Train	Test	Train	Test
AR Neutral S1	93.10	92.80	93.40	92.20	92.60	92.70	91.30	91.10
AR Smile S1	100.0	100.0	100.0	100.0	100.0	100.0	99.40	99.40
AR Angry S1	99.10	98.90	99.50	98.50	97.80	98.00	96.40	95.80
AR Scream S1	93.10	92.90	93.90	92.40	92.40	92.10	84.10	84.20
AR Sunglasses S1	98.30	98.40	97.40	96.70	98.20	98.20	98.30	98.10
AR Scarf S1	95.50	95.30	93.80	90.20	96.00	95.90	92.10	91.40
JAFFE	96.26	94.94	98.12	91.31	95.83	94.35	92.78	91.70
<i>fb</i>	97.27	97.26	95.98	96.05	83.22	83.18	95.70	95.65
Average	96.58	96.31	96.51	94.67	94.51	94.30	93.76	93.42

lower location, while lower face parts are attached to neurons' afferents at higher location. Note that, in both matching and nonmatching samples, the output spike delays and the spike counts are quite the same for upper afferent. However, at lower afferents, significant changes in delays and spike counts can be observed between matching and nonmatching samples. Nonmatching samples produce less spike counts and higher delay than matching sample at lower afferents. Since stricter condition is imposed on upper face part, it is much harder to evoke output spikes when the inputs actually belong to different subjects.

5.6. Results on Face Recognition Using PCA and Gabor Features. For the final experiment, we investigate the performance of our proposed CD classifier against several widely used classifiers. We use two popular feature representation approaches, namely, PCA and Gabor Wavelets, to represent the face. The PCA implementation follows Locally Lateral Subspace (LLS) strategy employed in [29] where the retained PCA features per local patch are 8. Local Gabor features on the other hand were acquired using approach adopted in [37] and the resulting Gabor features per local patches were further downsampled by a factor of 3. Soft k NN follows the

approach detailed in [30] while the soft SVM implementation follows the similar sum aggregation of ensembles of classifiers adopted by soft k NN [30]. SVM implementation uses LibSVM library with RBF kernel [38]. For AR, JAFFE, and FERET datasets, the trained CD classifier acquired in Section 5.2 was used, while, for CK+ dataset, 123 images at the beginning of first sequence are used as gallery while 577 peak images from each sequence are used as probe in training. Then, 4 most expressive images from each sequence resulting into a total of 2290 test images were used as test samples. The result of this experiment is given in Table 4.

According to Table 4, for PCA representation, CD classifier delivers the best result for all tested datasets, while, for Gabor representation, CD classifier gives best recognition accuracy except for CK+ dataset. On average, CD classifier is more than 5% and 11% better than soft k NN and soft SVM, respectively, in PCA representation. For Gabor representation, CD classifier is 2% and 13% better than soft k NN and soft SVM, respectively. The reason why the advantage of using CD classifier is more apparent in PCA representation rather than Gabor is due to the robustness of Gabor features against small spatial perturbations thus increasing the discriminations of facial features, while, in PCA, the noise due to variations

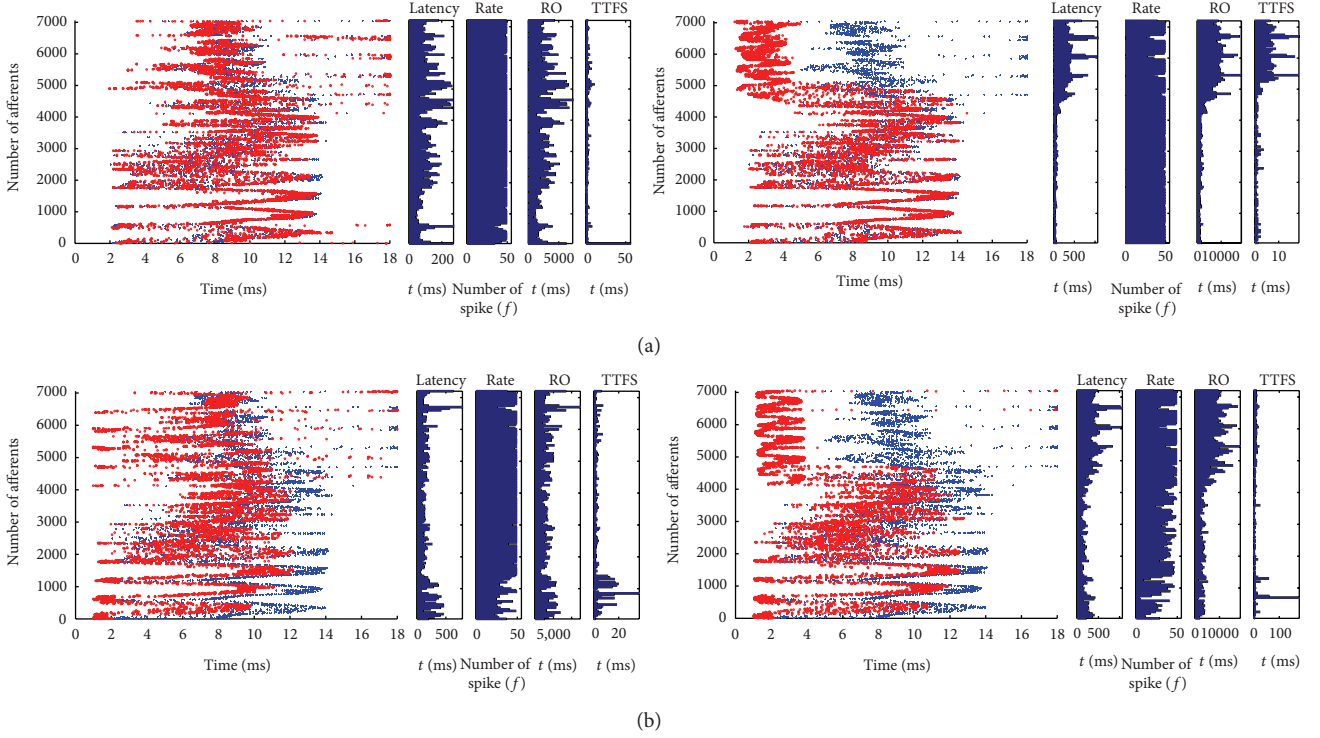


FIGURE 14: Different spike codings applied to output spikes of CD classifier fully trained by τ_s . Prediction with epoch = 1, taking inputs from AR Scream S1 on the left and AR Scarf S1 on the right. Figures in row (a) are plotted from matching face samples, while in bottom row (b) they are from nonmatching face samples. Scatter plots are comprised of spatiotemporal input spike patterns of reference face (blue asterisk) and test face (red circle) from 7056 neurons afferents while bar plots on the right show the CD neurons latency, rate, rank order, and TTFS coding applied. The input spikes are obtained by direct conversion of pixel values to time domain which is then normalized to be between 0 and 18.

TABLE 4: Comparison of face recognition accuracy using CD classifier trained by τ_s . Prediction against several other popular classifiers.

Face representations	Classifier	Accuracy (%)				
		AR	JAFFE	fb	CK+	Average
PCA	k NN	55.55	83.66	83.09	94.32	79.16
	soft k NN	77.09	92.08	92.97	96.86	89.75
	SVM	55.55	83.66	83.09	94.32	79.16
	soft SVM	61.00	88.12	87.11	95.19	82.86
	CD	87.09	94.06	95.73	97.03	93.48
Gabor	k NN	58.73	89.60	87.03	98.21	83.93
	soft k NN	84.00	94.55	96.65	99.26	93.62
	SVM	58.64	76.23	86.95	98.12	79.99
	soft SVM	58.82	87.13	87.28	98.17	82.85
	CD	91.18	95.54	97.32	99.13	95.79

is higher than Gabor features; thus CD classifier's ability to elevate the discriminations of PCA features is more obvious.

5.7. Results on Other Multivariate Datasets. To investigate the viability of the proposed CD classifier approach on multivariate data other than face images, another experiment is conducted using Iris dataset, Breast Cancer Wisconsin

TABLE 5: Comparison of classification accuracy of several multivariate datasets using k NN, SVM and CD classifier.

Classifier	Accuracy (%)			
	Iris	Wisconsin	Statlog	Average
k NN	90.82 \pm 3.5	89.04 \pm 1.2	89.45	89.77
SVM	93.56 \pm 2.3	90.12 \pm 2.6	83.65	89.11
CD (latency)	93.70 \pm 4.3	91.72 \pm 1.0	90.00	91.81
CD (rate)	50.52 \pm 4.7	85.38 \pm 4.8	86.80	73.54
CD (RO)	90.07 \pm 3.4	90.45 \pm 1.5	87.15	89.22
CD (TTFS)	63.26 \pm 6.5	72.44 \pm 6.9	40.65	58.78

(Diagnostic) dataset, and Statlog (Landsat Satellite) dataset [39]. Iris dataset contains 3 classes of 50 vectors each, where each vector has dimension of 4. Wisconsin breast cancer dataset contains 569 vectors belonging to two classes, namely, "malignant" and "benign," where each vector has 32 elements. Statlog dataset contains the multispectral values of pixels in 3×3 neighborhoods in a satellite image. There are 6435 vectors of 36 elements to be classified into 7 classes. Using 10-fold cross validations, 10 splits of training/testing are carried out, except for Statlog dataset since the training and test data are fixed, and the average and standard deviations are recorded in Table 5. CD classifier parameters used are $w = 5$, $\nu = 6$ mV, $A_+ = 1.0$, $\eta_{\text{spike}} = -2$ mV, and $\eta_{\text{no spike}} = 2$ mV.

Training is done by τ_s Prediction learning method where epoch = 1 is used for classification by latency and rate coding, and epoch = 30 is used for classification by RO and TTFS coding.

According to results presented in Table 5, CD classifier with latency coding produces slightly superior result, which is around 2% better than k NN and SVM approach in all datasets, even though the local discrimination is not applicable since the variations within the data are not as generic as the variations found in face image and there is no clear indication on how to locally divide each piece of data into locally lateral vectors. Even if the division was done by assuming single element of the vector as a local vector, we found that no further improvements in classification can be achieved. Furthermore, variations are more random and even though the discrimination can be computed, the learnt discriminants of training data would not be able to faithfully represent the variations in the test set.

Additionally, from this experiment it is found that, for classification of multivariate data, latency coding works best with the average accuracy being 18%, 2%, and 33% better than rate, RO, and TTFS, respectively. The reason behind the inferiority of rate coding is the limitation on maximum encoding capacity, $E_{\max} = 2^N$ of rate of firings due to relatively small number of variables when compared against the number of the samples; that is, for iris dataset only $N = 4$ different variables were available for classification of 120 samples. In contrast, significantly better results achieved by rate coding on Wisconsin and Statlog rather than Iris dataset are due to higher number of variables, which are 32 and 36 variables, respectively, thus increasing the rate-of-firing's maximum encoding capacity. Meanwhile, RO coding is just slightly inferior to latency coding. On the other hand, worst average performance is produced by TTFS coding since it failed to capture the underlying similarities between the probe and the gallery due to only one spike per CD neuron (first spike) being considered in this type of coding.

6. Conclusions and Future Works

In this paper, a classifier based on SNN is proposed, namely, coincidence detection (CD) classifier, where two learning methods used to train CD classifier are also presented. A method of optimizing the discrete-time Spike Response Model (SRM) by predicting the output spike time is also discussed in details. We found that our proposed Output Spike Time Prediction (OSTP) method can produce output spike pattern from input pair identical to discrete SRM but with significantly lower floating operations and much faster processing time, with an average of 12.82 seconds as opposed to 18.75×10^4 seconds in discrete-time SRM for all tested discrete intervals. Besides, we showed that coincidence detection can capture the degree of synchronization between two presynaptic inputs by producing lower-delay output spikes for more synchronized input pairs and vice versa. While CD classifier can produce spike based on the coincidence of inputs, the closeness between the inputs that will trigger the

output spike is explicitly determined by the training process of learning parameter τ_s .

In addition, CD classifier trained with τ_s Prediction delivered comparable performance to Supervised STDP; however it can achieve convergence faster with less number of epochs required. We found that latency coding produced best recognition accuracy at 96.31% but its performance is not too far from other spike codings. Furthermore, the distribution of discriminants derived from the learning parameters revealed the ability of τ_s Prediction learning to capture the underlying variation within the training faces. Further investigation on the performance of CD classifier using PCA and Gabor features showed that our proposed method performs 5% and 11% better than soft k NN and soft SVM, respectively, in PCA representation, while as for Gabor representation it is 2% and 13% better than soft k NN and soft SVM, respectively. Besides, experiment on the feasibility of CD classifier on classifying other multivariate data revealed that CD classifier with latency coding is around 2% better than k NN and SVM classifiers. Additionally, for the tested multivariate data, latency coding delivers the best result which is 18%, 2%, and 33% better than rate, RO, and TTFS, respectively.

As for future work, we will explore the possibility of extending the application of proposed method into object recognition task and also for temporal recognition of faces from video sequences. We would further study how to embed the global information of face image together with local patches information so that the resulting classification is more robust against global variations such as poses, age variation, and illumination.

Appendices

A. Two Presynaptic Spikes Firing at the Same Time

Calculating from (3) to (9)

$$u_m(t) = \eta(t - \hat{t}_i) + \sum_j w_{ij} \sum_f \frac{s}{\tau_{s,ij}} \exp\left(1 - \frac{s}{\tau_{s,ij}}\right). \quad (\text{A.1})$$

Let $\eta(t - \hat{t}_i) = \eta_0 = 0$:

$$\begin{aligned} u_m(t) &= w \left[\frac{t - t_1^f}{\tau_s} \cdot \exp\left(1 - \frac{t - t_1^f}{\tau_s}\right) \right] \\ &\quad + w \left[\frac{t - t_2^f}{\tau_s} \cdot \exp\left(1 - \frac{t - t_2^f}{\tau_s}\right) \right], \\ u_m(t) &= 2w \left[\frac{t - t^f}{\tau_s} \cdot \exp\left(1 - \frac{t - t^f}{\tau_s}\right) \right], \\ u_m &= 2w [s \cdot \exp(1 - s)], \\ \frac{u_m}{2w} &= s \cdot \exp(1 - s), \end{aligned}$$

$$\begin{aligned} \frac{u_m}{2w} &= s \cdot \frac{\exp(1)}{\exp(s)}, \\ \exp(s) \left(\frac{u_m}{2w} \right) &= s \cdot \exp(1), \\ \ln(\exp(s)) + \ln\left(\frac{u_m}{2w}\right) &= \ln(s) + \ln(\exp(1)), \\ s + \ln\left(\frac{u_m}{2w}\right) &= \ln(s) + 1, \\ \ln\left(\frac{u_m}{2w}\right) &= \ln(s) - s + 1, \\ \ln(s) - s + 1 - \ln\left(\frac{u_m}{2w}\right) &= 0. \end{aligned} \tag{A.2}$$

B. Proposed OSTP Equation

Complete calculation of OSTP equation (12) from (10):

$$\begin{aligned} u_m(s) - \eta_0 &= w [s_1 \cdot \exp(1 - s_1)] \\ &+ w [s_2 \cdot \exp(1 - s_2)]. \end{aligned} \tag{B.1}$$

Then, let $a = t_2^f - t_1^f$ and thus $t_2^f = a + t_1^f$. Consequently, s_2 becomes

$$\begin{aligned} s_2 &= \frac{t - t_1^f - a}{\tau_s} - \frac{a}{\tau_s}, \\ s_2 &= \frac{t - t_1^f}{\tau_s} - \frac{a}{\tau_s}, \\ s_2 &= s_1 - \frac{a}{\tau_s}, \\ u - \eta_0 &= w [s_1 \cdot \exp(1 - s_1)] \\ &+ w \left[\left(s_1 - \frac{a}{\tau_s} \right) \cdot \exp\left(1 - \left(s_1 - \frac{a}{\tau_s} \right)\right) \right], \\ \frac{u - \eta_0}{w} &= s_1 \cdot \exp(1 - s_1) + \left(s_1 - \frac{a}{\tau_s} \right) \\ &\cdot \exp\left(1 - \left(s_1 - \frac{a}{\tau_s} \right)\right), \\ \frac{u - \eta_0}{w} &= s_1 \cdot \exp(1 - s_1) + s_1 \cdot \exp\left(1 - s_1 + \frac{a}{\tau_s}\right) \\ &- \frac{a}{\tau_s} \cdot \exp\left(1 - s_1 + \frac{a}{\tau_s}\right), \\ \frac{u - \eta_0}{w} &= s_1 \cdot \exp(1 - s_1) + s_1 \cdot \exp\left(1 - s_1 + \frac{a}{\tau_s}\right) \\ &- \frac{a}{\tau_s} \cdot \exp\left(1 - s_1 + \frac{a}{\tau_s}\right), \end{aligned}$$

$$\begin{aligned} \frac{u - \eta_0}{w} &= s_1 \cdot \exp(1) \cdot \exp(-s_1) + s_1 \cdot \exp(1) \\ &\cdot \exp(-s_1) \cdot \exp\left(\frac{a}{\tau_s}\right), \\ \frac{u - \eta_0}{w} &= s_1 \cdot \exp(-s_1) \cdot \exp(1) \left[1 + \exp\left(\frac{a}{\tau_s}\right) \right] \\ &- \exp(-s_1) \left[\frac{a}{\tau_s} \cdot \exp\left(1 + \frac{a}{\tau_s}\right) \right]. \end{aligned} \tag{B.2}$$

Let $A = \exp(1)[1 + \exp(a/\tau_s)]$ and $B = [(a/\tau_s) \cdot \exp(1 + a/\tau_s)]$:

$$\begin{aligned} \frac{u - \eta_0}{w} &= A \cdot s_1 \cdot \exp(-s_1) - B \cdot \exp(-s_1), \\ \frac{u - \eta_0}{w} &= \exp(-s_1) (A \cdot s_1 - B), \\ \exp(-s_1) (A \cdot s_1 - B) - \frac{u - \eta_0}{w} &= 0. \end{aligned} \tag{B.3}$$

C. Approximating Synaptic Time Constant from SRM Model

Complete calculation from (10) to (15):

$$\begin{aligned} u_m(t) - \eta_0 &= w \left[\frac{t - t_1^f}{\tau_s} \cdot \exp\left(1 - \frac{t - t_1^f}{\tau_s}\right) \right] \\ &+ w \left[\frac{t - t_2^f}{\tau_s} \cdot \exp\left(1 - \frac{t - t_2^f}{\tau_s}\right) \right], \\ \frac{u - \eta_0}{w} &= \frac{1}{\tau_s} \left[(t - t_1^f) \cdot \exp\left(1 - \frac{t - t_1^f}{\tau_s}\right) + (t - t_2^f) \right. \\ &\cdot \exp\left(1 - \frac{t - t_2^f}{\tau_s}\right) \left. \right], \\ \frac{u - \eta_0}{w} &= \frac{1}{\tau_s} \left[(t - t_1^f) \right. \\ &\cdot \exp(1) \exp\left(-\left(t - t_1^f\right) \left(\frac{1}{\tau_s}\right)\right) + (t - t_2^f) \\ &\cdot \exp\left(-\left(t - t_2^f\right) \left(\frac{1}{\tau_s}\right)\right) \left. \right]. \end{aligned} \tag{C.1}$$

Let $X = 1/\tau_s$, and

$$\begin{aligned} \frac{u - \eta_0}{w} &= X \left[(t - t_1^f) \cdot \exp(1) \exp\left(-\left(t - t_1^f\right) (X)\right) \right. \\ &+ \left. (t - t_2^f) \cdot \exp\left(-\left(t - t_2^f\right) (X)\right) \right], \\ X \left[(t - t_1^f) \cdot \exp(1) \exp\left(-\left(t - t_1^f\right) (X)\right) + (t - t_2^f) \right. \\ &\cdot \exp\left(-\left(t - t_2^f\right) (X)\right) \left. \right] - \frac{u - \eta_0}{w} &= 0. \end{aligned} \tag{C.2}$$

D. Proof of Minimum τ_s Required to Evoke a Spike

Given a presynaptic input pair t_1^f and t_2^f , where $t_2^f > t_1^f$, and that the threshold v would make the firing possible, that is, $v \leq \sum w$, then we can let $\tau_s \leq t_2^f - t_1^f$. To prove this, based on (10) assuming that the spike would fire at time $t = t_d$, where $t_d \approx t_2^f$, thus (10) becomes

$$u_m(t_d) - \eta_0 = w \left[\frac{t_d - t_1^f}{\tau_s} \cdot \exp\left(1 - \frac{t_d - t_1^f}{\tau_s}\right) \right] + w \left[\frac{t_d - t_2^f}{\tau_s} \cdot \exp\left(1 - \frac{t_d - t_2^f}{\tau_s}\right) \right]. \quad (\text{D.1})$$

Since $t_d \approx t_2^f$, the second term on the right is almost 0. In order to ensure definitely that a spike would be evoked, $u_m(t_d) - \eta_0$ should be at least equal to w ; thus by setting $u_m(t_d) - \eta_0 = w$

$$w = w \left[\frac{t_d - t_1^f}{\tau_s} \cdot \exp\left(1 - \frac{t_d - t_1^f}{\tau_s}\right) \right], \quad (\text{D.2})$$

$$\left[\frac{t_d - t_1^f}{\tau_s} \cdot \exp\left(1 - \frac{t_d - t_1^f}{\tau_s}\right) \right] = 1.$$

Taking $\tau_s = t_2^f - t_1^f$, then $\tau_s \approx t_d - t_1^f$ so that

$$\left[\frac{\tau_s}{\tau_s} \cdot \exp\left(1 - \frac{\tau_s}{\tau_s}\right) \right] = 1. \quad (\text{D.3})$$

Conflict of Interests

The authors declare that there is no conflict of interests regarding the publication of this paper.

Acknowledgments

The authors would like to thank Dr. Aleix M. Martinez for providing the AR Face Dataset. Some portions of the research in this paper also use Extended Yale Face Database B. The work presented here is cooperatively sponsored by the Ministry of Higher Education Malaysia, under MyRA Incentive Grant Scheme (MIRGS) no. MIRGS13-02-001-0001 and University of Technology MARA, Malaysia.

References

- [1] S. A. Roy and K. D. Alloway, "Coincidence detection or temporal integration? What the neurons in somatosensory cortex are doing," *The Journal of Neuroscience*, vol. 21, no. 7, pp. 2462–2473, 2001.
- [2] J. G. Carlton and P. J. Cullen, "Coincidence detection in phosphoinositide signaling," *Trends in Cell Biology*, vol. 15, no. 10, pp. 540–547, 2005.
- [3] C. J. Tabone and M. Ramaswami, "Is NMDA receptor-coincidence detection required for learning and memory?" *Neuron*, vol. 74, no. 5, pp. 767–769, 2012.
- [4] W. Maass, "Computing with spiking neurons," in *Pulsed Neural Network*, W. Maass and C. M. Bishop, Eds., pp. 55–85, MIT Press, Cambridge, Mass, USA, 1999.
- [5] I. Sporea and A. Grüning, "Supervised learning in multilayer spiking neural networks," *Neural Computation*, vol. 25, no. 2, pp. 473–509, 2013.
- [6] M. Abeles, "Role of the cortical neuron: integrator or coincidence detector?" *Israel Journal of Medical Sciences*, vol. 18, no. 1, pp. 83–92, 1982.
- [7] P. König, A. K. Engel, and W. Singer, "Integrator or coincidence detector? The role of the cortical neuron revisited," *Trends in Neurosciences*, vol. 19, no. 4, pp. 130–137, 1996.
- [8] R. C. DeCharms and A. Zador, "Neural representation and the cortical code," *Annual Review of Neuroscience*, vol. 23, pp. 613–647, 2000.
- [9] W. M. Usrey, J. M. Alonso, and R. C. Reid, "Synaptic interactions between thalamic inputs to simple cells in cat visual cortex," *The Journal of Neuroscience*, vol. 20, no. 14, pp. 5461–5467, 2000.
- [10] Y. Chen, H. Zhang, H. Wang, and L. Yu, "The role of coincidence-detector neurons in the reliability and precision of subthreshold signal detection in noise," *PLoS ONE*, vol. 8, no. 2, Article ID e56822, 2013.
- [11] S. M. Bohte, J. N. Kok, and H. L. Poutre, "SpikeProp: backpropagation for networks of spiking neurons," in *Proceedings of the 8th European Symposium on Artificial Neural Networks (ESANN '00)*, pp. 419–424, Bruges, Belgium, April 2000.
- [12] S. M. Bohte, J. N. Kok, and H. L. Poutre, "Error-backpropagation in temporally encoded networks of spiking neurons," *Neurocomputing*, vol. 48, pp. 17–37, 2002.
- [13] F. Ponulak, *ReSuMe—New Supervised Learning Method for Spiking Neural Networks*, Institute of Control and Information Engineering, Poznan University of Technology, 2005.
- [14] R. V. Florian, "The chronotron: a neuron that learns to fire temporally precise spike patterns," *PLoS ONE*, vol. 7, no. 8, Article ID e40233, 2012.
- [15] Y. Xu, X. Zeng, L. Han, and J. Yang, "A supervised multi-spike learning algorithm based on gradient descent for spiking neural networks," *Neural Networks*, vol. 43, pp. 99–113, 2013.
- [16] A. Mohemmed, S. Schliebs, S. Matsuda, and N. Kasabov, "Training spiking neural networks to associate spatio-temporal input-output spike patterns," *Neurocomputing*, vol. 107, pp. 3–10, 2013.
- [17] J.-P. Pfister, D. Barber, and W. Gerstner, "Optimal hebbian learning: a probabilistic point of view," in *Artificial Neural Networks and Neural Information Processing—ICANN/ICONIP 2003*, vol. 2714 of *Lecture Notes in Computer Science*, pp. 92–98, Springer, Berlin, Germany, 2003.
- [18] J.-P. Pfister, T. Toyozumi, D. Barber, and W. Gerstner, "Optimal spike-timing-dependent plasticity for precise action potential firing in supervised learning," *Neural Computation*, vol. 18, no. 6, pp. 1318–1348, 2006.
- [19] A. Carnell and D. Richardson, "Linear algebra for time series of spikes," in *Proceedings of the 13th European Symposium on Artificial Neural Networks*, pp. 363–368, 2005.
- [20] A. Belatreche, L. P. Maguire, M. McGinnity, and Q. X. Wu, "A method for supervised training of spiking neural networks," in *Proceedings of the IEEE Cybernetics Intelligence—Challenges and Advances (CICA '03)*, pp. 39–44, Reading, UK, 2003.
- [21] B. Schrauwen, *Towards applicable spiking neural networks [Doctorate]*, Electronics and Information Systems, Ghent University, Ghent, Belgium, 2008.

- [22] W. Gerstner and W. M. Kistler, *Spiking Neuron Models*, Cambridge University Press, Cambridge, UK, 2002.
- [23] W. Gerstner and W. M. Kistler, "Mathematical formulations of Hebbian learning," *Biological Cybernetics*, vol. 87, no. 5-6, pp. 404–415, 2002.
- [24] L. F. Abbott and S. B. Nelson, "Synaptic plasticity: taming the beast," *Nature Neuroscience*, vol. 3, pp. 1178–1183, 2000.
- [25] S. Song, K. D. Miller, and L. F. Abbott, "Competitive Hebbian learning through spike-timing-dependent synaptic plasticity," *Nature Neuroscience*, vol. 3, no. 9, pp. 919–926, 2000.
- [26] T. Makino, "A discrete-event neural network simulator for general neuron models," *Neural Computing & Applications*, vol. 11, no. 3-4, pp. 210–223, 2003.
- [27] R. Brette, "Exact simulation of integrate-and-fire models with synaptic conductances," *Neural Computation*, vol. 18, no. 8, pp. 2004–2027, 2006.
- [28] I. Sporea and A. Grüning, "Reference time in SpikeProp," in *Proceedings of the International Joint Conference on Neural Network (IJCNN '11)*, pp. 1090–1092, August 2011.
- [29] F. K. Zaman, A. A. Shafie, and Y. M. Mustafah, "Face recognition robust against expressions and partial occlusions," *International Journal of Automation and Computing*. In press, <http://www.ijac.net/EN/abstract/abstract1650.shtml>.
- [30] X. Tan, S. Chen, Z.-H. Zhou, and F. Zhang, "Recognizing partially occluded, expression variant faces from single training image per person with SOM and soft κ -NN ensemble," *IEEE Transactions on Neural Networks*, vol. 16, no. 4, pp. 875–886, 2005.
- [31] X. Tan, S. Chen, Z.-H. Zhou, and F. Zhang, "Face recognition from a single image per person: a survey," *Pattern Recognition*, vol. 39, no. 9, pp. 1725–1745, 2006.
- [32] A. M. Martinez and R. Benavente, "The AR face database," CVC Technical Report 24, Purdue University, 1998.
- [33] M. J. Lyons, M. Kamachi, and J. Gyoba, "Japanese Female Facial Expressions (JAFFE)," Database of Digital Images, 1997.
- [34] P. Jonathon Phillips, H. Moon, S. A. Rizvi, and P. J. Rauss, "The FERET evaluation methodology for face-recognition algorithms," *IEEE Transactions on Pattern Analysis and Machine Intelligence*, vol. 22, no. 10, pp. 1090–1104, 2000.
- [35] P. Lucey, J. F. Cohn, T. Kanade, J. Saragih, Z. Ambadar, and I. Matthews, "The Extended Cohn-Kanade Dataset (CK+): a complete dataset for action unit and emotion-specified expression," in *Proceedings of the IEEE Computer Society Conference on Computer Vision and Pattern Recognition Workshops (CVPRW '10)*, pp. 94–101, June 2010.
- [36] E. Nordlie, M.-O. Gewaltig, and H. E. Plesser, "Towards reproducible descriptions of neuronal network models," *PLoS Computational Biology*, vol. 5, no. 8, Article ID e1000456, 18 pages, 2009.
- [37] Y. Su, S. Shan, X. Chen, and W. Gao, "Hierarchical ensemble of global and local classifiers for face recognition," *IEEE Transactions on Image Processing*, vol. 18, no. 8, pp. 1885–1896, 2009.
- [38] C.-C. Chang and C.-J. Lin, "LIBSVM: a Library for support vector machines," *ACM Transactions on Intelligent Systems and Technology*, vol. 2, no. 3, article 27, 2011.
- [39] K. Bache and M. Lichman, *UCI Machine Learning Repository*, University of California, School of Information and Computer Sciences, Irvine, Calif, USA, 2013.

Research Article

Gravitational Search Algorithm and Selection Approach for Optimal Distribution Network Configuration Based on Daily Photovoltaic and Loading Variation

Koong Gia Ing,¹ H. Mokhlis,^{1,2} H. A. Illias,^{1,2} M. M. Aman,¹ and J. J. Jamian³

¹Department of Electrical Engineering, Faculty of Engineering, University of Malaya, 50603 Kuala Lumpur, Malaysia

²University of Malaya Power Energy Dedicated Advanced Centre (UMPEDAC), Level 4, Wisma R&D UM, Jalan Pantai Baharu, University of Malaya, 59990 Kuala Lumpur, Malaysia

³Faculty of Electrical Engineering, Universiti Teknologi Malaysia, 81310 Johor Bahru, Johor, Malaysia

Correspondence should be addressed to H. Mokhlis; hazli@um.edu.my

Received 13 March 2015; Revised 14 June 2015; Accepted 21 June 2015

Academic Editor: Mengqi Hu

Copyright © 2015 Koong Gia Ing et al. This is an open access article distributed under the Creative Commons Attribution License, which permits unrestricted use, distribution, and reproduction in any medium, provided the original work is properly cited.

Network reconfiguration is an effective approach to reduce the power losses in distribution system. Recent studies have shown that the reconfiguration problem considering load profiles can give a significant improvement on the distribution network performance. This work proposes a novel method to determine the optimal daily configuration based on variable photovoltaic (PV) generation output and the load profile data. A good combination and coordination between these two varying data may give the lowest power loss in the system. Gravitational Search Algorithm (GSA) is applied to determine the optimum tie switches positions for 33-Bus distribution system. GSA based proposed method is also compared with Evolutionary Programming (EP) to examine the effectiveness of GSA algorithm. Obtained results show that the proposed optimal daily configuration method is able to improve the distribution network performance in term of its power loss reduction, number of switching minimization and voltage profile improvement.

1. Introduction

Over the last few decades, the power loss of distribution system has raised attention of researchers to increase the efficiency of the existing network. Different researchers have proposed different approaches for minimization of power system losses [1]. One of the common approaches is through network reconfiguration.

Network reconfiguration is defined as altering the topological structures of the distribution feeders, by changing the position of tie and sectionalizing switches; however, under normal operation, medium voltage distribution networks operate in radial manner [2, 3]. During normal condition, network reconfiguration is used to improve the power quality, maintain the voltage stability, and reduce power loss, while for fault condition it is used for service restoration. Once the source of fault is removed by opening all the switches surrounding the affected portions, the service can be restored within a very short time.

In the past, various algorithms have been proposed for network reconfiguration. Merlin and Back were the pioneers in proposing network reconfiguration as a tool for power loss reduction [4] in 1975. The network reconfiguration problem was solved by closing all tie switches in the system (resulting in mesh network); then the switches are successively opened, one at a time until a new radial network with minimum power losses is obtained. Later on, Shirmohammadi and Hong improved the Merlin method by avoiding the approximation made in [4]. Shirmohammadi theorem starts by closing all tie switches which are then opened by another based on optimum power flow results [5]. This method was also found efficient in terms of computation time as compared to Merlin method. Reference [2] introduced the “feeder exchange approach” and calculated the loss reduction due to load transfer between two feeders. A year later, Baran and Wu improved the branch exchange method [2] by proposing two approximated power flow equations and solved the problem of loss minimization and loss reduction as an integer

programming problem [6]. In the same year, Lin and Chin [7] have considered service restoration, in addition to loss minimization in solving network reconfiguration problem. Zhu et al. performed the network reconfiguration based on modified heuristic solution and experience system operation rules [8]. In a latest research, Mohd Zin et al. in [9] have used the heuristic search algorithm to find the minimum power losses as an objective function, introduced by the author in [6]. The update principle of heuristic search is made by finding the branch having minimal current, till the optimum solution is obtained.

Most of the methods discussed above require exhaustive search mechanism by considering all possible solutions from a predetermined set and subsequently pick the best one. However, such methods are considered as nonefficient in terms of computation time and space requirement. Intelligent, greedy, and nature observed heuristic techniques have also been proposed in the literature and they are commonly known as Artificial Intelligent (AI) methods [10]. Artificial Intelligent methods are a special class of heuristic search methods [10]. Intelligent based optimization methods have also been utilized in finding optimum tie switch combinations in network reconfiguration problem. Authors have used Genetic Algorithms (GA) [11], fuzzy [12–14], neural network [15, 16], fuzzy-GA [17], Particle Swarm Optimization (PSO) [18], Matroid Theory [19], Hybrid Evolutionary algorithm [20], Ant Colony Search (ACS) algorithm [21, 22], Harmony Search Algorithm [23], and Bacterial Foraging Algorithm [24]. Das [12] and Savier and Das [25] have proposed fuzzy based multiobjective approach for loss reduction and considered voltage limit and line limits as well in fuzzy set. Penalty based multiobjective-single-fitness approaches have been utilized in [21], to combine power losses with system constraints including voltage limits and line limit. The multiobjective problem is solved using ACS algorithm.

Besides network reconfiguration, Distributed Generation (DG) such as minihydro, photovoltaic, and wind is installed in distribution system to solve the power loss problem due to voltage drop. However, the placement and size of DG are essential as they have a great impact on the power loss [26]. Many researchers have proposed different methods for optimum DG location and size separately [26–28] or simultaneously [29, 30]. However, all the aforementioned works have considered a constant load and fixed DG output. In practical, load pattern and DG generation output dynamically change with time. Therefore, some studies have also considered a variable load pattern in their researches. For example, a gradual approaching method is proposed in [31] to solve dynamic reconfiguration. In [32], researchers solved the network reconfiguration problem with daily variable load implementation as well. These studies have proven that the network performance was improved when the time-varying load profiles were taken into consideration.

Apart from that, there are few works on network reconfiguration with the presence of DG considering variable load profile. For example, network reconfiguration with the presence of wind and photovoltaic generation for total daily power loss reduction using improved genetic algorithm is proposed in [33]. Network reconfiguration with photovoltaic

generation for power loss reduction considering the DG penetration and three different load levels is presented in [34].

In this work, a novel method is proposed to solve the network reconfiguration problem based on daily PV generation output and variable load profiles. Gravitational Search Algorithm (GSA) proposed in [35] is used in this paper to determine the best daily system configuration. The proposed method can be viewed in two parts. In the first part, hourly optimal configuration considering the PV generation and load profile is carried out using GSA. In the second part, a selective approach is used to determine the best configuration that gives the lowest power loss for the whole day (24 hrs) or optimal daily configuration. The proposed method is implemented on 33-bus distribution system. The proposed method results are also compared with Evolutionary Programming (EP) to show the effectiveness of GSA.

This paper is organized as follows. In Section 2, mathematical model for network reconfiguration is described. The proposed method including application of GSA and selection approach is provided in Section 3. Selection of PV module is presented in Section 4 while load modelling and PV generation are presented in Section 5. In Section 6, analysis of the performance of the proposed method is discussed. Finally, the conclusions are presented in Section 7.

2. Mathematical Model for Distribution Network Reconfiguration Problem

Network reconfiguration is used to minimize the distribution system power loss. The new configuration selected must fulfil the constraints and maintain the radial structure of the distribution system. In this study, the main objective is to gain minimum power loss of the distribution system. Thus, the objective function can be formulated as follows:

$$\text{Min} \left\{ P_{\text{loss}} = \sum_h^T \sum_{f=1}^N |I_f|^2 l_f R_f \right\}, \quad (1)$$

where N is total line in the system. I_f is real active current of line f . R_f is resistance of line f . f is line number. l_f is the topology status of line f ($1 = \text{close}$, $0 = \text{open}$).

T is the total hour considered in the time frame and h is the current time considered. In this work, (1) is used to analyse the power loss for every hour (h) of a day with the load data of hour (h) and PV generation of hour (h).

The power system constraints that are also being considered in the study are as follows.

(a) *Voltage Bus Constraint.* The value of the bus voltage V_{bus} at each node must be within the acceptable limits to maintain the power quality. For example, in this work, the minimum voltage (V_{min}) used is 0.95 p.u. and maximum voltage (V_{max}) is 1.05 p.u.:

$$V_{\text{min}} < V_{\text{bus}} < V_{\text{max}}. \quad (2)$$

(b) *Radial Configuration Constraint.* The radial configuration of the network must be maintained after the reconfiguration process. In order to ensure this requirement, graph theory is used to determine the radially of the network. In this work, a MATLAB function is used to check the radially of a network as follows:

$$TF = \text{graphisspantree}(G), \quad (3)$$

where G is the distribution system. If the network is radial, TF equals 1 (true); else it is 0 (false). A radial distribution system must connect all the buses and it contains no loop. In order to maintain the radial structure of the distribution system, a network with loop form, one of the switches from that loop must be opened to retain the radial structure.

There are several methods for radial power flow analysis such as backward-forward method. However, in this work the proposed method uses Newton-Raphson load flow for power flow analysis to calculate the power loss. This load flow is selected to avoid fussy requirements on radial structure and prevent complicated computation [36]. It can handle the DG in the calculation more effectively as compared to other distribution load flow methods. Furthermore, this method provides high convergence with low storage required which can be easily applied with any metaheuristic optimization method.

The real power of bus f , P_f , reactive power of bus f , Q_f , the differences in real power, ΔP_f , the differences in reactive power, ΔQ_f , rectangular Newton-Raphson, and power loss can be computed as

$$P_f = \sum_{k=1}^N |V_f| |V_k| |Y_{fk}| \cos(\theta_{fk} - \delta_f + \delta_k), \quad (4)$$

$$Q_f = \sum_{k=1}^N |V_f| |V_k| |Y_{fk}| \sin(\theta_{fk} - \delta_f + \delta_k), \quad (5)$$

$$\Delta P_f = P_f^{\text{SP}} - P_f, \quad (6)$$

$$\Delta Q_f = Q_f^{\text{SP}} - Q_f, \quad (7)$$

$$\begin{bmatrix} \Delta P \\ \Delta Q \end{bmatrix} = \begin{bmatrix} \frac{\partial P}{\partial \delta} & \frac{\partial P}{\partial V} \\ \frac{\partial Q}{\partial \delta} & \frac{\partial Q}{\partial V} \end{bmatrix} \begin{bmatrix} \Delta \delta \\ \Delta |V| \end{bmatrix}, \quad (8)$$

$$P_{\text{loss}} = \sum_{f=1}^N A_{fk} (P_f P_k + Q_f Q_k) + B_{fk} (Q_f P_k - P_f Q_k), \quad (9)$$

$$A_{fk} = \frac{R_{fk} \cos(\delta_f - \delta_k)}{V_f V_k}, \quad (10)$$

$$B_{fk} = \frac{R_{fk} \sin(\delta_f - \delta_k)}{V_f V_k}, \quad (11)$$

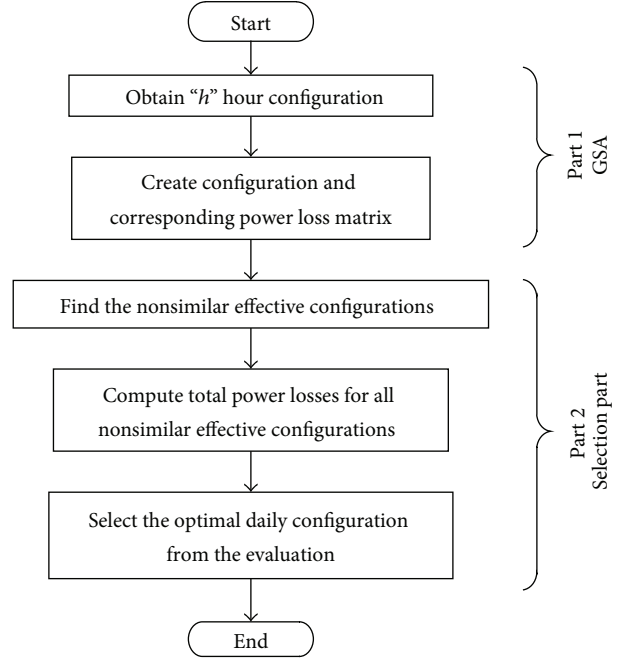


FIGURE 1: Flowchart of the proposed method.

where V_f and V_k are voltage magnitude of bus f and bus k , respectively, Y_{fk} and θ_{fk} are magnitude and angel of Y_{fk} element in the bus admittance matrix, respectively, δ_f and δ_k are voltage angel of bus f and bus k , respectively, P_f^{SP} and Q_f^{SP} are specified real and reactive power at bus f , respectively, P_k and Q_k are real and reactive power of bus k , respectively, and R_{fk} is line resistance between bus f and bus k .

3. Proposed Method

The proposed method for finding the best configuration based on daily PV generation and load profiles is presented in this section. The proposed algorithm consists of two main parts, as shown in Figure 1. In the first part, a day is divided into h hours, where h equals 24 hours in this work. Using GSA and graph theory, optimal configuration is obtained for each hour while the distribution network is maintained to be radial. Hence, a total of h effective configurations are obtained for the network. In part two, the optimal daily configuration is obtained with a selective approach.

Part 1: Finding Effective Configuration Using Gravitational Search Algorithm (GSA). Gravitational Search Algorithm (GSA) is first introduced by Rashedi et al. in [35]. GSA is the newest stochastic search algorithm which is based on Newtonian laws and mass interactions. In this algorithm, the population individuals are referred to as masses and their performances are measured by their position masses. Each mass will have four particulars: its position, its inertial mass, its active gravitational mass, and passive gravitational mass. The position of the mass represented a solution while its gravitational and inertial masses are corresponding to the fitness function. According to Newtonian laws, all these objects will attract each other due to the gravity force. Due to

this force, all these objects will move towards the object with heavier mass. In other words, heavy masses equaled good solutions and they move slower than the lighter masses that equaled bad solutions. In this way, the exploitation step of the algorithm is guaranteed.

The details of the proposed method to reduce power loss are based on the following steps.

Step 1 (input data and parameters). Input data are inserted in the program. This includes bus data, line data, PV output, base MVA, base voltage, predefined voltage bus range, radial configuration constraint, maximum iteration, and accuracy. The parameter needed to be set in GSA is the number of masses (N_{mass}).

Step 2 (generating initial masses). The initial population is determined by selecting random switches to be opened in the distribution network to form the masses. The number of switches to be opened is N_{opened} . The set of switches to be opened is written as follows:

$$\text{Mass}_i = \left[S_1^1, S_2^2, \dots, S_{N_{\text{opened}}}^d \right] \quad \text{for } i = 1, 2, \dots, N_{\text{mass}}, \quad (12)$$

where Mass_i represents the position of i th mass in the d th dimension or d th component in i th mass. S_1^1 , S_2^2 , and $S_{N_{\text{opened}}}^d$ are the switches to be opened in d th dimension. Only the set of switches to be opened that satisfy all the constraints will be generated as the mass. At the end of this step, all the elements in the masses for network reconfiguration are then converted to whole number by rounding the decimal number to the nearest positive number.

Step 3 (evaluate fitness of each mass). In the fitness function, power loss is calculated in the current mass population using Newton-Raphson load flow analysis.

Step 4 (update gravitational constant, best mass, worst mass, and inertia mass of each iteration). In order to control the searching accuracy, the gravitational constant, G , is initialized at the beginning and is reduced with iteration. Hence, gravitational constant G is a function of initial value of gravitational constant, G_0 , and iteration, iter , as follows:

$$G(\text{iter}) = G_0 e^{-\alpha(\text{iter}/\text{max_iter})}, \quad (13)$$

where α is a user specified constant, iter is the current iteration, and max_iter is the total number of iterations.

The active gravitational mass, M_a , passive gravitational mass, M_p , and inertial mass of mass i , M_{ii} , are computed using fitness evaluation. According to Newton's law and law of motion, a heavier mass has higher attractions and move more slowly. Hence, in GSA, a heavier mass is represented as good solution and the pattern of movement is represented by the explorations. The inertia mass, M_i , is updated as follows by assuming all masses are equal:

$$M_{ai} = M_{pi} = M_{ii} = M_i, \\ m_i(\text{iter}) = \frac{\text{fit}_i(\text{iter}) - \text{worst}(\text{iter})}{\text{best}(\text{iter}) - \text{worst}(\text{iter})},$$

$$M_i(\text{iter}) = \frac{m_i(\text{iter})}{\sum_{j=1}^{N_{\text{mass}}} m_j(\text{iter})}, \quad (14)$$

where $\text{fit}_i(\text{iter})$ represents the power loss of the mass i at iteration, iter , and $\text{best}(\text{iter})$ and $\text{worst}(\text{iter})$ represent the strongest and weakest masses with respect to the lowest and highest power losses in current iteration. The mass j of current iteration is represented as $m_j(\text{iter})$. For minimization problem, the $\text{best}(\text{iter})$ and $\text{worst}(\text{iter})$ are defined as

$$\text{best}(\text{iter}) = \min_{j \in \{1, \dots, N_{\text{mass}}\}} \text{fit}_j(\text{iter}), \\ \text{worst}(\text{iter}) = \max_{j \in \{1, \dots, N_{\text{mass}}\}} \text{fit}_j(\text{iter}). \quad (15)$$

Step 5 (calculation of the total force in different directions). The gravitational force, F_{ij} , of mass i due to mass j at current iteration, iter , can be computed as follows:

$$F_{ij}(\text{iter}) = G(\text{iter}) \frac{M_i(\text{iter}) \times M_j(\text{iter})}{R_{ij}(\text{iter}) + \varepsilon} \left(\text{Mass}_j(\text{iter}) - \text{Mass}_i(\text{iter}) \right), \quad (16)$$

where M_i is the inertial mass of the mass i , M_j is the inertial mass of mass j , ε is a small constant, and $R_{ij}(\text{iter})$ is the Euclidian distance between i and j masses specified as follows:

$$R_{ij}(\text{iter}) = \left\| \text{Mass}_i(\text{iter}), \text{Mass}_j(\text{iter}) \right\|_2. \quad (17)$$

Step 6 (calculation of acceleration and velocity). The acceleration of the mass i at current iteration, iter , in d th dimension, and $a_i^d(\text{iter})$ is defined as follows:

$$a_i^d(\text{iter}) = \frac{F_i^d(\text{iter})}{M_{ii}(\text{iter})}, \quad (18)$$

where $F_i^d(\text{iter})$ is the total force that acts on mass i of d th dimension and is calculated as follows:

$$F_i^d(\text{iter}) = \sum_{j \in k_{\text{best}}, j \neq i}^{N_{\text{mass}}} \text{rand}_j F_{ij}^d(\text{iter}). \quad (19)$$

The random number between interval $[0, 1]$, rand_j is introduced in GSA. In order to compromise between exploration and exploitation in this algorithm, the exploration must fade out and exploitation must fade in with lapse of iterations. In other words, all masses apply force to each other in the beginning and only one mass applies force to others in the end of the algorithm. Based on the aforementioned concept, K_{best} , a function of iteration which is the set of first K masses with the lowest power loss and biggest mass, is introduced to this algorithm. K_0 , the initial value of K_{best} , is set at the beginning and decreased with iterations. Thus, K_{best} is decreased linearly with iterations as well. In this way, a smaller value of K_{best} will result in less interaction between the masses by gravitational force. Hence, the movement and computational of power loss

are reduced and lead to convergence [37]. The next velocity of a mass is given as follows:

$$v_i^d(\text{iter} + 1) = \text{rand}_i \times v_i^d(\text{iter}) + a_i^d(\text{iter}). \quad (20)$$

Step 7 (update masses' position). The next position of a mass can be expressed as follows:

$$\text{Mass}_i^d(\text{iter} + 1) = \text{Mass}_i^d(\text{iter}) + v_i^d(\text{iter} + 1). \quad (21)$$

Step 8 (convergence). Steps 3 to 8 are repeated until the stopping criterion is reached.

Step 9 (matrix of h feasible configurations). A matrix consists of h feasible configuration and its power loss is created. Each configuration consists of N_{opened} switch to be opened which depends on the chosen test system. Configuration h is the best configuration with the minimum power loss at hour h . For example, configuration 1 is the best configuration at 0100 and so on as illustrated in

$$\begin{array}{l}
 \text{Configuration 1} \\
 \text{Configuration 2} \\
 \vdots \\
 \text{Configuration } h
 \end{array}
 \begin{bmatrix}
 S_1 & S_2 & S_3 & \cdots & S_{N_{\text{opened}}} \\
 S_{1,1} & S_{1,2} & S_{1,3} & \cdots & S_{1,N_{\text{opened}}} \\
 S_{2,1} & S_{2,2} & S_{2,3} & \cdots & S_{2,N_{\text{opened}}} \\
 \vdots & \vdots & \vdots & \vdots & \vdots \\
 S_{h,1} & S_{h,2} & S_{h,3} & \cdots & S_{h,N_{\text{opened}}}
 \end{bmatrix}
 \begin{array}{l}
 \text{Power loss for } h \text{ hour} \\
 P_{\text{loss}S_1} \\
 P_{\text{loss}S_2} \\
 \vdots \\
 P_{\text{loss}S_h}
 \end{array}
 \quad (22)$$

Part 2: A Selective Approach for Optimal Daily Configuration. In the steps above, N_z number of configurations will be obtained for total time, T . Since most of the PV generations and the load of certain h hour in total time, T , are approximately the same, most of the obtained configurations in (22) are similar. The similar configurations, N_{similar} , are removed from the matrix. Hence, only the nonsimilar effective configurations are left in the matrix, N_{left} ($N_z - N_{\text{similar}} = N_{\text{left}}$).

The first nonsimilar effective configuration in the matrix represents the set switch 1, and so forth, until the last nonsimilar effective configuration, and set switch y . Hence, a matrix consists of all nonsimilar effective configurations and is obtained as illustrated in

$$\begin{array}{l}
 \text{Set Switch 1} \\
 \text{Set Switch 2} \\
 \vdots \\
 \text{Set Switch } y
 \end{array}
 \begin{bmatrix}
 X_1 \\
 X_2 \\
 \vdots \\
 X_y
 \end{bmatrix}
 \begin{array}{l}
 P_{\text{loss}X_1} \\
 P_{\text{loss}X_2} \\
 \vdots \\
 P_{\text{loss}X_y}
 \end{array}
 \quad (23)$$

Each set switch obtained in Part 2 is used to calculate the total power loss for a day using Newton-Raphson load flow analysis. Then, the total daily power losses of the distribution system for all sets of the switch are obtained and the switch set with the minimum total daily power loss is selected as the optimum configuration of the day, as illustrated in

$$\begin{array}{l}
 \text{Set switch} \\
 X_1 \\
 X_2 \\
 \vdots \\
 X_y
 \end{array}
 \begin{array}{l}
 \text{Total daily power loss} \\
 \text{TotDaily}P_{\text{loss}X_1} \\
 \text{TotDaily}P_{\text{loss}X_2} \\
 \vdots \\
 \text{TotDaily}P_{\text{loss}X_y}
 \end{array}
 \quad (24)$$

where optimal daily configuration = $\min(\text{TotDaily}P_{\text{loss}})$.

4. Selection of PV Module

The PV generation in this study is dependent on the solar irradiance and ambient temperature of Malaysian Meteorological Department for year 2008 at Kuantan site. The capacity factor (CF) is calculated using four PV modules from [38] based on the solar irradiance mentioned as above for a day. As shown in Figure 2, module D has the highest CF (0.2223); therefore, module D is selected for this study. The PV output for 10000 units and each h time interval are calculated using (8) to (12). The PV generation is shown in Figure 3:

$$T_{CZ}(h) = T_a + s_{az}(hr) \left(\frac{N_{OT}(\text{module}) - 20}{0.8} \right),$$

$$I_Z(h) = s_{az}(h)$$

$$\cdot [I_{SC}(\text{module}) + K_i(\text{module})(T_{CZ}(h) - 25)],$$

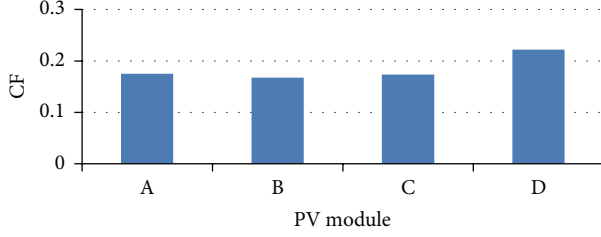


FIGURE 2: CF of the PV module.

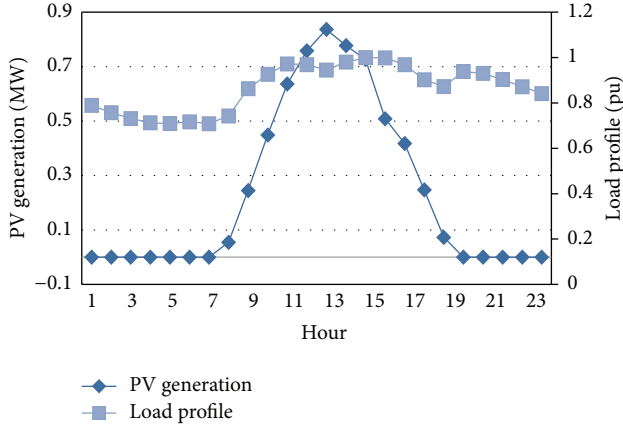


FIGURE 3: PV generation and load profile of a day.

$$V_Z(h) = V_{OC}(\text{module}) - (K_V(\text{module}) \times T_{CZ}(h)),$$

$$FF(\text{module}) = \frac{(V_{MPP}(\text{module}) \times I_{MPP}(\text{module}))}{V_{OC}(\text{module}) \times I_{SC}(\text{module})},$$

$$P_{S_z}(h) = N_{PV} \times FF(\text{module}) \times V_Z(h) \times I_Z(h), \quad (25)$$

where $T_{CZ}(h)$ is cell temperature [$^{\circ}\text{C}$] during h current time, T_a is ambient temperature [$^{\circ}\text{C}$], $K_V(\text{module})$ is voltage temperature coefficient of the PV module [$\text{V}/^{\circ}\text{C}$], $K_i(\text{module})$ is current temperature of the PV module [$\text{A}/^{\circ}\text{C}$], $N_{OT}(\text{module})$ is nominal operating temperature of cell of the PV module [$^{\circ}\text{C}$], $FF(\text{module})$ is fill factor of the PV module, $I_{SC}(\text{module})$ is short circuit current of the PV module [A], $V_{OC}(\text{module})$ is open circuit voltage of the PV module [V], $I_{MPP}(\text{module})$ is current at maximum power point of the PV module [A], $V_{MPP}(\text{module})$ is voltage at maximum power point of the PV module [V], $P_{S_z}(h)$ is output generation of PV module during h current time, and $s_{az}(h)$ is average solar irradiance during h current time.

5. Load Modelling and PV Generation

The load profiles were received from Tenaga Nasional Berhad (TNB) [39] as shown in Figure 3. This study provides hourly peak load per unit of the daily peak load.

6. Analysis of Proposed Method

The test system for this study consists of 12.66 kV 33-bus radial distribution. The single line diagram of the system is shown in Figure 2. The system consists of three DGs, five labelled tie switches, 32 unlabelled sectionalizing switches, and 33 labelled buses. The line between bus 1 and bus 2 is referred to as switch 1, line between bus 2 and bus 3 is referred to as switch 2, and so forth until switch 32. The five tie switches are referred to as switches 33, 34, 35, 36, and 37 as shown in Figure 4. The line and load data are taken from [6]. For analysis purpose, the DGs are assumed to be installed at buses 6, 18, and 22. However, the locations can be changed based on the actual site data or using other placement methods such as in [29]. The parameters of GSA used in the simulation are set to $N_{\text{mass}} = 100$, $\text{max_iter} = 100$, and $G_0 = \text{sum of all active power in the system}$ and $\alpha = 10$. The simulations are carried out on a computer with Intel Duo Core, 3.0 GHz, and 3.0 GB RAM.

The S_{base} equals 100 MVA and all the calculations are performed per unit. In the simulation of the network, four scenarios were considered to analyse the capability of the proposed method. They are as follows.

Scenario 1. The system is without reconfiguration and variation of the load and PV generation are considered.

Scenario 2. The system is with optimal hourly reconfiguration and variation of the load and PV generation are considered.

Scenario 3. The system is with optimal daily configuration obtained from the proposed method.

Scenario 4. The system is with optimal daily configuration obtained by considering 24 demand levels and PV generation as whole.

The results of a matrix consist of h feasible configurations and their power loss obtained in Part 1 of the study is shown in Table 4. The highlighted configurations in Table 4 represent repeated configurations that will be removed in selection approach in Part 2 to obtain the nonsimilar effective configurations matrix in Part 2. The remaining are the non-similar effective configurations. The results of nonsimilar effective configurations matrix in Part 2 of the study are shown in Table 5.

Then, for each set of the switch in Table 5, their total daily power loss is obtained by carrying out Newton-Raphson load flow analysis. The results of the total power loss evaluation for all sets switch obtained in Part 2 are shown in Table 1.

From Table 1, the total daily power loss of set switch 19 which is represented with * is the lowest among the 20 sets switch. Even set switch 16 with the lowest power loss at 1300 does not yield the lowest total daily power losses. Hence, set switch 19 is chosen as the optimal daily configuration which is the best configuration for the day. The real results of the four scenarios are summarised in Table 2. The proposed method is carried out using EP for these four scenarios as well as for comparison as shown in

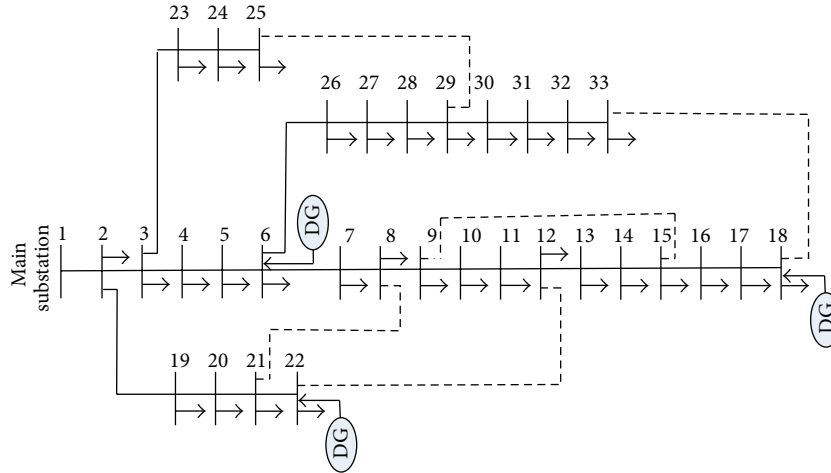


FIGURE 4: 33-bus test system with DG at buses 6, 18, and 22.

TABLE 1: Results of total power loss evaluation for all sets switch obtained in Part 2.

Set switch	1	2	3	4	5	6	7	8	9	10
Total daily power loss (kW)	2724.30	2770.07	2638.54	2752.83	2960.39	2564.08	2219.49	2909.31	2375.65	2149.08
Set switch	11	12	13	14	15	16	17	18	19*	20
Total daily power loss (kW)	2249.01	2303.23	2330.55	3202.01	2088.32	2256.25	2721.87	2256.25	2075.51	2473.59

Table 2. EP is selected for comparison since it is a common and well-established optimization method. The optimal daily configuration obtained in Scenario 4 is 37, 10, 7, 13, and 17 with GSA and 6, 8, 17, 10, and 5 with EP.

From Table 2, the total daily power loss is reduced by 50.36% in Scenario 2, 48.40% in Scenario 3, and 48.02% in Scenario 4 using GSA as optimizing tool and 44.77% in Scenario 2, 41.97% in Scenario 3, and 41.00% in Scenario 4 using EP as optimizing tool compared with Scenario 1 with same load profile and PV generation. The total daily power loss reduction using Scenario 2 is 1.96% (GSA) and 2.80% (EP) more compared with Scenario 3 and 2.34% (GSA) and 3.77% (EP) more compared with Scenario 4. However, no switching is required for Scenarios 3 and 4. For example, 24 times switching are requested in Scenario 2 while no switching is requested in Scenarios 3 and 4. Scenarios 3 and 4 far outweigh Scenario 2 with an acceptable total power loss reduction less than Scenario 2. Apart from that, Scenario 3 gives slightly higher total daily power loss reduction compared with Scenario 4. This is because more constraints need to be considered when 24 demand levels and PV generation are considered as whole. Hence, this limited the solution options.

The DG installation location and number are assumed in this work. Altering DG installation location and number will automatically effect the power loss. The performance of the proposed method is not affected since the algorithm still the same just altering the load data. In other words, more power loss can be reduced with optimal DG installation location and number for a distribution network. An optimal daily

configuration still can be obtained with the proposed method. Similarly for different type of DG with their typical output generation.

The performance of Scenario 2 is reduced when changing the hour slots from 1 hour to 2 hours or 4 hours and so forth. In this case, lower total daily power loss is obtained in Scenario 3 compared to Scenario 2 if the hour slot is increased. The total daily power loss for Scenarios 2 and 3 and optimal daily configuration obtained from Scenario 3 for hour slots of one, two, and four are presented in Table 3. It can be noticed that the total daily power loss in Scenario 3 is less than Scenario 2 for two- and four-hour slots. However, these results are the optimal results since the load demand and PV generation are changing with time. Therefore, the analysis in this work is carried out based on hourly basis.

From this analysis, it clearly shows that the proposed method is effective to determine optimal daily configuration based on PV generation and load profiles for a day. Apart from that, GSA with selection approach gives the best solution compared with EP with selection approach. Figure 5 illustrates the optimal configuration obtained from the proposed method.

The voltage profiles for all scenarios are shown in Figure 6. All the scenarios show the similar shape of the voltage profiles with slight change in the magnitude. The proposed method also improves the overall voltage profiles of the distribution system besides generating lower power loss.

From Figure 6, all bus voltages in Scenario 1 are below the 0.95 p.u. voltage constraint in a day. Although all the bus voltages satisfy the minimum voltage constraint only from

TABLE 2: Comparison of the total daily power loss among the four scenarios.

	Scenario 1 (without reconfiguration)	Scenario 2 (with optimal hourly reconfiguration)	Scenario 3 (with proposed method)	Scenario 4 (with optimal daily configuration of 24 demand levels as whole)
GSA and selection approach				
Total daily power loss (kW)	4022.30	1996.58	2075.51	2090.78
EP and selection approach				
Total daily power loss (kW)	4022.30	2221.52	2334.28	2373.17

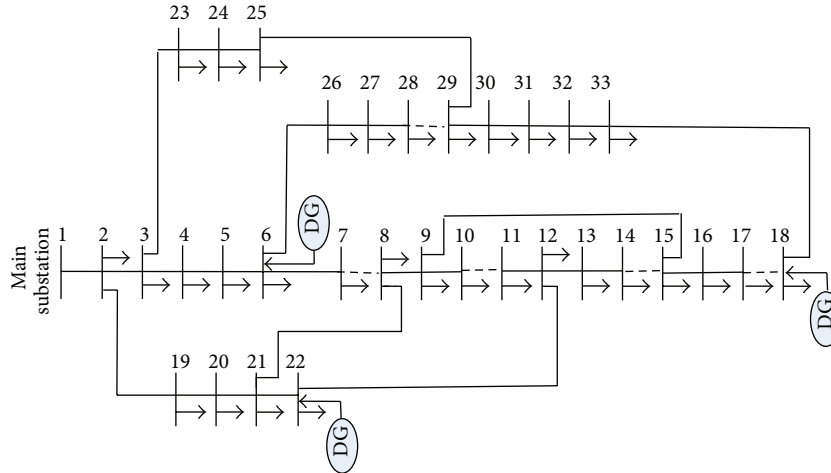


FIGURE 5: Optimal daily configuration.

TABLE 3: Comparison of the total daily power loss among one, two, and four hours' slots.

Hour slots (hr)	Scenario 2	Scenario 3	Optimal daily configuration in Scenario 3
1	1996.58	2075.51	28, 14, 7, 17, 10
2	2204.75	2088.97	31, 6, 37, 34, 10
4	2132.67	2099.09	28, 10, 7, 17, 13

time 0200 to 1800, the overall voltage profiles are improved clearly for all the buses in Scenarios 2, 3, and 4. The voltage profiles at time 1800 for all the buses for Scenarios 1, 2, 3, and 4 are shown in Figure 7.

From Figure 7, it can be seen that, at time 1800, the voltage profiles for Scenarios 1, 2, 3, and 4 are almost the same for all buses. Scenarios 2, 3, and 4 improve the voltage profiles of all the buses and the voltages are within acceptable range especially for buses 28 to 33. This implies that reconfiguration considering PV generation and load profiles yields desired results of minimizing the power loss, reducing the number of switching and improving the voltage profiles. Meanwhile, Figure 8 shows the ability of the GSA with proposed method in finding the optimum configuration at times 0100, 0800, and 1800 which required less than 10 numbers of iterations to reach the optimal point. It is to note that the large the

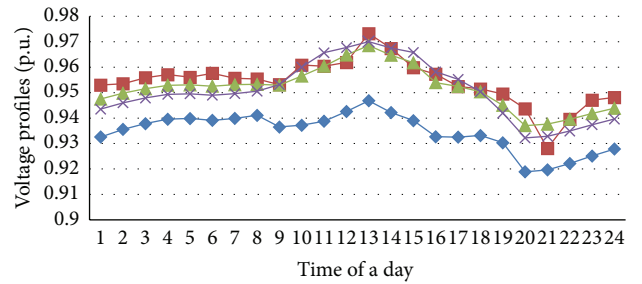


FIGURE 6: Performance of voltage profile for all scenarios of a day.

number of iterations, the longer computing time required as the iteration is counted based on the fixed looping in programming. Thus, in this work, the number of iterations is set to 100.

7. Conclusion

In this work, a novel method to determine the best configuration based on the daily PV generation and load profiles in the distribution network has been successfully proposed. Experimental results indicate that the proposed method is

TABLE 4: Results of matrix consists of h feasible configurations and their power loss obtained in Part 1.

Current time (h)	S_1	S_2	S_3	S_4	S_5	Power losses for h hour (kW)
01	11	7	27	32	14	88.56
02	11	7	28	14	36	80.08
03	28	14	33	9	32	75.39
04	28	9	33	32	14	71.31
05	9	34	37	32	7	70.74
06	32	28	34	7	11	71.65
07	33	36	10	28	34	71.21
08	37	34	9	32	7	70.73
09	37	17	9	14	7	75.63
10	21	31	37	7	13	70.41
11	11	14	30	7	28	70.01
12	8	33	28	13	16	70.22
13	10	7	37	30	14	57.17
14	37	9	30	7	13	62.30
15	37	7	30	10	13	67.28
16	21	34	31	37	7	83.17
17	14	11	7	28	17	86.92
18	10	7	37	14	31	79.19
19	7	11	34	32	28	98.01
20	10	7	14	27	32	126.14
21	10	37	31	14	7	123.80
22	28	14	7	17	10	118.42
23	9	14	28	32	33	108.45
24	7	37	13	32	9	99.78
Total daily power losses for Scenario 2						1996.58

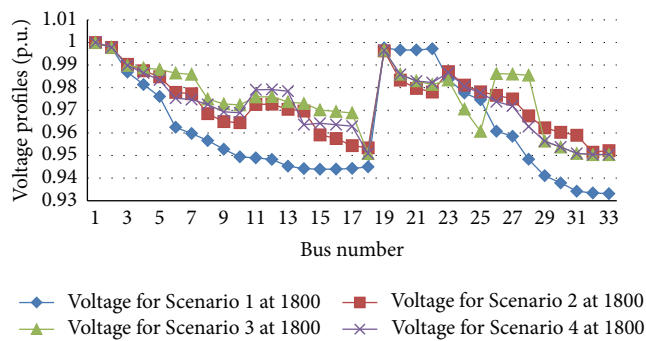


FIGURE 7: Voltage profiles for all buses for all scenarios with load and PV generation at 1800.

simple and effective to minimize total daily power loss with no switching required with the optimal daily configuration obtained. Hence, same method can be applied for a year. It also improves the voltage profiles. A 33-bus distribution system with three photovoltaic DGs, different sets of PV generation, and load profiles are successfully used to

TABLE 5: Results of nonsimilar effective configurations matrix obtained in Part 2.

	S_1	S_2	S_3	S_4	S_5
Set switch 1	11	7	27	32	14
Set switch 2	11	7	28	14	36
Set switch 3	28	9	33	32	14
Set switch 4	32	28	34	7	11
Set switch 5	33	36	10	28	34
Set switch 6	37	34	9	32	7
Set switch 7	37	17	9	14	7
Set switch 8	21	31	37	7	13
Set switch 9	11	14	30	7	28
Set switch 10	8	33	28	13	16
Set switch 11	10	7	37	30	14
Set switch 12	37	9	30	7	13
Set switch 13	37	7	30	10	13
Set switch 14	21	34	31	37	7
Set switch 15	14	11	7	28	17
Set switch 16	10	7	37	14	31
Set switch 17	10	7	14	27	32
Set switch 18	10	37	31	14	7
Set switch 19	28	14	7	17	10
Set switch 20	7	37	13	32	9

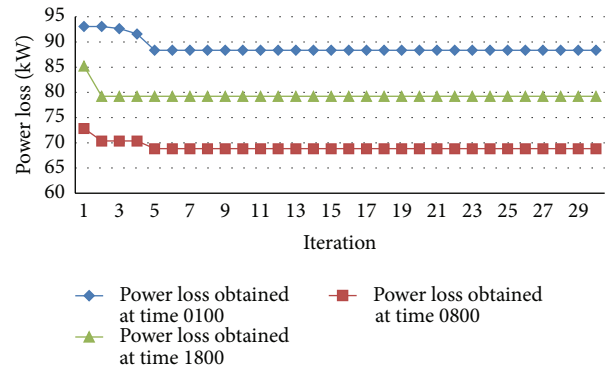


FIGURE 8: Convergence performance of GSA with proposed method at selected time of a day.

demonstrate the effectiveness of the proposed method. A comparison between GSA and EP with selection approach is carried out and the result proven GSA outperforms EP in terms of producing lower total daily power loss.

Conflict of Interests

The authors declare that there is no conflict of interests regarding the publication of this paper.

Acknowledgments

The authors thank the University of Malaya and Malaysian Ministry of Education (MOE) for supporting this work through High Impact Research Grant (HIR-MOHE

D000004-16001) and Universiti Teknologi Malaysia (Q.J130000.2723.00K88).

References

- [1] S. Kalambe and G. Agnihotri, "Loss minimization techniques used in distribution network: bibliographical survey," *Renewable and Sustainable Energy Reviews*, vol. 29, pp. 184–200, 2014.
- [2] S. Civanlar, J. J. Grainger, H. Yin, and S. S. H. Lee, "Distribution feeder reconfiguration for loss reduction," *IEEE Transactions on Power Delivery*, vol. 3, no. 3, pp. 1217–1223, 1988.
- [3] A. González, F. M. Echavarren, L. Rouco, T. Gómez, and J. Cabetas, "Reconfiguration of large-scale distribution networks for planning studies," *International Journal of Electrical Power & Energy Systems*, vol. 37, no. 1, pp. 86–94, 2012.
- [4] A. Merlin and H. Back, "Search for a minimal-loss operating spanning tree configuration in an urban power distribution system," in *Proceedings of the 5th Power System Conference (PSCC '75)*, Cambridge, UK, 1975.
- [5] D. Shirmohammadi and H. W. Hong, "Reconfiguration of electric distribution networks for resistive life losses reduction," *IEEE Transactions on Power Delivery*, vol. 4, no. 2, pp. 1492–1498, 1992.
- [6] M. E. Baran and F. F. Wu, "Network reconfiguration in distribution systems for loss reduction and load balancing," *IEEE Transactions on Power Delivery*, vol. 4, no. 2, pp. 1401–1407, 1989.
- [7] W.-M. Lin and H.-C. Chin, "A new approach for distribution feeder reconfiguration for loss reduction and service restoration," *IEEE Transactions on Power Delivery*, vol. 13, no. 3, pp. 870–875, 1998.
- [8] J. Zhu, X. Xiong, J. Zhang, G. Shen, Q. Xu, and Y. Xue, "A rule based comprehensive approach for reconfiguration of electrical distribution network," *Electric Power Systems Research*, vol. 79, no. 2, pp. 311–315, 2009.
- [9] A. A. Mohd Zin, A. K. Ferdavani, A. B. Khairuddin, and M. M. Naeni, "Reconfiguration of radial electrical distribution network through minimum-current circular-updating-mechanism method," *IEEE Transactions on Power Systems*, vol. 27, no. 2, pp. 968–974, 2012.
- [10] N. Kokash, *An Introduction to Heuristic Algorithms*, Department of Informatics and Telecommunications, 2005.
- [11] J. Z. Zhu, "Optimal reconfiguration of electrical distribution network using the refined genetic algorithm," *Electric Power Systems Research*, vol. 62, no. 1, pp. 37–42, 2002.
- [12] D. Das, "A fuzzy multiobjective approach for network reconfiguration of distribution systems," *IEEE Transactions on Power Delivery*, vol. 21, no. 1, pp. 202–209, 2006.
- [13] Y. Song, G. Wan, A. Johns, and P. Wang, "Distribution network reconfiguration for loss reduction using fuzzy controlled evolutionary programming," *IEEE Proceedings—Generation, Transmission and Distribution*, vol. 144, no. 4, pp. 345–350, 1997.
- [14] J. S. Savier and D. Das, "Impact of network reconfiguration on loss allocation of radial distribution systems," *IEEE Transactions on Power Delivery*, vol. 22, no. 4, pp. 2473–2480, 2007.
- [15] H. Kim, Y. Ko, and K.-H. Jung, "Artificial neural-network based feeder reconfiguration for loss reduction in distribution systems," *IEEE Transactions on Power Delivery*, vol. 8, no. 3, pp. 1356–1366, 1993.
- [16] M. A. Kashem, G. B. Jasmon, A. Mohamed, and M. Moghavvemi, "Artificial neural network approach to network reconfiguration for loss minimization in distribution networks," *International Journal of Electrical Power and Energy Systems*, vol. 20, no. 4, pp. 247–258, 1998.
- [17] K. Prasad, R. Ranjan, N. C. Sahoo, and A. Chaturvedi, "Optimal reconfiguration of radial distribution systems using a fuzzy mutated genetic algorithm," *IEEE Transactions on Power Delivery*, vol. 20, no. 2 I, pp. 1211–1213, 2005.
- [18] M. Assadian, M. M. Farsangi, and H. Nezamabadi-Pour, "GCPSO in cooperation with graph theory to distribution network reconfiguration for energy saving," *Energy Conversion and Management*, vol. 51, no. 3, pp. 418–427, 2010.
- [19] B. Enacheanu, B. Raison, R. Caire, O. Devaux, W. Bienia, and N. HadjSaid, "Radial network reconfiguration using genetic algorithm based on the matroid theory," *IEEE Transactions on Power Systems*, vol. 23, no. 1, pp. 186–195, 2008.
- [20] T. Niknam, E. Azadfarani, and M. Jabbari, "A new hybrid evolutionary algorithm based on new fuzzy adaptive PSO and NM algorithms for distribution feeder reconfiguration," *Energy Conversion and Management*, vol. 54, no. 1, pp. 7–16, 2012.
- [21] C.-T. Su, C.-F. Chang, and J.-P. Chiou, "Distribution network reconfiguration for loss reduction by ant colony search algorithm," *Electric Power Systems Research*, vol. 75, no. 2-3, pp. 190–199, 2005.
- [22] Y.-K. Wu, C.-Y. Lee, L.-C. Liu, and S.-H. Tsai, "Study of reconfiguration for the distribution system with distributed generators," *IEEE Transactions on Power Delivery*, vol. 25, no. 3, pp. 1678–1685, 2010.
- [23] R. Srinivasa Rao, S. V. L. Narasimham, M. Ramalinga Raju, and A. Srinivasa Rao, "Optimal network reconfiguration of large-scale distribution system using harmony search algorithm," *IEEE Transactions on Power Systems*, vol. 26, no. 3, pp. 1080–1088, 2011.
- [24] K. S. Kumar and T. Jayabarathi, "Power system reconfiguration and loss minimization for an distribution systems using bacterial foraging optimization algorithm," *International Journal of Electrical Power & Energy Systems*, vol. 36, no. 1, pp. 13–17, 2012.
- [25] J. S. Savier and D. Das, "Impact of network reconfiguration on loss allocation of radial distribution systems," *IEEE Transactions on Power Delivery*, vol. 22, no. 4, pp. 2473–2480, 2007.
- [26] M. M. Aman, G. B. Jasmon, H. Mokhlis, and A. H. A. Bakar, "Optimal placement and sizing of a DG based on a new power stability index and line losses," *International Journal of Electrical Power & Energy Systems*, vol. 43, no. 1, pp. 1296–1304, 2012.
- [27] Z. Yasin and T. Rahman, *Network Reconfiguration in a Power Distribution System under Fault Condition with the Presence of Distributed Generation*, Universiti Tenaga Nasional, Selangor, Malaysia, 2006.
- [28] J. Olamaei, T. Niknam, and G. Gharehpetian, "Application of particle swarm optimization for distribution feeder reconfiguration considering distributed generators," *Applied Mathematics and Computation*, vol. 201, no. 1-2, pp. 575–586, 2008.
- [29] W. M. Dahalan, H. Mokhlis, A. H. A. Bakar, and J. J. Jamian, "The simultaneous application of optimum network reconfiguration and distributed generation sizing using PSO for power loss reduction," *Przegląd Elektrotechniczny*, vol. 89, no. 4, pp. 137–141, 2013.
- [30] M. M. Aman, G. B. Jasmon, A. H. A. Bakar, and H. Mokhlis, "A new approach for optimum simultaneous multi-DG distributed generation Units placement and sizing based on maximization of system loadability using HPSO (hybrid particle swarm optimization) algorithm," *Energy*, vol. 66, pp. 202–215, 2014.
- [31] Y. HuPing, P. YunYan, and X. Ning, "Gradual approaching method for distribution network dynamic reconfiguration," in

- Proceedings of the Workshop on Power Electronics and Intelligent Transportation System (PEITS '08)*, pp. 257–260, IEEE, Guangzhou, China, August 2008.
- [32] A. E. Milani and M. R. Haghifam, “An evolutionary approach for optimal time interval determination in distribution network reconfiguration under variable load,” *Mathematical and Computer Modelling*, vol. 57, no. 1-2, pp. 68–77, 2013.
- [33] T. Hao, L. Lin, and W. Yanhan, “Research of distribution network reconfiguration with renewable energy power generation unit,” in *Proceedings of the IEEE International Conference on Power System Technology (POWERCON '14)*, pp. 2680–2685, IEEE, Chengdu, China, October 2014.
- [34] A. S. Bouhouras, T. A. Papadopoulos, G. C. Christoforidis, G. K. Papagiannis, and D. P. Labridis, “Loss reduction via network reconfigurations in Distribution Networks with Photovoltaic Units Installed,” in *Proceedings of the 10th International Conference on the European Energy Market (EEM '13)*, pp. 1–8, Stockholm, Sweden, May 2013.
- [35] E. Rashedi, H. Nezamabadi-pour, and S. Saryazdi, “GSA: a gravitational search algorithm,” *Information Sciences*, vol. 179, no. 13, pp. 2232–2248, 2009.
- [36] H. Yang, F. Wen, and L. Wang, “Newton-Raphson on power flow algorithm and Broyden method in the distribution system,” in *Proceedings of the IEEE 2nd International Power and Energy Conference (PECon '08)*, pp. 1613–1618, December 2008.
- [37] B. Shaw, V. Mukherjee, and S. P. Ghoshal, “A novel opposition-based gravitational search algorithm for combined economic and emission dispatch problems of power systems,” *International Journal of Electrical Power and Energy Systems*, vol. 35, no. 1, pp. 21–33, 2012.
- [38] Y. M. Atwa, E. F. El-Saadany, M. M. A. Salama, and R. Seethapathy, “Optimal renewable resources mix for distribution system energy loss minimization,” *IEEE Transactions on Power Systems*, vol. 25, no. 1, pp. 360–370, 2010.
- [39] N. H. B. Jalal, *Operating Code 1: Demand Forecast*, The Malaysian Grid Code Awareness Programme, Kuala Lumpur, Malaysia, 2014.

Research Article

Migrating Birds Optimization for the Seaside Problems at Maritime Container Terminals

Eduardo Lalla-Ruiz, Christopher Expósito-Izquierdo, Jesica de Armas, Belén Melián-Batista, and J. Marcos Moreno-Vega

Department of Computer and Systems Engineering, University of La Laguna, 38271 La Laguna, Spain

Correspondence should be addressed to Eduardo Lalla-Ruiz; elalla@ull.es

Received 13 March 2015; Revised 25 May 2015; Accepted 27 May 2015

Academic Editor: Wei Fang

Copyright © 2015 Eduardo Lalla-Ruiz et al. This is an open access article distributed under the Creative Commons Attribution License, which permits unrestricted use, distribution, and reproduction in any medium, provided the original work is properly cited.

Sea freight transportation involves moving huge amounts of freights among maritime locations widely spaced by means of container vessels. The time required to serve container vessels is the most relevant indicator when assessing the competitiveness of a maritime container terminal. In this paper, two main logistic problems stemming from the transshipment of containers in the seaside of a maritime container terminal are addressed, namely, the Berth Allocation Problem aimed at allocating and scheduling incoming vessels into berthing positions along the quay and the Quay Crane Scheduling Problem, whose objective is to schedule the loading and unloading tasks associated with a container vessel. For solving them, two Migrating Birds Optimization (MBO) approaches are proposed. The MBO is a recently proposed nature-inspired algorithm based on the V-formation flight of migrating birds. In this algorithm, a set of solutions of the problem at hand, called birds, cooperate among themselves during the search process by sharing information within a V-line formation. The computational experiments performed over well-known problem instances reported in the literature show that the performance of our proposed MBO approaches is highly competitive and presents a better performance in terms of running time than the best approximate approach proposed in the literature.

1. Introduction

Maritime container terminals and container vessels are the main components involved in sea freight transportation, where huge amounts of freights are moved among widely spaced locations. Since the international sea freight trade has undergone a relevant growth over the last few decades (United Nations Conference on Trade And Development, <http://www.unctad.org/>), maritime container terminals have to better use and schedule their resources in order to efficiently face the operational and technical requirements of shipping companies. In this regard, as indicated by Nicoletti et al. [1] and Expósito-Izquierdo et al. [2], the time required to serve container vessels, since their arrival until their departure, is the most representative indicator used by the shipping companies when assessing the competitiveness of a given maritime container terminal. Moreover, the faster these tasks are made, the earlier the containers are available for withdrawal by the corresponding companies, and therefore

there will be a better management of the whole terminal (Yeo [3]).

Several logistic problems are relevant in the productivity of the maritime container terminal. One of the most outstanding problems within them is the Berth Allocation Problem (BAP), whose purpose is to allocate and schedule those vessels arriving to port into berthing positions along the quay in order to optimize some objective function. This problem has been extensively studied in the literature over the last years and a multitude of variations has been proposed (Biertwirth and Meisel [4]). One of these variants is the Dynamic Berth Allocation Problem (DBAP), proposed by Cordeau et al. [5]. It considers berth and vessel time windows as well as heterogeneous vessel service times depending on the assigned berth. The other outstanding optimization problem in maritime container terminal is the Quay Crane Scheduling Problem (QCSP), which is aimed at determining the work schedules of the quay cranes allocated to a given container vessel. It is worth mentioning that solving the

DBAP and the QCSP allows the terminal managers to know how to perform the management of the incoming container vessels during a certain planning horizon. This means knowing the berthing position and berthing time of the vessels and how the quay cranes are handled during the transshipment operations. In this regard, their efficient solution prevents traffic bottlenecks and enhances the competitiveness of the whole infrastructure.

Logistic operations, such as those involved in the DBAP and QCSP, require fast and effective solution approaches due to inherent requirements of the context where they appear. In this backdrop, the usage of metaheuristics to find high-quality feasible solutions is advisable. For this reason, in this work we apply and assess a recent nature-inspired metaheuristic based on the V-formation of the migrating birds, called Migrating Birds Optimization (MBO), proposed by Duman et al. [6]. This metaheuristic is a population-based algorithm, where the individuals, called birds, cooperate among themselves during the search process by sharing information about the explored search space. The way they share the information is by considering a V-formation that establishes the relation among birds.

The main goal of this work is to propose and evaluate the use of the MBO technique for solving the main seaside problems at maritime container terminals. With this goal in mind, we have selected two of the most relevant problems in the related literature, DBAP and QCSP. The computational results as well as the comparison with the best approximate algorithms reported in the literature point out a competitive performance of MBO in terms of objective function value and running time. This latter feature makes MBO suitable and competitive to be included in port decision support systems. It is worth highlighting the significance of the running time in these systems, due to the fact that the aforementioned problems may have to be solved frequently (i) because of its direct link with each other and with problems from other parts of the container terminal and (ii) to include possible changes related to terminal resources and (iii) to assist port managers during the negotiations with shipping companies.

The remainder of this paper is structured as follows. Section 2 introduces the DBAP and QCSP. The MBO is presented in Section 3. Afterwards, Section 4 describes the application of MBO to the seaside problems under analysis in this paper: DBAP and QCSP. Section 5 discusses the computational experiments carried out to assess the suitability of MBO. Finally, Section 6 presents the main conclusions extracted from the work and suggests several directions for further research.

2. Seaside Operations

Seaside operations are those related to the transshipment of containers between the container vessels and the maritime container terminal. In this context, three main problems can be identified.

- (i) *Berthing of the Vessels.* Each incoming container vessel has to be assigned to a position along the quay of the container terminal according to its particular characteristics (i.e., length, draft, arrival time, etc.).

- (ii) *Allocation of Quay Cranes.* A subset of the quay cranes in the container terminal must be allocated to each berthed vessel in order to perform its loading and unloading operations.
- (iii) *Scheduling of the Quay Cranes.* The quay cranes allocated to a given container vessel have to be scheduled for performing its transshipment operations in such a way that the stay is the shortest as possible.

As indicated by Bierwirth and Meisel [4], the allocation of quay cranes known as Quay Crane Allocation Problem (QCAP) is tightly related to the BAP due to the fact that the handling times of the vessels depend on the number of quay cranes assigned to them. Consequently, the QCAP is usually jointly considered with the BAP or QCSP. Therefore, in the following, these two relevant logistic problems, namely, the management of berths and the schedule of quay cranes at a terminal when serving container vessels, are addressed.

2.1. Dynamic Berth Allocation Problem. The Dynamic Berth Allocation Problem (DBAP) is an \mathcal{NP} -hard problem (Cordeau et al. [5]) that seeks to identify the berthing position and berthing time of the container vessels arriving to port over a well-defined time horizon.

In the DBAP, we are given a set of incoming container vessels, V , and a set of berths, B . Each vessel, $i \in V$, must be assigned to a berth, $k \in B$. Each vessel has a known time window, $[tv_i, tv'_i]$. Similarly, each berth has its own time window, $[tb_k, tb'_k]$. For each vessel $i \in V$, its service time, s_i^k , depends on the berth $k \in B$, where it is assigned to. That is, the service time of a given vessel may differ from one berth to another. Furthermore, each $i \in V$ has a given service priority, denoted as p_i , according to its contractual agreement with the terminal. It should be noted that the higher this value, the higher the priority of the vessel.

In a more detailed way, the assumptions in the DBAP can be enumerated as follows.

- (a) Each berth $k \in B$ can only handle one vessel at a time.
- (b) The service time of each vessel $i \in V$ is determined by the assigned berth $k \in B$.
- (c) Each vessel $i \in V$ can be served only after its arrival time tv_i .
- (d) Each vessel $i \in V$ has to be served until its departure time tv'_i .
- (e) Each vessel $i \in V$ can only be berthed at berth $k \in B$ after k becomes available at time step tb_k .
- (f) Each vessel $i \in V$ can only be berthed at berth $k \in B$ until k becomes unavailable at time step tb'_k .

In order to present the decision variables, let us define a graph, $G^k = (V^k, A^k) \forall k \in B$, where $V^k = V \cup \{o(k), d(k)\}$ contains a vertex for each vessel as well as the vertices $o(k)$ and $d(k)$, which are the origin and destination nodes for any route in the graph. The set of arcs is defined as $A^k \subseteq V^k \times V^k$, where each one represents the handling time of the vessel. Considering this graph, the decision variables defined in the DBAP are as follows.

- (i) $x_{ij}^k \in \{0, 1\}, \forall k \in B, \forall (i, j) \in A^k, i \neq j$, set to 1 if vessel j is scheduled after vessel i at berth k and 0 otherwise.
- (ii) $T_i^k, \forall k \in B, \forall v \in V$, the berthing time of vessel i at berth k , that is, the time when the vessel berths.
- (iii) $T_{o(k)}^k, \forall k \in B$, starting operation time of berth k , that is, the time when the first vessel berths at the berth.
- (iv) $T_{d(k)}^k, \forall k \in B$, ending operation time of berth k , that is, the time when the last vessel departs at the berth.

The objective function (1) aims to minimize the total (weighted) service time of all the vessels, defined as the time elapsed between their arrival to the port and the completion of their handling. It should be noted that when vessel $i \in V$ is not assigned to berth $k \in B$, the corresponding term in the objective function is zero because $\sum_{j \in V \cup d(k)} x_{ij}^k = 0$ and $T_i^k = t_i$:

$$\min \sum_{i \in V} \sum_{k \in B} p_i \left[T_i^k - t_i + s_i^k \sum_{j \in V \cup d(k)} x_{ij}^k \right]. \quad (1)$$

A comprehensive description of the DBAP is provided by Cordeau et al. [5], Imai et al. [9], and Lalla-Ruiz et al. [10].

For the sake of clarity, we provide an example of a solution of the DBAP in Figure 1. In this figure, an assignment plan is depicted for 6 container vessels and 3 berths. The rectangles represent the vessels. Within each rectangle the service priority, service time, and the time windows associated with each vessel are provided. The time windows of the berths are delimited by the scratched areas. For instance, berth 1 is opened from time step 0 until time step 13. In the figure, vessel 6 has to wait for berthing in their respective assigned berths. In this regard, since its priority is 2, its waiting time will have less impact on the objective function value than delaying, for example, vessel 5.

The mathematical formulation of this problem provided in [11] allows solving those instances within reasonable computational time. However, as indicated in [10] this mathematical model implemented in CPLEX reaches a memory fault status for problem instances where other characteristics are taken into account. Therefore, approximate approaches are required, in the following, we describe the most recent ones, de Oliveira et al. [12] proposed a clustering search with simulated annealing, and the authors evaluate their approach using only the large-size problem instances proposed in [5]. Their approach allows us to reach high-quality solutions in short computational times. Later, Ting et al. [13] developed a Particle Swarm Optimization (PSO) and solve the small- and large-size instances proposed in [5]. Their approach reports the same quality solutions as [12] in terms of objective function value; nevertheless, it requires less computational time. Finally, Lalla-Ruiz and Voß [14] propose a matheuristic based on POPMUSIC (Partial Optimization Metaheuristic Under Special Intensification Conditions). The authors tested their approach over the largest instances proposed in [5] exhibiting a high robustness in terms of the average objective values reported by their approach.

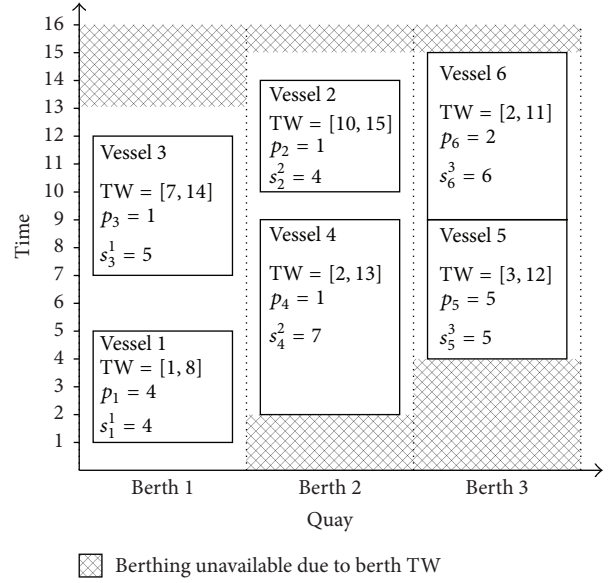


FIGURE 1: Solution example for $|V| = 6$ vessels and $|B| = 3$ berths.

2.2. Quay Crane Scheduling Problem. The Quay Crane Scheduling Problem (QCSP) is stated as determining the finishing times of the tasks performed by the available quay cranes allocated to a container vessel berthed at the terminal. In this environment, a task represents the loading/unloading of a group of containers onto/from a given deck or hold of the container vessel at hand. Alternative definitions of tasks are proposed by Meisel and Bierwirth [15].

Input data for the QCSP consist of a set of tasks $\Omega = \{1, 2, \dots, |\Omega|\}$ (loading or unloading operations associated with a container group) and a set of quay cranes $Q = \{1, 2, \dots, |Q|\}$ with similar technical characteristics. Each $t \in \Omega$ is located in a certain position along the container vessel, l_t , and has a positive handling time, p_t .

The objective of the QCSP is to minimize the service time of the container vessel at hand. That is, its makespan (Kim and Park [16]):

$$\min c_T, \quad (2)$$

where c_t is the finishing time of the task $t \in \Omega$ and T is a dummy task that represents the end of the service.

The QCSP has a set of particular constraints which differentiates it from other well-known scheduling problems found in the scientific literature.

- (a) Each quay crane performs a task without any interruption. This means that once a quay crane starts to (un)load the containers related to a given task, this goes on until all the containers included into the relevant group are (un)loaded.
- (b) Each quay crane $q \in Q$ is only available after its earliest ready time, $r^q \geq 0$.
- (c) Each quay crane $q \in Q$ is initially located on a known position, l_0^q .

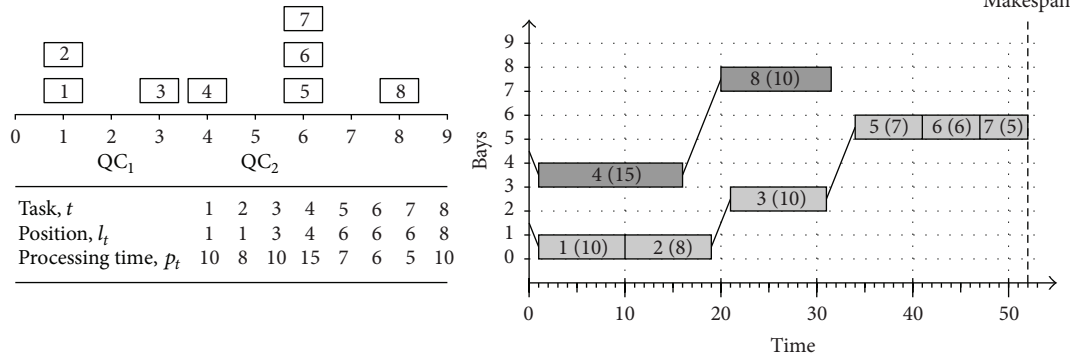


FIGURE 2: Example of a QCSP instance and schedule with 8 tasks and 2 quay cranes.

- (d) Each quay crane $q \in Q$ can travel between two adjacent positions of the container vessel with a travel time, $\hat{t} > 0$.
- (e) Within each position of the container vessel, the relevant tasks are sorted according to their precedence relationships. For instance, unloading tasks must be performed before loading tasks.
- (f) The quay cranes are rail mounted. This means they can only move from left to right along the container vessel and vice versa.
- (g) The quay cranes cannot work in the same position of the vessel simultaneously and they cannot cross each other.
- (h) The quay cranes have to keep a safety distance, $\delta > 0$, between them in order to prevent collisions. This gives rise to that certain tasks cannot be performed simultaneously.

Figure 2 illustrates an example of an instance for the QCSP with 8 tasks and 2 quay cranes. The quay cranes are initially located in the positions $l_0^1 = 2$ and $l_0^2 = 5$ of the container vessel. The right figure depicts a schedule for the instance at hand where the quay cranes are available from the beginning of the service time, $r^q = 0, \forall q \in Q$. Additionally, the quay cranes have to keep a safety distance $\delta = 1$ and they can move between two consecutive positions of the vessel with $\hat{t} = 1$. In this example, tasks 1, 2, 3, 5, 6, and 7 are performed by quay crane 1, whereas tasks 4 and 8 are performed by quay crane 2. As can be seen, the makespan of this schedule is 52 time units.

The QCSP is already known to be \mathcal{NP} -hard (Sammorra et al. [17]). A mathematical formulation for the QCSP is proposed by Legato et al. [18]. Moreover, the QCSP has been suitably dealt in the literature through several papers. It was introduced in the early work by Daganzo [19] and later approximately addressed by Kim and Park [16] and Sammarra et al. [17]. The computational results of these works brought to light the necessity of developing high efficient optimization techniques to tackle the QCSP by means of reasonable computational times. In this regard, an interesting approach to solve the QCSP was put forward by Bierwirth and

Meisel [7]. In their proposal, the authors suggest exploring the search space of unidirectional schedules. A given schedule is termed *unidirectional* if all the quay cranes move with similar direction of movement along their service time. This approach was afterwards deeply exploited by Legato et al. [18] and Expósito-Izquierdo et al. [8]. Lastly, the interested reader is referred to the work by Meisel and Bierwirth [15] to obtain an exhaustive review or the related literature. Unlike most of the previous proposals found in the related literature, the MBO proposed in this work (see Section 3) allows us to reach a high diversification level of the search space during exploration whereas it properly exploits the promising regions in order to find a large number of local optima solutions. This suitable balance between diversification and intensification is mainly due to its population-based structure, which avoids stagnation in low-quality regions of the search space.

3. Migrating Birds Optimization

The Migrating Birds Optimization (MBO) algorithm was initially proposed by Duman et al. [6]. In that work, the authors propose a nature-inspired metaheuristic based on the V-formation flight of migrating birds. This algorithm consists of a set of individuals, where each is associated to a solution and termed as *birds* in MBO. Moreover, the individuals are aligned in a V-formation. Figure 3 shows an illustrative scheme of the V-formation, in which the first individual corresponds to the leader bird in the flock and it is represented by the doubled circle at the top. The remaining circles represent the rest of the flock. The arrows in the figure represent how the information is shared among the individuals.

In MBO, the leader individual attempts to improve itself by generating a number of neighbour solutions. Then, the following individual in the V-formation evaluates a number of its own neighbours and a number of the best discarded neighbour solutions received from the previous individual. In case one of those solutions leads to an improvement with respect to the solution associated with the individual then it is replaced by that solution yielding the maximum improvement. Once all the individuals have been considered, the process is repeated for $iter_{max}$ iterations. Once those

```

(1) Generate  $n_{\text{birds}}$  initial solutions in a random manner and place them on a hypothetical V formation arbitrarily
(2)  $g = 0$ 
(3) while  $g < K$  do
(4)   for ( $l = 0; l < \text{iter}_{\text{max}}; l++$ ) do
(5)     Try to improve the leading solution by generating and evaluating  $\lambda$  neighbours of it
(6)      $g = g + \lambda$ 
(7)     for all (solutions  $s$  in the flock (except leader)) do
(8)       Try to improve the leading solution by generating and evaluating  $\lambda - \delta$ 
         neighbours of it and the  $\delta$  unused best neighbours from the solution in the front.
(9)        $g = g + (\lambda - \delta)$ 
(10)    end for
(11)  end for
(12)  Move the leader solution to the end and forward one of the solutions following it to the leader position
(13) end while
(14) Return best solution in the flock

```

ALGORITHM 1: Migrating Birds Optimization algorithm (Duman et al. [6]).

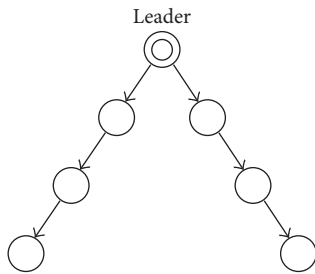


FIGURE 3: Example of the V-formation of the MBO for 7 individuals (birds).

iterations have been reached, the leader individual is moved to the end of one of the lines of the V-formation and one of its direct follower individuals becomes the new leader of the flock. For this new formation, the process restarts for another iter_{max} iterations. The complete MBO process is carried out until a given a stopping criterion is met.

The initial position of the individuals along the V-formation depends on the generation order. That is, the first individual generated will be the leader individual, and therefore the leader bird of the flock, the second and third individuals generated will be its direct followers, and so forth. After generating the initial population, the individuals are organized into a V-formation, as shown in Figure 3.

The input parameters of the MBO algorithm defined by the user are the following:

- n_{birds} : number of individuals termed as birds;
- K : maximum number of neighbour solutions generated by the individuals;
- iter_{max} : number of iterations before changing the leader individuals;
- λ : number of random neighbours generated by each individual;
- δ : number of best discarded solutions to share among individuals.

Algorithm 1 depicts the pseudocode of MBO, as reported by Duman et al. [6]. The first step is to generate n_{birds} individuals (line 1). The number of generated solutions by the population, g , is set to 0 (line 2). Once the population is generated, the MBO search process starts (lines 3–13). During the search process, firstly, the leader individual generates λ random neighbour solutions by means of a neighbourhood structure. In case the best solution generated leads to an improvement in terms of objective function value, the solution associated to the leader is replaced by that neighbour solution (line 5). Secondly, each direct follower individual generates a $\lambda - \delta$ neighbour solutions selected at random (lines 7–10) by means of a neighbourhood structure. Also, each individual receives the best δ discarded solutions from the individual in front of it. If one of the solutions, generated or received, leads to an improvement of the solution associated to the individual, then the improved solution replaces it (line 8). This V-formation is maintained until a prefixed number of iterations, iter_{max} , is reached. Once that, the leader individual becomes the last solution and one of its direct follower individuals becomes the new leader (line 12). Right after, the search process is restarted for other iter_{max} iterations. The MBO search process is executed until a number of neighbour solutions, K , have been generated through the search process (line 3). For a more detailed description of the MBO algorithm, the reader is referred to the work by Duman et al. [6].

4. Migrating Birds Optimization for the Seaside Problems at Maritime Container Terminals

In the following, we apply the Migrating Birds Optimization (MBO) introduced in Section 3 to the DBAP and the QCSP. In both cases, we also evaluate the use of improvement procedures applied to the best solution provided by MBO. The rationale behind this is to (i) assess the capability of MBO for pointing out promising regions of the search space that can be exploited by using a improvement procedure and

(ii) measure the contribution of an improvement method based to the quality of the solutions provided by MBO.

4.1. Migrating Birds Optimization for the Dynamic

Berth Allocation Problem

4.1.1. Solution Representation. In the context of the DBAP, the MBO implementation considers a solution S_{DBAP} as a sequence composed of the vessel identifiers, where each berth is delimited by a 0. The service order of each vessel is determined by its position in the sequence. The solution structure for the example of Figure 1 for 3 berths and 6 vessels is as follows: $S_{DBAP} = \{1, 3, 0, 4, 2, 0, 5, 6\}$.

4.1.2. Neighbourhood Structures. The neighbourhood structures considered in this approach are generated by using the following movements.

- (a) *Reinsertion Movement.* A vessel i is removed from a berth k and reinserted into another berth k' ($\forall k, k' \in B, i \neq i'$) at any of the possible positions. For example, in $S_{DBAP} = \{1, 3, 0, 4, 2, 0, 5, 6\}$ if vessel 1 is removed from its berth, then all these possible reinsertion movements can be performed, namely, $\{3, 0, 1, 4, 2, 0, 5, 6\}$, $\{3, 0, 4, 1, 2, 0, 5, 6\}$, $\{3, 0, 4, 2, 1, 0, 5, 6\}$, $\{3, 0, 4, 2, 0, 1, 5, 6\}$, $\{3, 0, 4, 2, 0, 5, 1, 6\}$, and $\{3, 0, 4, 2, 0, 5, 6, 1\}$.
- (b) *Interchange Movement.* It consists of exchanging a vessel i assigned to berth k with a vessel i' assigned to berth k' ($\forall i, i' \in V, i \neq i', \forall k, k' \in B, k \neq k'$). For example, for the previous solution, $S_{DBAP} = \{1, 3, 0, 4, 2, 0, 5, 6\}$, if we select vessel 1, the possible interchange movements that can be obtained are the following: $\{4, 3, 0, 1, 2, 0, 5, 6\}$, $\{2, 3, 0, 4, 1, 0, 5, 6\}$, $\{5, 3, 0, 4, 2, 0, 1, 6\}$, and $\{6, 3, 0, 4, 2, 0, 5, 1\}$.

The generation of random neighbour solutions by the individuals is based on the reinsertion move. On the other hand, both movements are used in the improvement method.

4.1.3. Improvement Method. As discussed in the relevant section, we also analyse the capability of MBO for pointing out promising regions in the solution search space. In doing so, we applied an improvement method proposed by Lalla-Ruiz et al. [10] over the best solution provided by MBO. This method consist of the following steps: given a solution, its best neighbour solution is obtained by means of the reinsertion moment. Over that best neighbor solution, we generate its neighborhood by means of the interchange movement and return the best neighbor solution. This process is performed until no improvement in terms of the objective function value is achieved.

4.1.4. Initial Population. For generating the initial population, we use a random greedy method (R-G) proposed by Cordeau et al. [5]; that is, given a random vessel permutation, the vessels are assigned one at a time to the best possible berth following that sequence order according to their impact over the objective function value. The use of this method instead

of other proposed initialization procedures reported in the literature such as First-Come First-Served Greedy (FCFS-G) or generating the solution completely at random is based on the fact that, on the one hand, FCFS-G is a deterministic approach, which use will affect the convergence of the algorithm. On the other hand, R-G provides better quality solutions than generating the initial solutions completely at random; this is due to the fact that R-G allocates the vessels within the random sequence according to the impact over the objective function value of the solution being constructed.

4.1.5. Stopping Criterion. The stopping criterion for the overall MBO search process is met when a certain number of K generated solutions by the population are reached. Moreover, as pointed out in the relevant section, for large-size instances, we included an additional stopping criterion based on a maximum number of iterations γ without improvement of the best solution obtained.

4.2. Migrating Birds Optimization for the Quay Crane Scheduling Problem

4.2.1. Solution Representation. The solutions of the QCSP are represented as sequences composed of the available tasks, that is, Ω . A given sequence includes zeros in order to delimit the subsets of tasks performed by the quay cranes. This way, the leftmost quay crane performs those tasks from the beginning of the sequence up to the first zero, the second quay crane performs those tasks from the first zero up to the second zero, and so forth. For instance, a solution for the example presented in Figure 2 with 2 quay cranes and 8 tasks could be as follows: $S_{QCSP} = (1, 2, 3, 5, 6, 7, 0, 4, 8)$. In this case, the leftmost quay crane performs the tasks $(1, 2, 3, 5, 6, 7)$, whereas the other quay crane performs the tasks $(4, 8)$.

4.2.2. Neighbourhood Structures. The neighbourhood structures used by the MBO are based on the following exploring movements.

- (a) *Reinsertion Movement.* A task $t \in \Omega$ currently assigned to a quay crane $q \in Q$ is reassigned, in such a way that t is performed by another quay crane $q' \in Q$ (where $q' \neq q$).
- (b) *Interchange Movement.* Given pair tasks, $t_1, t_2 \in \Omega$, assigned to two different quay cranes, $q \in Q$ and $q' \in Q$ (where $q' \neq q$), the movement exchanges the tasks. This way, t_2 is eventually assigned to q whereas t_1 is assigned to q_2 .

The generation of random neighbour solutions by the individuals is based on the interchange movement.

4.2.3. Local Search. A local search process based on the best improvement strategy is proposed in order to find local optima solutions during the search. This way, given a certain feasible solution of the QCSP, at each step, the set of neighbour solutions found by means of reinsertion movement is generated. The best neighbour solution replaces the current solution until a local optimum is achieved.

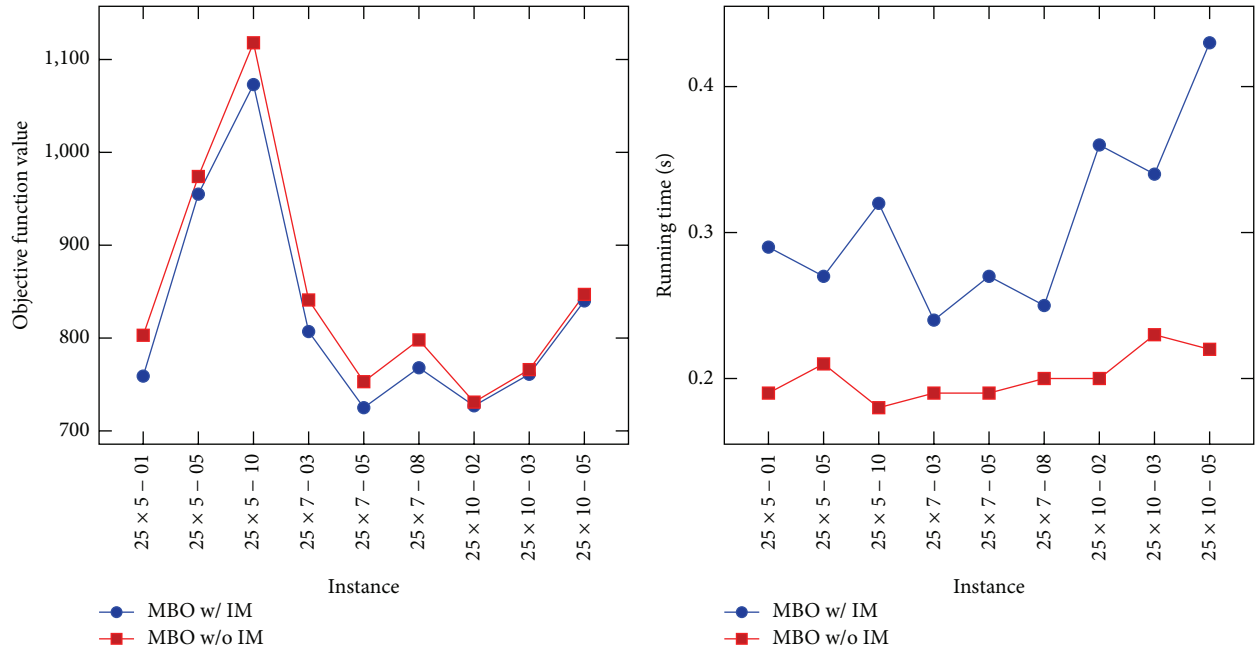


FIGURE 4: Performance of MBO with and without an improvement procedure when solving the DBAP small-size instances.

4.2.4. Initial Population. The solutions included into the initial population have been generated at random. This means that each task is assigned to one of the available quay cranes randomly. It is worth mentioning that the tasks are selected to be assigned from the leftmost up to the rightmost within the container vessel.

4.2.5. Stopping Criterion. The stopping criterion for the overall MBO search process is met when a certain number of K neighbour solutions have been already generated by the individuals.

5. Computational Experiments

This section is devoted to assessing the performance of the Migrating Birds Optimization (MBO) introduced in the previous section. All the reported computational experiments have been conducted on a computer equipped with an Intel Dual Core 3.16 GHz and 4 GB of RAM.

5.1. Computational Experiments for the DBAP. The problem instances used for evaluating the performance of our MBO approach are those provided by Cordeau et al. [5]. According to the authors, their instances were generated by taking into account a statistical analysis of the traffic and berth allocation data at the maritime container terminal of Gioia Tauro (Italy). The instances are grouped into sets of 10 instances, whose sizes range from 25 vessels and 5 berths up to 60 vessels and 13 berths. Moreover, in order to fit the space for this work, for the small- and medium-size problem instances we have selected the 3 hardest solvable instances of each set with regard to the time required to provide

the optimal solution by the implementation of the mathematical formulation (Buhrkal et al. [11]) in CPLEX (<http://www-01.ibm.com/software/commerce/optimization/cplex-optimizer/>) to provide the optimal solution. For the large instance set, we selected a representative set of instances. By taking into account the experiments carried out in this work, we identified the following parameter values for MBO, $n_{\text{birds}} = 31$, $\delta = 3$, $\lambda = 20$, $\text{iter}_{\text{max}} = 3$, and $K = |N|^3$ for the small- and medium-size instances. For the large-size instances, we set $K = |N|^{2.5}$ and an additional stopping criterion of a maximum number of $\gamma = 10$ consecutive iterations without improvement of the best solution obtained.

5.1.1. Improvement Method. As previously indicated in Section 4, an improvement phase (based on that proposed by Lalla-Ruiz et al. [10]) is applied over the best solution provided by MBO. Figures 4, 5, and 6 show the computational performance in terms of objective function value and computational time of MBO with (MBO w/IM) and without (MBO w/o IM) improvement method for the small-, medium-, and large-size instances proposed by Cordeau et al. [5]. As can be checked, the performance exhibited by MBO is similar regardless of size of the instance. Furthermore, the use of an improvement procedure leads to an enhancement of the best-known solution through a small increase of the computational time. This indicates that the use of the improvement to this method enhances the convergence to the best solution within our complete approach proposed in this work.

At the light of this analysis, in the following results we report the computational results provided by the joint use of MBO with the improvement method.

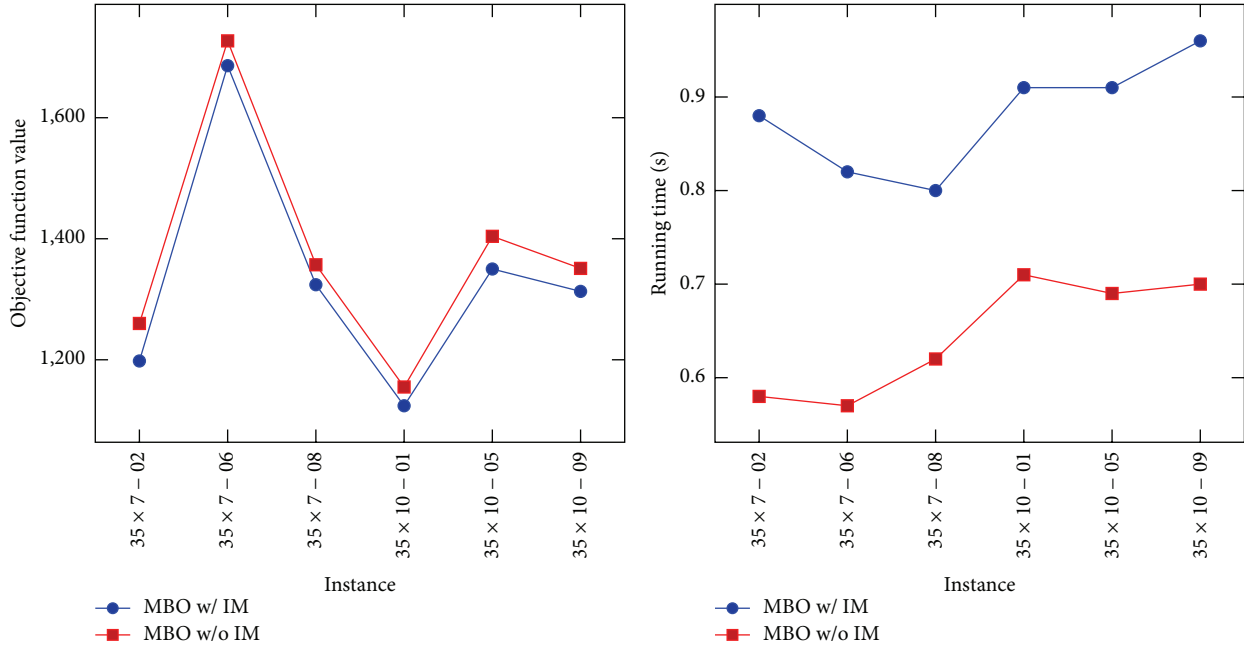


FIGURE 5: Performance of MBO with and without an improvement procedure when solving the DBAP medium-size instances.

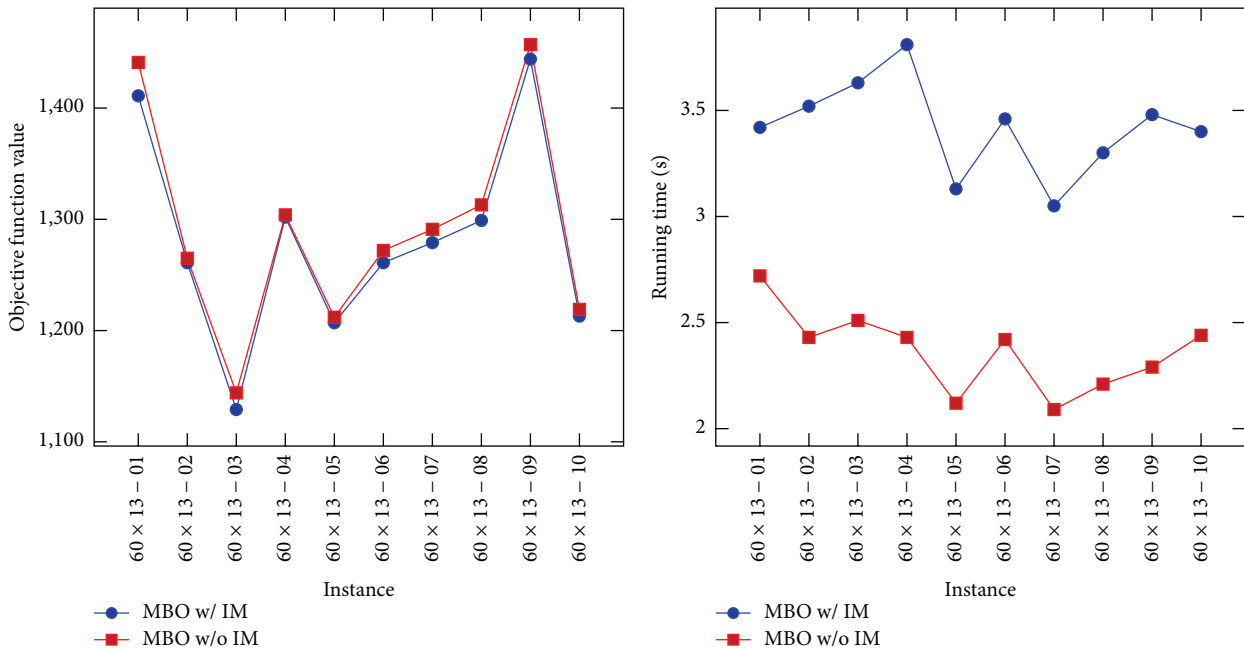


FIGURE 6: Performance of MBO with and without an improvement procedure when solving the DBAP large-size instances.

5.1.2. Comparison with the Best Literature Approach. Tables 1 and 2 present a comparison among the best published approaches for the DBAP, namely, the mathematical model presented by Buhrkal et al. [11], the best approximate approach for this problem consisting of a Particle Swarm Optimization algorithm (PSO) proposed by Ting et al. [13], and our MBO. The first column shows the characteristics of the instances to solve, that is, the number of vessels ($|V|$) and berths ($|B|$), and the instance identifier (id). For each

instance, the best objective value (Obj.), relative error (Gap (%)) with regard to the optimal value provided by CPLEX, and the computational time measured in seconds (t (s)) are presented. Furthermore, with the aim of assessing the time improvement reported by MBO in comparison with PSO, the percentage of time improvement (t_{impr}) is also reported.

As shown in Table 1, MBO reports high-quality solutions in shorter computational times than the other approaches. It reaches the optimal value for the majority of the problem

TABLE 1: Computational results for a representative set of small- and medium-size instances proposed by Cordeau et al. [5].

Instance		CPLEX			PSO			MBO			
$ V $	$ B $	id	Obj.	t (s)	Obj.	Gap (%)	t (s)	Obj.	Gap (%)	t (s)	t_{impr} (%)
25	5	1	759	5.99	759	0.00	0.75	759	0.00	0.29	-61.33
		5	955	6.97	955	0.00	0.86	955	0.00	0.27	-69.77
		10	1073	6.38	1073	0.00	0.73	1073	0.00	0.32	-54.79
25	7	3	807	4.28	807	0.00	0.97	807	0.00	0.24	-75.26
		5	725	3.85	725	0.00	0.44	725	0.00	0.27	-38.64
		8	768	3.93	768	0.00	1.05	768	0.00	0.25	-76.19
25	10	2	727	6.99	727	0.00	0.75	727	0.00	0.36	-52.00
		3	761	6.12	761	0.00	0.56	761	0.00	0.34	-39.29
		5	840	6.77	840	0.00	0.45	840	0.00	0.29	-35.56
35	7	2	1192	15.93	1192	0.00	4.91	1198	0.50	0.81	-83.50
		6	1686	29.16	1686	0.00	3.28	1692	0.36	0.77	-76.52
		8	1318	17.52	1318	0.00	2.39	1324	0.46	0.73	-69.46
35	10	1	1124	19.98	1124	0.00	1.58	1124	0.00	0.91	-42.41
		5	1349	22.31	1349	0.00	1.53	1350	0.07	0.91	-40.52
		9	1311	29.45	1311	0.00	2.81	1313	0.15	0.97	-65.48
Average			1026.33	12.38	1026.33	0.00	1.54	1027.73	0.10	0.52	-58.71

TABLE 2: Computational results for a representative set of large-size instances proposed by Cordeau et al. [5].

Instance		CPLEX			PSO			MBO			
$ V $	$ B $	id	Opt.	t (s)	Obj.	Gap (%)	t (s)	Obj.	Gap (%)	t (s)	t_{impr} (%)
60	13	1	1409	17.92	1409	0.00	11.11	1411	0.14	3.42	-69.22
		2	1261	15.77	1261	0.00	7.89	1261	0.00	3.52	-55.39
		3	1129	13.54	1129	0.00	7.48	1129	0.00	3.63	-51.47
		4	1302	14.48	1302	0.00	6.03	1302	0.00	3.81	-36.82
		5	1207	17.21	1207	0.00	5.84	1207	0.00	3.13	-46.40
		6	1261	13.85	1261	0.00	7.67	1261	0.00	3.46	-54.89
		7	1279	14.60	1279	0.00	7.5	1279	0.00	3.05	-59.33
		8	1299	14.21	1299	0.00	9.94	1299	0.00	3.30	-66.80
		9	1444	16.51	1444	0.00	4.25	1444	0.00	3.48	-18.12
		10	1213	14.16	1213	0.00	5.2	1213	0.00	3.40	-34.62
Average			1280.40	15.23	1280.40	0.00	7.29	1280.60	0.01	3.42	-49.31

instances. Although MBO is not able to provide the optimal solutions in five cases (i.e., $35 \times 7 - 2$, $35 \times 7 - 6$, $35 \times 7 - 8$, $35 \times 10 - 1$, and $35 \times 10 - 9$), it presents a very competitive performance with a time range enough for improvement. In this regard, the maximum gap in those cases is 0.50%. Furthermore, MBO is able to reduce, on average, about the 58% of the time required by PSO.

Moreover, when we evaluate larger problem instances, as those reported in Table 2, we can point out the relevant time improvement reported by MBO over PSO, which is, on average, of almost 50%. In this regard, as shown in this table, the quality of the solutions is similar to the PSO. MBO is able to provide the optimal solutions in the majority of the cases. In the unique case where MBO does not provide the optimal solution, it is able to provide a solution with a gap of 0.07%. It should be also pointed out that the time benefit

presented by MBO makes it suitable as a solution method for being applied either individually or included into integrated schemes in which the berth allocation is required and has to be executed frequently.

5.2. Computational Experiments for the QCSP. In order to assess the suitability of MBO when solving the QCSP, we have considered 40 instances ($k13-k52$) of those proposed by Bierwirth and Meisel [7]. These instances have different number of tasks (from 10 up to 25) and quay cranes (from 2 up to 3) which allow encompassing real-world scenarios. It is worth mentioning that, as done in previous works, in this experiment we have established that the quay cranes are available from the beginning of the service time (i.e., $r^q = 0$, $\forall q \in Q$) and have to keep a safety distance $\delta = 1$ during the service. Moreover, by preliminary tests the following

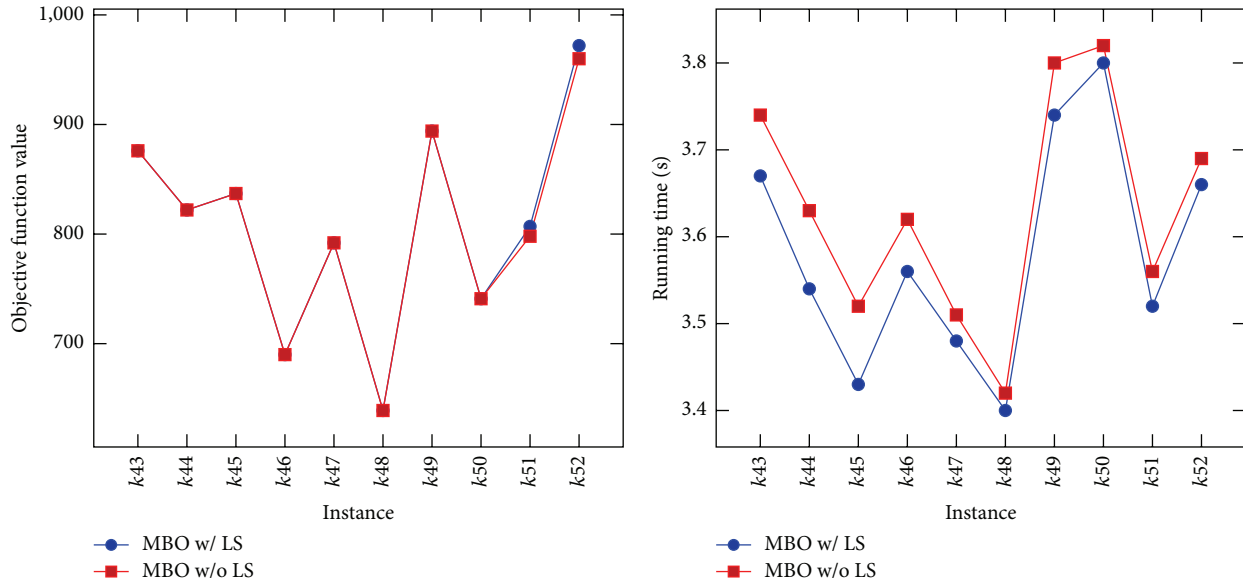


FIGURE 7: Performance of MBO with and without a local search procedure when solving the QCSP $k43$ – $k52$ problem instances.

parameter values have been used in the execution of MBO: $n_{\text{birds}} = 31$, $\delta = 1$, $\lambda = 10$, $\text{iter}_{\text{max}} = 5$, and $K = |N|^3$.

5.2.1. Local Search. As done in previous works (e.g., Sammarra et al. [17], Expósito-Izquierdo et al. [8]), a local search process is applied to the best solution provided by MBO. The rationale behind this is to assess the capacity of MBO to point out promising regions in the search space. Figure 7 shows the computational performance in terms of objective function value and computational time of MBO with (MBO w/LS) and without (MBO w/o LS) local search for the instances $k43$ – $k52$ (for the other instances, $k13$ – $k42$, regardless of the use or not of the local search, our algorithm provides the best known solution). As shown in the figure, the performance exhibited by the MBO with and without LS is similar independently of the instance tackled. In this regard, the use of a local search leads to a very small improvement of some solutions in some cases (see $k51$ and $k52$) requiring only a slightly increase of the computational time. This fact may indicate that, in some cases, the solution provided by MBO is already a local optimum. Finally, although LS contributes to improving the quality of the solution, not using it may not affect substantively the quality of the solution. Nevertheless, due to small computational time required, in the following, the MBO computational results reported for the QCSP instances are the ones obtained with local search.

5.2.2. Comparison with the Best Literature Approach. Table 3 shows a comparison between the optimal solutions reported by Bierwirth and Meisel [7], the Estimation Distribution Algorithm (EDA) proposed by Expósito-Izquierdo et al. [8], and our MBO. In each case, we report the objective function value of the best found solution and the computational time measured in seconds. In the case of the MBO, we also report the gap in the objective function value compared with

the optimal solution and computational time compared with those reported by the EDA.

As can be checked in Table 3, our MBO has reported (near-)optimal solutions for all the instances under analysis. Only in one instance ($k45$), the optimal solution was not reached. In those cases, MBO reports a gap of 0.36% and an overall gap of only 0.01% for all the instances considered. The quality of the solutions reported by MBO indicates that our approach is highly effective in realistic scenarios. Finally, when carrying out an analysis of the computational times, we realize that MBO requires short computational times, requiring at most 3.84 seconds. This fact constitutes a relevant improvement in comparison with the EDA, which requires more than 16 seconds in some instance ($k50$). This time advantage must be suitably considered when addressing practical scenarios where the QCSP has to be solved dynamically.

6. Conclusions and Further Research

In this paper, we have presented a Migrating Birds Optimization-based approach for addressing two essential seaside problems at maritime container terminals: the Dynamic Berth Allocation Problem (DBAP) and Quay Crane Scheduling Problem (QCSP). It is noticeable from the computational experiments that the proposed algorithm is able to report high-quality solutions by means of short computational times. In this regard, the time advantage makes MBO promising and competitive as solution method when tackling seaside operations either individually or embedded into real decision-support systems where this problem has to be solved frequently. Moreover, since our approach includes the use of an improvement method (in the case of DBAP) and a local search (in the case of QCSP) over the best solution provided by MBO, we have assessed the contribution of them to the quality of the solution provided. In this regard, their use

TABLE 3: Comparison among the optimal solutions (UDS, Bierwirth and Meisel [7]), the Estimation Distribution Algorithm (EDA, Expósito-Izquierdo et al. [8]), and our MBO when solving the QCSP.

	UDS		EDA		MBO		Gap (%)
	Obj.	t (s)	Obj.	t (s)	Obj.	t (s)	
k_{13}	453	—	453	0.08	453	0.17	0.00
k_{14}	546	—	546	0.09	546	0.18	0.00
k_{15}	513	—	513	0.08	513	0.17	0.00
k_{16}	312	—	312	0.56	312	0.17	0.00
k_{17}	453	—	453	0.08	453	0.17	0.00
k_{18}	375	—	375	0.07	375	0.16	0.00
k_{19}	543	—	543	0.08	543	0.18	0.00
k_{20}	399	—	399	0.09	399	0.19	0.00
k_{21}	465	—	465	0.07	465	0.17	0.00
k_{22}	540	—	540	0.13	540	0.20	0.00
k_{23}	576	—	576	0.27	576	0.40	0.00
k_{24}	666	—	666	0.39	666	0.38	0.00
k_{25}	738	—	738	0.25	738	0.35	0.00
k_{26}	639	—	639	0.33	639	0.37	0.00
k_{27}	657	—	657	0.29	657	0.35	0.00
k_{28}	531	—	531	0.27	531	0.34	0.00
k_{29}	807	—	807	0.31	807	0.36	0.00
k_{30}	891	—	891	0.22	891	0.40	0.00
k_{31}	570	—	570	0.26	570	0.37	0.00
k_{32}	591	—	591	0.37	591	0.38	0.00
k_{33}	603	—	603	9.12	603	1.13	0.00
k_{34}	717	—	717	9.24	717	1.16	0.00
k_{35}	684	—	684	4.48	684	1.09	0.00
k_{36}	678	—	678	7.62	678	1.13	0.00
k_{37}	510	—	510	4.09	510	1.11	0.00
k_{38}	618	—	618	6.66	618	1.09	0.00
k_{39}	513	—	513	6.54	513	1.14	0.00
k_{40}	564	—	564	7.14	564	1.11	0.00
k_{41}	588	—	588	6.66	588	1.13	0.00
k_{42}	573	—	573	6.30	573	1.18	0.00
k_{43}	876	12.6	876	12.60	876	3.74	0.00
k_{44}	822	12.0	822	11.40	822	3.63	0.00
k_{45}	834	10.8	834	8.40	837	3.52	0.36
k_{46}	690	11.4	690	9.60	690	3.66	0.00
k_{47}	792	10.2	792	10.20	792	3.51	0.00
k_{48}	639	11.4	639	8.40	639	3.44	0.00
k_{49}	894	10.8	894	13.20	894	3.80	0.00
k_{50}	741	10.2	741	16.80	741	3.84	0.00
k_{51}	798	10.2	798	12.00	798	3.52	0.00
k_{52}	960	10.2	960	13.20	960	3.69	0.00
Avg.	633.98	10.98	633.98	4.70	634.05	1.33	0.01

allows an enhancement in the quality of the solutions in terms of objective function value through a small increase of the computational time.

Furthermore, the inherent dynamism of the seaside operations at maritime container terminals highly impacts on

the performance of the technical equipment and, consequently, on the involved transportation modes. Thus, having effective and fast algorithms to reach high-quality solutions is aspired by terminal managers. In this context, at the light of the computational results presented along this paper, we can claim that using MBO is suitable and advisable to be used in practical contexts with the goal of providing an adequate service to the incoming container vessels.

A multitude of lines are open for further research. In the future, we are going to test the performance of MBO in other heterogeneous transportation problems, such as Vehicle Routing Problem, due to its generalist standpoint. In this regard, we are also going to study how different interaction schemes impact on the performance of MBO.

Conflict of Interests

The authors declare that there is no conflict of interests regarding the publication of this paper.

Acknowledgments

This work has been partially funded by the Spanish Ministry of Economy and Competitiveness (Project TIN2012-32608). The authors thank the funding granted to the University of La Laguna (ULL) by the Canary Agency of Investigation, Innovation, and Information Society (ACIISI), 85% cofinanced with the help of European Social Fund. Eduardo Lalla-Ruiz and Christopher Expósito-Izquierdo would like to thank the Canary Government for the financial support they receive through their doctoral grants.

References

- [1] L. Nicoletti, A. Chiurco, C. Arango, and R. Diaz, "Hybrid approach for container terminals performances evaluation and analysis," *International Journal of Simulation and Process Modelling*, vol. 9, no. 1-2, pp. 104–112, 2014.
- [2] C. Expósito-Izquierdo, E. Lalla-Ruiz, B. Melián Batista, and J. M. Moreno-Vega, "Optimization of container terminal problems: an integrated solution approach," in *Computer Aided Systems Theory—EUROCAST 2013*, R. Moreno-Díaz, F. Pichler, and A. Quesada-Arencibia, Eds., vol. 8111 of *Lecture Notes in Computer Science*, pp. 324–331, Springer, Berlin, Germany, 2013.
- [3] H.-J. Yeo, "Competitiveness of Asian container terminals," *The Asian Journal of Shipping and Logistics*, vol. 26, no. 2, pp. 225–246, 2010.
- [4] C. Bierwirth and F. Meisel, "A survey of berth allocation and quay crane scheduling problems in container terminals," *European Journal of Operational Research*, vol. 202, no. 3, pp. 615–627, 2010.
- [5] J.-F. Cordeau, G. Laporte, P. Legato, and L. Moccia, "Models and tabu search heuristics for the berth-allocation problem," *Transportation Science*, vol. 39, no. 4, pp. 526–538, 2005.
- [6] E. Duman, M. Uysal, and A. F. Alkaya, "Migrating birds optimization: a new metaheuristic approach and its performance on quadratic assignment problem," *Information Sciences*, vol. 217, pp. 65–77, 2012.

- [7] C. Bierwirth and F. Meisel, "A fast heuristic for quay crane scheduling with interference constraints," *Journal of Scheduling*, vol. 12, no. 4, pp. 345–360, 2009.
- [8] C. Expósito-Izquierdo, J. L. González-Velarde, B. Melián-Batista, and J. M. Moreno-Vega, "Hybrid estimation of distribution algorithm for the quay crane scheduling problem," *Applied Soft Computing Journal*, vol. 13, no. 10, pp. 4063–4076, 2013.
- [9] A. Imai, E. Nishimura, and S. Papadimitriou, "The dynamic berth allocation problem for a container port," *Transportation Research Part B: Methodological*, vol. 35, no. 4, pp. 401–417, 2001.
- [10] E. Lalla-Ruiz, B. Melián-Batista, and J. Marcos Moreno-Vega, "Artificial intelligence hybrid heuristic based on tabu search for the dynamic berth allocation problem," *Engineering Applications of Artificial Intelligence*, vol. 25, no. 6, pp. 1132–1141, 2012.
- [11] K. Bührkal, S. Zuglian, S. Ropke, J. Larsen, and R. Lusby, "Models for the discrete berth allocation problem: a computational comparison," *Transportation Research Part E: Logistics and Transportation Review*, vol. 47, no. 4, pp. 461–473, 2011.
- [12] R. M. de Oliveira, G. R. Mauri, and L. A. N. Lorena, "Clustering search for the berth allocation problem," *Expert Systems with Applications*, vol. 39, no. 5, pp. 5499–5505, 2012.
- [13] C.-J. Ting, K.-C. Wu, and H. Chou, "Particle swarm optimization algorithm for the berth allocation problem," *Expert Systems with Applications*, vol. 41, no. 4, pp. 1543–1550, 2014.
- [14] E. Lalla-Ruiz and S. Voß, "Popmusic as a matheuristic for the berth allocation problem," *Annals of Mathematics and Artificial Intelligence*, pp. 1–17, 2014.
- [15] F. Meisel and C. Bierwirth, "A unified approach for the evaluation of quay crane scheduling models and algorithms," *Computers & Operations Research*, vol. 38, no. 3, pp. 683–693, 2011.
- [16] K. H. Kim and Y.-M. Park, "A crane scheduling method for port container terminals," *European Journal of Operational Research*, vol. 156, no. 3, pp. 752–768, 2004.
- [17] M. Sammarra, J.-F. Cordeau, G. Laporte, and M. F. Monaco, "A tabu search heuristic for the quay crane scheduling problem," *Journal of Scheduling*, vol. 10, no. 4-5, pp. 327–336, 2007.
- [18] P. Legato, R. Trunfio, and F. Meisel, "Modeling and solving rich quay crane scheduling problems," *Computers & Operations Research*, vol. 39, no. 9, pp. 2063–2078, 2012.
- [19] C. F. Daganzo, "The crane scheduling problem," *Transportation Research Part B: Methodological*, vol. 23, no. 3, pp. 159–175, 1989.

Research Article

An UWB LNA Design with PSO Using Support Vector Microstrip Line Model

Salih Demirel, Filiz Gunes, and A. Kenan Keskin

Electronics & Communication Engineering Department of Yildiz Technical University, Esenler, 34220 Istanbul, Turkey

Correspondence should be addressed to A. Kenan Keskin; kkeskin@yildiz.edu.tr

Received 13 March 2015; Accepted 2 August 2015

Academic Editor: Wei Fang

Copyright © 2015 Salih Demirel et al. This is an open access article distributed under the Creative Commons Attribution License, which permits unrestricted use, distribution, and reproduction in any medium, provided the original work is properly cited.

A rigorous and novel design procedure is constituted for an ultra-wideband (UWB) low noise amplifier (LNA) by exploiting the 3D electromagnetic simulator based support vector regression machine (SVRM) microstrip line model. First of all, in order to design input and output matching circuits (IMC-OMC), source Z_S and load Z_L termination impedance of matching circuit, which are necessary to obtain required input VSWR (V_{ireq}), noise (F_{req}), and gain (G_{Treq}), are determined using performance characterisation of employed transistor, NE3512S02, between 3 and 8 GHz frequencies. After the determination of the termination impedance, to provide this impedance with IMC and OMC, dimensions of microstrip lines are obtained with simple, derivative-free, easily implemented algorithm Particle Swarm Optimization (PSO). In the optimization of matching circuits, highly accurate and fast SVRM model of microstrip line is used instead of analytical formulations. ADCH-80a is used to provide ultra-wideband RF choking in DC bias. During the design process, it is aimed that $V_{ireq} = 1.85$, $F_{req} = F_{min}$, and $G_{Treq} = G_{Tmax}$ all over operating frequency band. Measurements taken from the realized LNA demonstrate the success of this approximation over the band.

1. Introduction

Nowadays, RF circuits have many important usage areas in communication systems. In front-end systems, low noise amplifiers are used in first stage of receiver parts because of their low signal to noise ratio which provides possibility of getting more incoming signal from ambient. Besides, ultra-wideband structures are usually demanded because of their multiple operation frequency choices. To design such ultra-wideband low noise amplifiers, a fast, highly accurate, and feasible method which combines many areas like circuit theory, microwave, and so forth is required [1–4].

Microstrip transmission lines are popularly used to design microwave circuits because of low cost, flexible structure, and easy production. In order to design microstrip matching network of amplifier, a highly accurate, efficient, and fast microstrip transmission line model is required. After obtaining such a model, the lines are synthesized with circuit theory to compose matching circuit. High frequency elements of RF circuit could be analyzed and optimized with numerical programs, but these numerical methods could be slow because of their solution methodology. This

problem would be solved using knowledge based model of RF elements. Learning machine models like artificial neural network (ANN), general regression neural network (GRNN), support vector regression machines (SVRM), and so forth are frequently used in many areas. Microwave applications of learning machines have been issued in previous works such as microwave transistor modeling with ANN [5, 6], SVRM model of a transmission line [7]. Obtained models of different RF elements could be used to synthesise RF circuits.

A low noise microwave amplifier is composed of input and output matching circuit (IMC and OMC), microwave transistor, and DC bias. In order to design IMC and OMC, input and output impedance (Z_S, Z_L) of matching circuits are required for requested transducer gain (G_T), input VSWR (V_i), and noise figure (F_i) of low noise amplifier. This impedance is acquired from performance characterisation of employed microwave transistor [8, 9]. After that, dimensions of microstrip lines in matching circuits are obtained with an optimization algorithm. In the literature, different kinds of optimization algorithms, such as genetic, particle swarm, have been successfully utilized together in microwave circuit and antenna design [10–13].

In this paper, an ultra-wideband low noise microstrip amplifier is designed with novel methodology and then fabricated and measured. Firstly, highly accurate and fast SVRM model of microstrip line is created. Secondly, input and output impedance of matching networks are obtained with performance characterisation of NE3512S02 high technology transistor all over the operation band for requested $G_{T\text{req}}$, $V_{i\text{req}}$, and F_{req} . After that, microstrip line dimensions of IMC and OMC are optimized using evolutionary global optimum searcher PSO [14, 15]. In optimization process, microstrip lines are represented by SWRM model. Finally, designed amplifier is fabricated and measured, and then results are compared with each other.

2. Performance Characterisation for a Microwave Transistor

2.1. Compatible (F, V_i, G_T) Triplets and the (Z_S, Z_L) Terminations. In a typical design problem of a basic microwave amplifier employing per se a FET as an active device, the active device can be represented by a two-port circuit. Since in such a system all the main performance components of F , V_i , and G_T are determined by the active device employed, the device must be identified by all its compatible $(F, V_i, \text{ and } G_T)$ performance triplets and their $(Z_S = Z_{\text{out}}\{\text{IMC}\}, Z_L = Z_{\text{in}}\{\text{IMC}\})$ terminations (Figure 1). Here the (Z_S, Z_L) terminations are the simultaneous solutions of the following nonlinear performance equations of the transistor subject to the physical realization conditions:

$$F = \frac{(S/N)_i}{(S/N)_O} = F\{R_S, X_S\} \\ = F_{\min} + \frac{R_N}{|Z_{\text{opt}}|^2} \frac{|Z_S - Z_{\text{opt}}|^2}{R_S} \quad (1)$$

$$V_i = V_i\{R_S, X_S, R_L, X_L\} = \frac{1 + |\rho_i|}{1 - |\rho_i|}, \quad \rho_i = \frac{Z_S - Z_{\text{in}}^*}{Z_S + Z_{\text{in}}} \quad (2)$$

$$G_T \triangleq \frac{P_L}{P_{\text{AVS}}} = G\{R_S, X_S, R_L, X_L\} \\ = \frac{4R_S R_L |z_{21}|^2}{|(z_{11} + Z_S)(z_{22} + Z_L) - z_{12}z_{21}|^2} \quad (3)$$

Here the physical realization conditions can be expressed as follows:

$$\text{Re}\{Z_{\text{in}}\} = \text{Re}\left\{z_{11} - \frac{z_{12}z_{21}}{z_{22} + Z_L}\right\} > 0. \quad (4)$$

$$\text{Re}\{Z_{\text{out}}\} = \text{Re}\left\{z_{22} - \frac{z_{12}z_{21}}{z_{11} + Z_S}\right\} > 0. \quad (5)$$

$$F \geq F_{\min},$$

$$V_i \geq 1, \quad (6)$$

$$G_{T\min} < G_T \leq G_{T\max},$$

where $z_{ij} = r_{ij} + jx_{ij}$, $i, j = 1, 2$, are the open-circuited parameters of the transistor and the conditions given by (4) and (5) ensure the stable operation of the active device.

The simultaneous solution (Z_S, Z_L) sets of the nonlinear performance equations (1), (2), and (3) subject to the physical realization conditions given by (4), (5), and (6) are obtained in the three main steps which are determinations of (i) the Possible Solution Region (PSR); (ii) the Unconditionally Stable Working Area (USWA); (iii) Variations of the Constrained Gain in the USWA. Finally, the Possible Solution Region (PSR) and the Unconditionally Stable Working Area (USWA) are gathered together with the Variations of the Constrained Gain in the input impedance Z_{in} plane and the resulted configuration may be called "design configuration" which is dependent on the device operation parameters of the frequency f , bias condition IDS, VDS.

2.2. The Possible Solution Region (PSR). Examination of the nonlinear performance equations (1), (2), and (3) reveals, respectively, the following variations for the noise figure F , input VSWR V_i , and gain G_T in the Z_S plane taking Z_L as a control parameter:

(i) All the source $Z_S = R_S + jX_S$ terminations that satisfy $F\{R_S, X_S\} = F_{\text{req}} = \text{const.}$ in (1) take place on the circle in the Z_S plane whose equation is

$$|Z_S - Z_{cn}| = r_n, \quad (7)$$

where Z_{cn} and r_n are the center and radius of the noise circle which can be, respectively, given by [8]

$$Z_{cn} = R_{\text{opt}} + N + jX_{\text{opt}}, \\ r_n = \sqrt{N(N+1) + 2R_{\text{opt}}}, \quad (8)$$

where $Z_{\text{opt}} = R_{\text{opt}} + jX_{\text{opt}}$ is the source termination providing the minimum noise figure to the transistor and the real constant N is described in terms of the noise parameters such that

$$N \triangleq \frac{(F_{\text{req}} - F_{\min})}{2R_n} |Z_{\text{opt}}|^2. \quad (9)$$

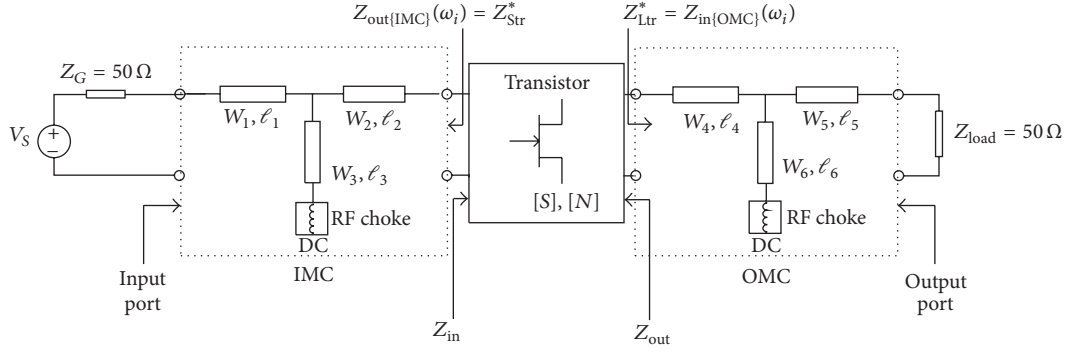
Here when $F_{\text{req}} = F_{\min}$, then $N = 0$, $r_n = 0$, and the noise circle becomes a point of the optimum noise impedance Z_{opt} . While $F_{\text{req}} > F_{\min}$, the centers shift to the right on the $X = X_{\text{opt}}$ line and the radii increase according to (8).

(ii) All the source $Z_S = R_S + jX_S$ terminations that satisfy $V_i = V_i\{R_S, X_S, R_L, X_L\} = V_{i\text{req}} = \text{const.}$ for a fixed passive load Z_L take place on the circle of

$$|Z_S - Z_{cv}| = r_v, \quad (10)$$

where Z_{cv} is the center phasor and r_v is the radius of

$$Z_{cv} = \frac{1 + |\rho_{\text{in}}|^2}{1 - |\rho_{\text{in}}|^2} (R_{\text{in}} - jX_{\text{in}}), \\ r_v = 2 \frac{|\rho_{\text{in}}|}{1 - |\rho_{\text{in}}|^2} R_{\text{in}}. \quad (11)$$


 FIGURE 1: Low noise amplifier with T -type microstrip line matching networks.

A $V_i = V_{i\text{req}}$ circle corresponds to a constant gain circle for a fixed load Z_L , which can be expressed using (2) and (3) as

$$G_T = (1 - |\rho_{in}|^2) \frac{R_L}{R_{in}} \frac{|z_{21}|^2}{|z_{22} + Z_L|^2}. \quad (12)$$

Therefore, only the required noise and the input VSWR circles are sufficient to be taken into account in the Z_S plane. As already seen from (7), (8), and (9), while the required noise circle is fixed in the Z_S plane, the required input VSWR circle can travel, depending on the load impedance Z_L , via the input impedance Z_{in} in a manner given by the center and radius relations in equation given by (11). Thus, the following situations are possible to obtain using the load impedance Z_L as the control parameter: these circles may not touch which corresponds to the no-solution case, they become tangential, or they cut each other [8]. In the following step, each of these positions is mapped into the Z_{in} plane.

(iii) The equations of the T_1 and T_2 boundary circles between the solution and no-solution regions in the Z_{in} plane can be obtained from mapping of the external and internal tangential positions of the VSWR circle with respect to the noise circle, respectively, from the Z_S plane as follows:

$$|Z_{cn} - Z_{cv}|^2 = (r_n \pm r_v)^2. \quad (13)$$

Substituting Z_{cn} , Z_{cv} , r_n , and r_v from (8), (9), and (11) into the (13), the center phasors Z_{ct1} , Z_{ct2} and radii r_{t1} , r_{t2} of the T_1 and T_2 circles can be obtained, respectively, as

$$Z_{ct1} = R_{cn}U + r_nV - jX_{\text{opt}}. \quad (14)$$

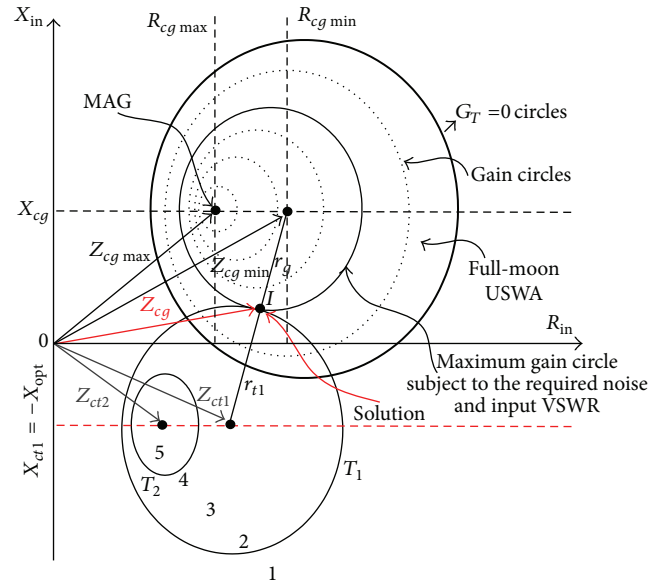
$$r_{t1} = \sqrt{|Z_{ct1}|^2 - |Z_{\text{opt}}|^2}. \quad (15)$$

$$\Leftrightarrow T_1 \text{ circle} \Leftrightarrow \text{Region 2}$$

$$Z_{ct2} = R_{cn}U - r_nV - jX_{\text{opt}}. \quad (16)$$

$$r_{t2} = \sqrt{|Z_{ct2}|^2 - |Z_{\text{opt}}|^2}. \quad (17)$$

$$\Leftrightarrow T_2 \text{ circle} \Leftrightarrow \text{Region 4,}$$


 FIGURE 2: The full-moon USWA for the unconditional stability case is at the right hand side of the Z_{in} plane.

where U and V stand for

$$U \triangleq \frac{1 + |\rho_{in}|^2}{1 - |\rho_{in}|^2}, \quad (18)$$

$$V \triangleq \frac{|\rho_{in}|}{1 - |\rho_{in}|^2}.$$

As seen from (14) and (16), the centers of the T_1 and T_2 circles lie on the same imaginary axis, which is $X = -X_{\text{opt}}$, and it can also be proved using (14)–(17) that circle T_2 is always situated inside circle T_1 without touching as shown in Figure 2.

All the Z_{in} values ensuring intersection positions of both the noise and input VSWR circles in the Z_S plane are situated in Region 3 between the T_1 and T_2 circles in the Z_{in} plane, which is shown in Figures 2 and 3. The remaining regions numbered 1 and 5, which are the outermost and innermost regions, respectively, are impossible solution regions that

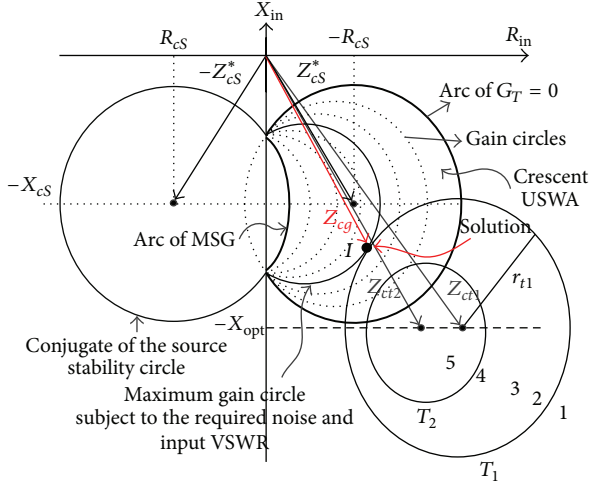


FIGURE 3: The crescent USWA for the conditional stability case takes place at left hand side of the Z_{in} plane.

include Z_{in} values controlling all the nontouching positions in the Z_s plane (Figures 2 and 3).

In order to satisfy the physical realization conditions given by (4), (5), and (6), the Unconditionally Stable Working Area (USWA) and the gain circles constrained by the V_{ireq} must also be constructed in the Z_{in} plane; thus the design configuration will have been formed in the Z_{in} plane.

2.3. Design Configuration and Compatible Performance (F, V_i, G_T) Triplets. There are two types of the design configuration depending on the stability condition of the device:

(i) Design configuration for the absolutely stable device: the necessary and sufficient conditions for this case are as follows:

$$\begin{aligned} r_{11} &> 0, \\ r_{22} &> 0, \\ 2r_{11}r_{22} - r &> |z|, \\ z &\triangleq z_{12}z_{21} \triangleq r + jx. \end{aligned} \quad (19)$$

Examination of the gain equation given in (12) under the constraints of (19) reveals the nonintersection geometry of Figure 2, where the input stability circle is the $G_T = 0$ circle, since it is the geometric place of the mapped load impedance in the purely reactive nature $Z_L = jX_L$. Using (12), one may obtain the centers and radii of the gain circles taking place inside the $G_T = 0$ circle which are, respectively, as follows:

$$R_{cg} = \frac{1}{2r_{22}} (Q - P), \quad (20)$$

$$X_{cg} = \frac{1}{2r_{22}} (2x_{11}r_{22} - x),$$

$$r_g = \frac{1}{r_{22}} \sqrt{P^2 - 2QP + |z|^2}, \quad (21)$$

$$P \triangleq \frac{|z_{12}|^2}{1 - |\rho_i|^2} G_T, \quad (22)$$

$$Q \triangleq 2r_{11}r_{22} - r.$$

It can be seen from (20)–(22) that R_{cg} decreases with the increase of $G_{Treq} \leq G_{Tmax}$ when X_{cg} remains constant (Figure 2) and the G_{Tmax} is only achieved at the point where the r_g equals zero. Setting r_g to zero in (21) gives

$$G_{Tmax} = \left(Q - \sqrt{Q^2 - |z|^2} \right) \frac{1 - |\rho_i|^2}{|z_{12}|^2}. \quad (23)$$

$$Z_{i\max} = Z_{cg\max} = R_{cg\max} + jX_{cg}.$$

$$R_{cg\max} = \frac{1}{r_{22}} (Q^2 - |z|^2).$$

The minimum gain limit circle is the $G_T = 0$ circle input stability circle whose center phasor $Z_{cg\min} = R_{cg\min} + jX_{cg\min}$ and $r_{g\min}$ can be given as follows:

$$\begin{aligned} R_{cg\min} &= \frac{Q}{2r_{22}}, \\ X_{cg\min} &= X_{cg}, \\ r_{g\min} &= \frac{|z|}{2r_{22}}. \end{aligned} \quad (24)$$

Because Q is greater than $|z|$ for the absolutely stable device, $R_{cg\min}$ is greater than $r_{g\min}$, which results in a non-intersection geometry with the $G_T = 0$ circle being entirely in the right half of the Z_{in} plane with the positive real part and enclosing all the circles for $G_T > 0$ (Figure 2). The region inside of the $G_T = 0$ circle is the Unconditionally Stable Working Area (USWA); since the device is unconditionally stable, all the compatible (F, V_i, G_T) triplets take place in the intersection area between the PSR and USWA and any selection criteria to establish the design target space can be applied to them.

(ii) Design configuration for the conditionally stable device: in the case of the conditionally stable transistor, the USWA takes place between the input stability circle which is the $G_T = 0$ circle and the arc of the conjugate of the stability circle remaining in the right half of the Z_{in} plane (Figure 3). The constrained gain formula equation (12) can be rearranged in terms of the radius and center of the source plane stability circle as

$$|Z_i|^2 + 2(R_{CS} + S)R_i + 2X_{CS}X_i + |Z_{CS}|^2 - r_s^2 = 0, \quad (25)$$

$$S \triangleq \frac{|z_{12}|^2 G_T}{2r_{22} (1 - |\rho_i|^2)}, \quad (26)$$

$$\begin{aligned}
R_{CS} &= -\frac{2r_{11}r_{22} - r}{2r_{22}}, \\
X_{CS} &= \frac{2x_{11}r_{22} - r}{2r_{22}}, \\
r_s &= \frac{|z|}{2r_{22}}.
\end{aligned} \tag{27}$$

The features of the G_T circles, which can be derived from (25)–(27), can briefly be expressed as follows (Figure 3):

(a) All G_T circles cut the imaginary axis at the same points, which are the intersection points of the conjugate of the source plane stability circle with the same axis.

(b) The $G_T = 0$ circle whose center is $Z_{cgmin} = -R_{cs} - jX_{cs}$ with $r_{gmin} = r_s$ is symmetrical with the conjugate of the stability circle with respect to the imaginary axis.

(c) The $G_{Tmax} > G_T > 0$ circles always take place in the USWA. As the absolute stability case, all the compatible (F, V_i, G_T) triplets take place in the intersection area between the PSR and USWA.

(d) In the conditional stability case, the maximum gain will be obtained on the arc of the conjugate stability circle remaining in the right half of the Z_{in} plane. The maximum gain subject to the V_i can be found by substituting $R_{cg} = R_{cs}$ in (27):

$$G_{Tmax} = 2 \frac{1 - |\rho_i|^2}{|z_{12}|^2}. \tag{28}$$

We have the Maximum Stable Gain (MSG)

$$MSG = 2 \left| \frac{z_{21}}{z_{12}} \right| \eta, \quad \eta \triangleq \frac{2r_{11}r_{22} - r}{|z|}, \tag{29}$$

where η is the stability factor with the values between zero and unity ($0 > \eta > 1$).

3. SVRM Model of Microstrip Line

In this section, SVRM model of a microstrip line is presented. It is significant that SVRM model of microstrip line is as fast as analytical formulation and is highly accurate like 3D numerical simulations. The mathematical background and detailed theory of SVRM are explained in previous work [7]. In this study, epsilon SVR [16] is employed as SVM type and radial basis function is performed as kernel type. Input variables of model are line width (W), frequency (f), height (h), and relative permittivity (ϵ_r) of substrate material and corresponding output variables are characteristic impedance (Z_0) and effective relative permittivity (ϵ_{eff}). Because each machine has one output, there are two machines with the same inputs.

First of all, coarse model of microstrip line, which has a training data set acquired from quasi-TEM analytical formulations, is formed. Input and output variable values of training data set are given in Table 1. Furthermore, support vectors (SVs) and accuracy of coarse model are shown for different epsilon values in Table 2. The obtained support vectors are used to form training data set of fine model, such that these

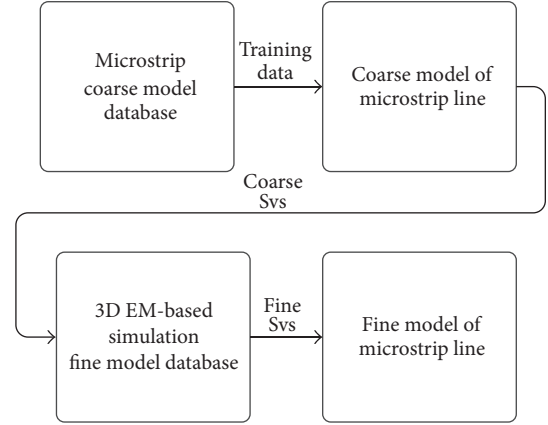


FIGURE 4: Cost effective 3D EM simulation-based Support Vector Microstrip Modeling.

TABLE 1: The range of values for SVRM training data set for coarse model.

Parameters	Start value	Stop value	Interval
Width (W)	0.1 mm	4.6 mm	0.5 mm
Height (h)	0.1 mm	2.2 mm	0.7 mm
Permittivity (ϵ_r)	2	10	2
Frequency (f)	2 GHz	14 GHz	3 GHz
Characteristic impedance (Z_0)	3 ohms	240 ohms	
Effective permittivity (ϵ_{eff})	1.5	9.7	

TABLE 2: SVRM parameters for coarse model.

γ	C	Epsilon (ϵ)	Number of " Z_0 " SVs	Accuracy
0.001	10000	0.05	583	%99.4
0.001	10000	0.07	402	%98.6
0.001	10000	1	279	%97.9

SVs are chosen as input variables of training data and output data is calculated with 3D electromagnetic simulator, as seen in Figure 4. Therefore, either training data number is reduced or duration of data set forming is shortened. The same SVR model and kernel type are used for fine model training. According to results of fine model, accuracy of characteristic impedance and effective permittivity are %99.4 and %99, respectively, and it is also 400 times faster than 3D EM simulator for 2.3 GHz CPU and 2 GB memory. As an example, Figure 5 shows characteristic impedance and effective relative permittivity variations subject to width of line for fine model ($\epsilon_r = 2.94$, $h = 0.762$ mm). Consequently, expeditious and highly accurate model of microstrip line is ready to perform in optimization network.

4. Optimization

During the design optimization process, determining widths and lengths of microstrip lines in input and output matching network is objected, so that IMC and OMC provide source and load impedance which are obtained from performance

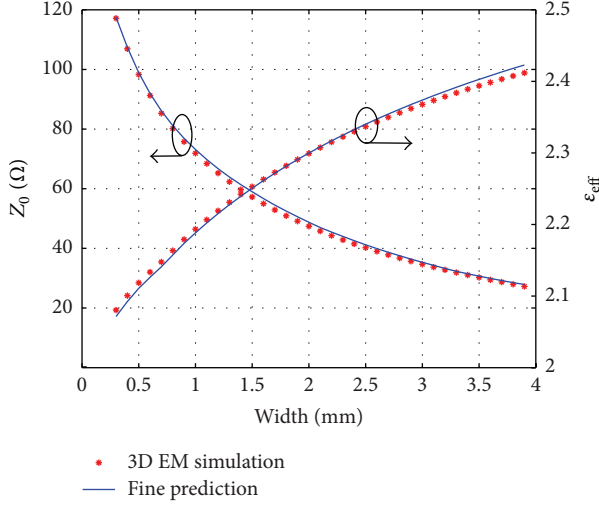


FIGURE 5: Comparative variations of characteristic impedance and effective dielectric constant versus width of the fine model and the 3D EM simulation on the substrate $\epsilon_r = 2.94$, $h = 0.762$ mm at $f = 6$ GHz.

characterisation of employed transistor (NE3512S02) for minimum noise $F_{\text{req}}(\omega) = F_{\text{min}}$, maximum gain $G_{T\text{req}}(\omega) = G_{T\text{max}}$, and $V_{i\text{req}}(\omega) = 1.85$ input VSWR. For this purpose, gains of the input/output matching circuits (G_T) terminated by the $Z_{\text{Str}}^*(\omega)$ and the $Z_{\text{Ltr}}^*(\omega)$ are maximized all over the requested operation band (B_{req}), as seen in Figure 1. In order to do that, the cost function is chosen as minimization of

$$\text{cost}(\vec{W}, \vec{\ell}) = \sum_{i=1}^N 1 - G_T(\vec{W}, \vec{\ell}, \omega_i), \quad (30)$$

where

$$G_T = \frac{4R_S R_L}{|AZ_L + B + Z_S(CZ_L + D)|^2}, \quad (31)$$

$$W_\ell \leq W_i \leq W_u, \quad \ell_\ell \leq \ell_i \leq \ell_u; \quad i = 1, \dots, \Lambda,$$

where A , B , C , D , Z_S , and Z_L parameters of matching circuit configurations are calculated using the cost effective SVRM model of the microstrip line given in Section 3 for chosen substrate (ϵ_r, h). Also, N is the number of the sampled frequencies within the bandwidth and is the element number of the matching circuit.

PSO algorithm is performed to minimize the cost function given by (30) with respect to the microstrip widths and lengths. PSO is a population based optimization method for an N -dimensional problem; the position and velocity of each particle can be specified by $M \times N$ matrices, where M is the number of particles in the swarm.

Firstly, physical parameters, which are geometric limits of matching circuits, and convergence parameters, which are tolerance parameter (τ) and maximum iteration number (κ_{max}), of the algorithm are assigned. In the updating process, position, velocity, personal best, and global best matrices are launched randomly. For each iteration, cost function value

is calculated for each particle and these values are used to determine each particle's personal best and global best value of the swarm. The algorithm ends when either the error or the iteration number reaches its assigned value. Comprehensive design optimization algorithm of the amplifier is depicted in Figure 6.

5. Design Example and Measurement

As a test vehicle of the presented methodology, the worked design example of typical wideband, low noise amplifiers using the T -types of microstrip matching circuits will be given. In design example, transistor NE3512S02 is used and Figure 7 gives the maximum gain variations constrained by the minimum noise figure, resulted from its performance characterisation at $V_{\text{DS}} = 2$ V and $I_{\text{DS}} = 20$ mA. From Figure 7, it is understood that there is no solution all over the operation band for every V_i value and $V_i = 1.85$ is the most appropriate solution for both flat gain and mismatching as little as possible. In the design optimization process, the performance ($F_{\text{req}}(\omega) = F_{\text{min}}(\omega)$, $V_{i\text{req}}(\omega) = 1.85$, and $G_{T\text{req}}(\omega) = G_{T\text{max}}(\omega)$) triplet within the bandwidth of 3 GHz $\leq f \leq 8$ GHz at the bias condition of $V_{\text{DS}} = 2$ V and $I_{\text{DS}} = 20$ mA is required as a design target and the real and reactive parts of the corresponding source and load terminations obtained by performance characterisation are trying to satisfy with matching circuits. As substrate material, RO 6002 is used $\{\epsilon_r = 2.94, h = 0.762$ mm, $\tan \delta = 0.002, t = 0.035$ mm}. In order to provide ultra-wideband DC bias of the transistor, ADCH-80A+ RF choke [17] is used in T -type of microstrip MCs, as seen in Figure 1. Moreover, in our PSO application, convergence happens between 150 and 300 iterations depending on the initialization values taking 2 minutes 37 seconds and 4 minutes 33 seconds, respectively, using 50 particles with 2.3 GHz CPU Processor, 2 GB RAM. After so many trials, best particles number is chosen as 50 for this application. Besides, PSO convergence parameters and maximum iteration number are taken as 0.005 and 300, respectively. Figure 8 shows convergence curve of cost function, where the convergence typically occurs within 200 numbers of iterations. After optimization process the designed amplifier is fabricated and measured. Picture of the manufactured ultra-wideband LNA is given in Figure 9 and the optimum values for the T -types of microstrip widths and lengths $\{\vec{W}, \vec{\ell}\}$ are found in Table 3. Furthermore the performances of the synthesized amplifier are compared using a microwave system circuit simulator and verified to agree with each other. Thus the targeted, synthesized, simulated, and measured performance ingredients gain, V_i , V_{out} , and noise with respect to the frequency are given for the amplifiers with the T -types of microstrip matching circuits in Figures 10, 11, 12, and 13, respectively.

6. Conclusions

In this work, the highly nonlinear design optimization problem of the linear regime microwave amplifiers is solved by a systematic and efficient methodology in which each

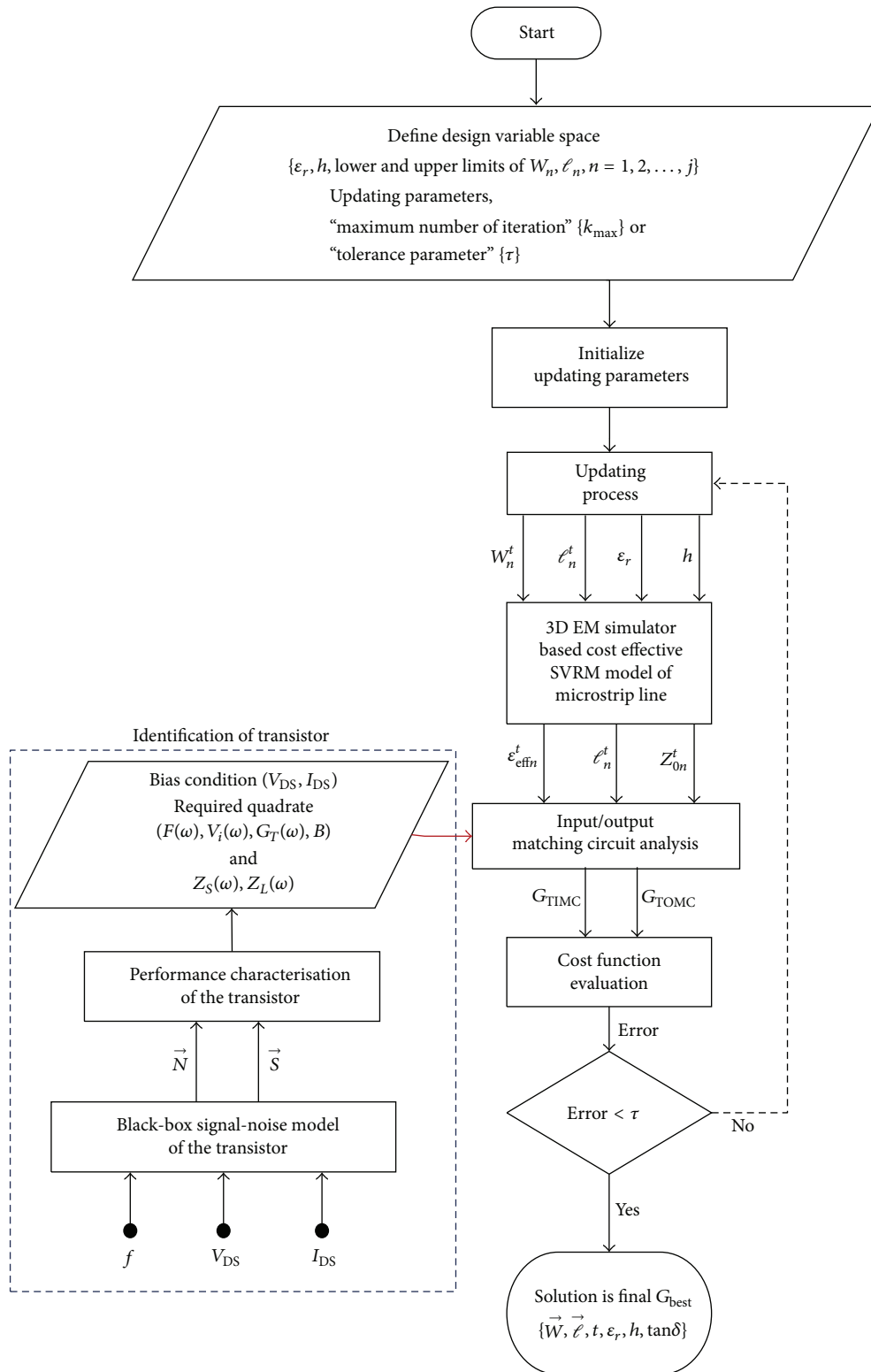


FIGURE 6: Block diagram of the performance characterisation-based design optimization of the matching circuits with the cost effective 3D EM-based Support Vector Microstrip Model.

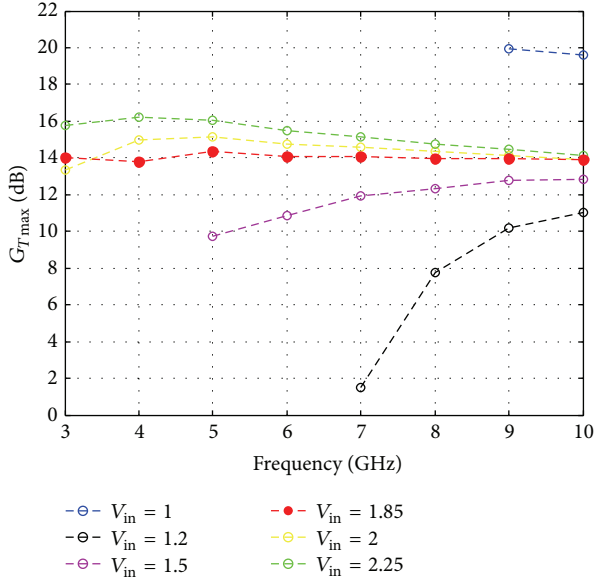


FIGURE 7: Maximum transducer gain for different input VSWR ($V_{DS} = 2\text{ V}$, $I_{DS} = 20\text{ mA}$, and $F_{req} = F_{min}\text{ dB}$).

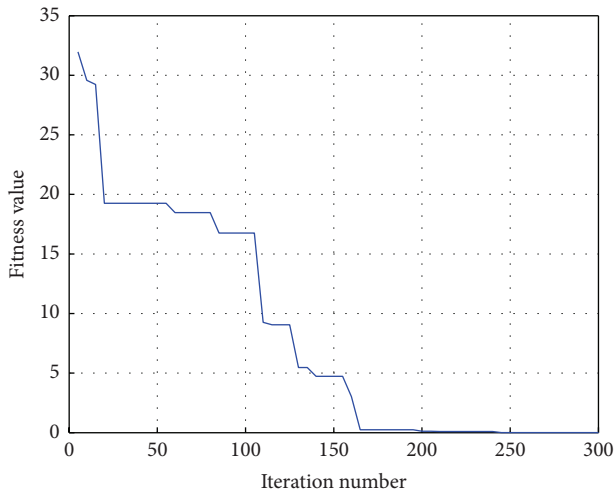


FIGURE 8: Cost function convergence curve.

TABLE 3: Solution space for the (T-T) IMC and OMC elements.

W_1 (mm)	W_2 (mm)	W_3 (mm)	W_4 (mm)	W_5 (mm)	W_6 (mm)
2,4	0,25	0,25	0,75	0,25	3
ℓ_1 (mm)	ℓ_2 (mm)	ℓ_3 (mm)	ℓ_4 (mm)	ℓ_5 (mm)	ℓ_6 (mm)
4,25	14,5	2,5	13	6,5	15,75

constituent of the optimization procedure is defined on the rigorous mathematical bases. First of all, identification of transistor is based upon the potential performance of the employed transistor in the form of interrelations among the operation parameters (f , V_{DS} , I_{DS}) and performance measure functions, gain, input VSWR, and noise, built by using the linear circuit and noise theories. Thus, this will enable the designer to choose the most proper compatible {noise

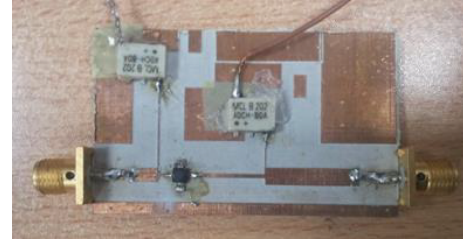


FIGURE 9: Fabricated UWB low noise amplifier.

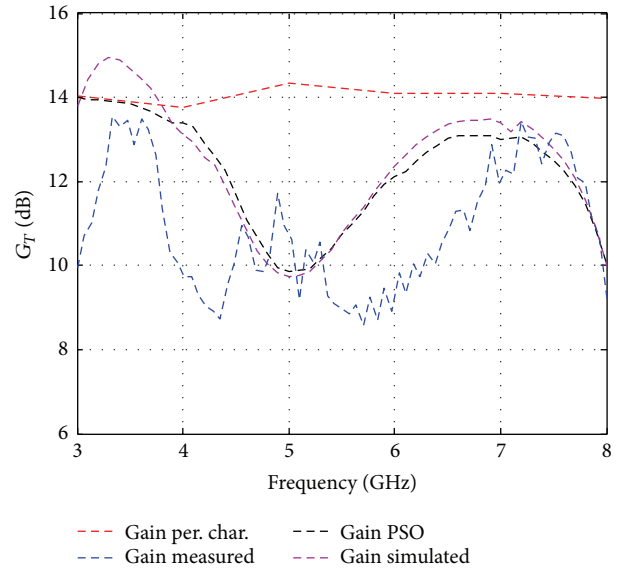


FIGURE 10: Comparative results for transducer gain of designed amplifier.

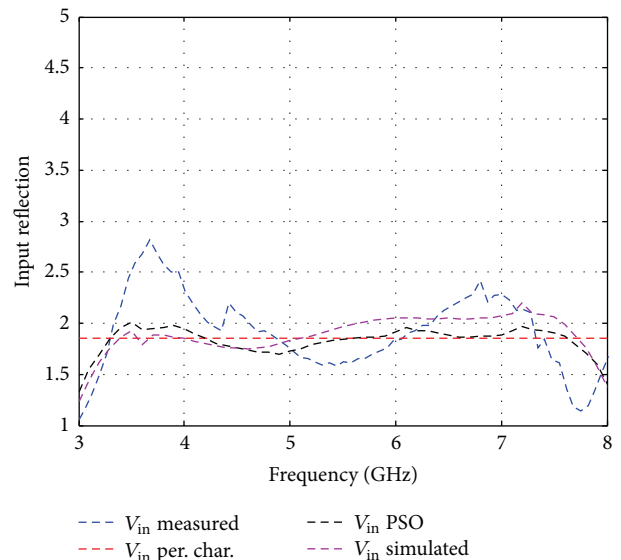


FIGURE 11: Comparative results for input VSWR of designed amplifier.

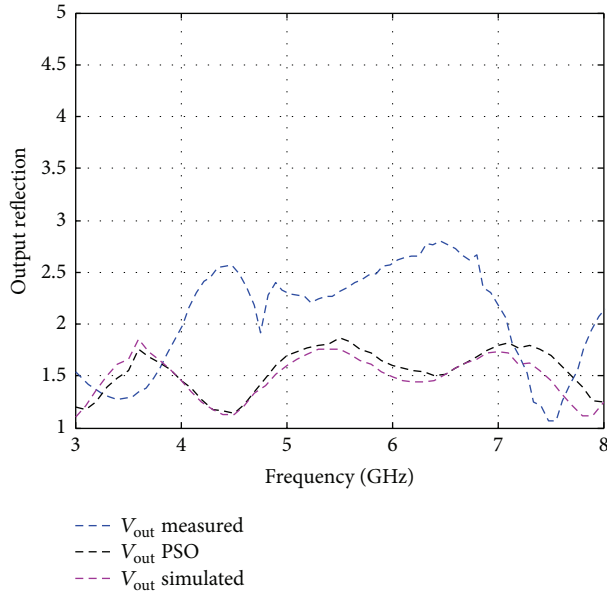


FIGURE 12: Comparative results for output VSWR of designed amplifier.

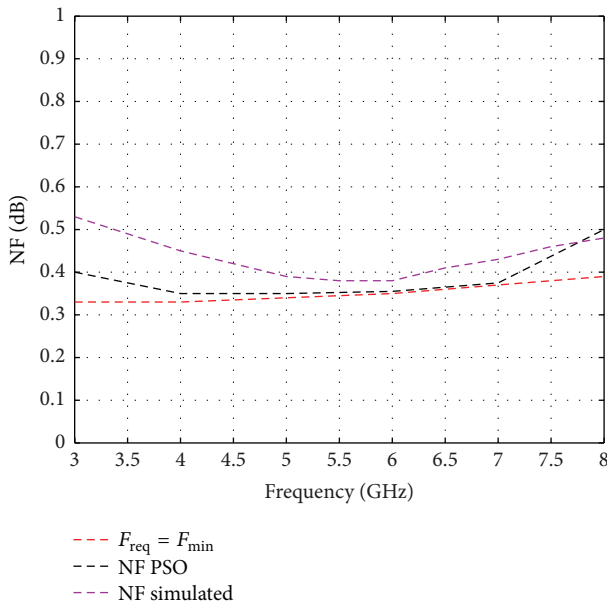


FIGURE 13: Comparative results for noise figure of designed amplifier.

$F(\omega) \geq F_{\min}(\omega)$, input VSWR $V_{in}(\omega) \geq 1$, gain $G_{T_{\min}}(\omega) > G_T(\omega) \geq G_{T_{\max}}(\omega)$, bandwidth B quadruple as being aware of its advantages and disadvantages. The necessary source $Z_S(\omega)$ and load $Z_L(\omega)$ terminations will also be provided so that the multiobjective optimization is reduced into the two separate single objective scalar optimization processes within a design variable space subject to the technological limits. Another significant contribution of this work is to provide a fast, accurate, and cost effective model employing novel soft technology facilities in which the characteristic

impedance Z_0 and the dielectric constant ϵ_{eff} of the equivalent transmission line are expressed as the continuous functions to be used in the updating process. In this work, the 3D EM-based SVRM analysis model of the microstrip line has been provided to be used in the updating process. In the modelling process, the substantial reduction (by up to %60) is obtained utilizing sparseness of the standard SVRM in the number of expensive fine discretization training data with the negligible loss in the predictive accuracy in conjunction with the quasi-TEM microstrip synthesis formulae as the coarse data generator that allow identifying the regions of the design space requiring denser sampling. Besides, any convenient algorithm using either gradient or no gradient can be employed for the updating processes; in our case PSO is used for the accuracy and fast convergence.

Finally as the worked example, this design methodology is applied to the design of typical wideband low noise amplifiers of the transistor NE3512S02 on the dielectric substrate $\{\epsilon_r = 2.94, h = 0.762 \text{ mm}, \tan \delta = 0.002, \text{ and } t = 0.035 \text{ mm}\}$ within 3 GHz and 8 GHz satisfying $\{F_{\min}(f), V_{in} = 1.85, G_{T_{\max}}(f)\}$ triplet using T -type of microstrip matching circuits. After that, the designed amplifier is manufactured and measured. Both simulated and measured results validate the predicted design with good agreement. It is concluded that this method, which is highly accurate as 3D EM simulator and fast as analytical solution, can also be applied as a robust method for the design and analysis of any microstrip amplifier synthesis.

Conflict of Interests

The authors declare that there is no conflict of interests regarding the publication of this paper.

References

- [1] H. Fukui, "Available power gain, noise figure, and noise measure of two-ports and their graphical representations," *IEEE Transactions on Circuit Theory*, vol. 13, no. 2, pp. 137–142, 1966.
- [2] H. Fukui, "Design of microwave GaAs MESFET's for broadband low-noise amplifiers," *IEEE Trans Microwave Theory Tech*, vol. 27, no. 7, pp. 643–650, 1979.
- [3] A. Dobrowolski, *Introduction to Computer Methods for Microwave Circuit Analysis and Design*, Artech House, Norwood, Mass, USA, 1991.
- [4] G. Gonzales, *Microwave Transistor Amplifiers*, Prentice-Hall, London, UK, 1996.
- [5] Z. Marinković, O. Pronić-Rančić, and V. Marković, "Small-signal and noise modeling of class of HEMTs using knowledge-based artificial neural networks," *International Journal of RF and Microwave Computer-Aided Engineering*, vol. 23, no. 1, pp. 34–39, 2013.
- [6] Q.-J. Zhang, K. C. Gupta, and V. K. Devabhaktuni, "Artificial neural networks for RF and microwave design—from theory to practice," *IEEE Transactions on Microwave Theory and Techniques*, vol. 51, no. 4, pp. 1339–1350, 2003.
- [7] F. Güneş, N. T. Tokan, and F. Gürgen, "A knowledge-based support vector synthesis of the transmission lines for use in microwave integrated circuits," *Expert Systems with Applications*, vol. 37, no. 4, pp. 3302–3309, 2010.

- [8] F. Güneş, M. Güneş, and M. Fidan, "Performance characterisation of a microwave transistor," *IEE Proceedings: Circuits, Devices and Systems*, vol. 141, no. 5, pp. 337–344, 1994.
- [9] F. Güneş and B. A. Çetiner, "A novel Smith chart formulation of performance characterization for a microwave transistor," *IEE Proceedings—Circuits, Devices and Systems*, vol. 145, pp. 419–428, 1998.
- [10] N. Telzhensky and Y. Leviatan, "Novel method of UWB antenna optimization for specified input signal forms by means of genetic algorithm," *IEEE Transactions on Antennas and Propagation*, vol. 54, no. 8, pp. 2216–2225, 2006.
- [11] S. Chamaani, M. S. Abrishamian, and S. A. Mirtaheri, "Time-domain design of UWB vivaldi antenna array using multiobjective particle swarm optimization," *IEEE Antennas and Wireless Propagation Letters*, vol. 9, pp. 666–669, 2010.
- [12] D. Swanson and G. Macchiarella, "Microwave filter design by synthesis and optimization," *IEEE Microwave Magazine*, vol. 8, no. 2, pp. 55–69, 2007.
- [13] R. Menozzi, A. Piazzzi, and F. Contini, "Small signal modeling for microwave FET linear circuits based on a genetic algorithm," *IEEE Transactions on Circuits and Systems I: Fundamental Theory and Applications*, vol. 43, no. 10, pp. 839–847, 1996.
- [14] R. Eberhart and J. Kenedy, "A new optimizer using particle swarm theory," in *Proceedings of the 6th International Symposium on Micro Machine and Human Science (MHS '95)*, pp. 39–43, Cape Cod, Mass, USA, 1995.
- [15] R. Eberhart and J. Kennedy, "Particle swarm optimization," in *Proceedings of the IEEE International Conference on Neural Networks*, pp. 1114–1121, Piscataway, NJ, USA, December 1995.
- [16] V. N. Vapnik, *The Nature of Statistical Learning Theory*, Springer, New York, NY, USA, 1995.
- [17] 2015, <http://194.75.38.69/pdfs/ADCH-80A.pdf>.